Palaeogeography, Palaeoclimatology, Palaeoecology 573 (2021) 110432

Contents lists available at ScienceDirect

Palaeogeography, Palaeoclimatology, Palaeoecology

journal homepage: www.elsevier.com/locate/palaeo

Climate and biotic evolution during the Permian-Triassic transition in the temperate Northern Hemisphere, Kuznetsk Basin, Siberia, Russia

V.I. Davydov [a,b,*], E.V. Karasev [a,c], N.G. Nurgalieva [a], M.D. Schmitz [b], I.V. Budnikov [d], A. S. Biakov [a,e], D.M. Kuzina [a], V.V. Silantiev [a], M.N. Urazaeva [a], V.V. Zharinova [a], S.O. Zorina [a], B. Gareev [a], D.V. Vasilenko [c]

[a] Kazan Federal University, Kazan, Russia
[b] Boise State University, Boise, ID, USA
[c] Paleontological Institute RAS, Moscow, Russia
[d] Siberian Research Institute of Geology, Geophysics and Mineral Resources, Novosibirsk, Russia
[e] North-East Interdisciplinary Scientific Research Institute RAS, Magadan, Russia

ARTICLE INFO

Editor: Thomas Algeo

Keywords:
Terrestrial sediments
Permian-Triassic extinction
Multidisciplinary study
CA-IDTIMS
Geochemistry
Quantitative correlation
Biodiversity
Paleoenvironments

ABSTRACT

The Siberian Traps volcanism is widely considered the main cause of the end-Permian mass extinction, the greatest biological crisis in the Earth history. While the extinction is interpreted as catastrophic and sudden with estimates of duration of approximately 35–40 thousand years from marine strata in South China, various lines of evidence have emerged for a more complex, prolonged, and diachronous extinction pattern. We present here the results of a multidisciplinary study of the Permian-Triassic continental transition in the Kuznetsk Basin, Russia. The region is proximal to the Siberian Traps LIP and the detrimental effects of the flood basalt volcanism in the Kuznetsk Basin may have been of similar scale as in the main area of the Siberian Traps distribution (Tunguska and Taymyr regions). Whereas earlier work has placed the Permian-Triassic boundary position between the coal-bearing Tailugan Formation and the volcanoclastic Maltsev Formation, here we revised the traditional model using three independent methods: radioisotopic CA-IDTIMS U-Pb zircon ages, $\delta^{13}C_{org}$ isotope values and paleomagnetic proxies. The regional extinction of the humid-dominated forest flora (cordaites) and the aridity-induced biotic turnover in the Kuznetsk Basin occurred 820 kyr earlier than the end-Permian extinction event recorded in South China at 251.94 Ma. The biota in Kuznetsk Basin at the turnover subsequently diversified (with some exceptions) across the Permian-Triassic transition.

By compiling a large taxonomic database, we find that marine and terrestrial biotic diversity in Siberia progressively increased from the beginning of the Permian up to the middle Roadian (early Guadalupian global glacial event). After that time, the diversity at the species and generic level progressively and slowly declined towards the aforementioned latest Changhsingian (252.76 Ma) biotic turnover. Starting from this time, the biota rapidly diversified in the latest Changhsingian and Early-Middle Triassic. We suggest that the Permian-Triassic mass extinction mostly occurred in the tropics and subtropics due to the strong climatic warming, which was relatively low in late Changhsingian and gradually but quickly extends in the latest Changhsingian to an abnormally high temperature and extremely low oxygenated water in the oceans that was deadly for most marine animals. The warm climate shift poleward during Permian-Triassic transition in the middle-high latitudes caused the replacement (turnover) of the humid-related biotas by the dry climate-related and more diverse communities, which continued to expand throughout the Triassic in both marine and terrestrial habitats. The pattern of the Permian-Triassic event in both marine and terrestrial habitats was more intricate in terms of extinction, turnover, and diversity of biota within the different climatic zones and environmental habitats than has been generally considered.

* Corresponding author at: Kazan Federal University, Kazan, Russia.
E-mail addresses: vdavydov@boisestate.edu (V.I. Davydov), karasev@paleo.ru (E.V. Karasev), nurgal07@gmail.com (N.G. Nurgalieva), markschmitz@boisestate.edu (M.D. Schmitz), budnikov@sniiggims.ru (I.V. Budnikov), abiakov@mail.ru (A.S. Biakov), di.kuzina@gmail.com (D.M. Kuzina), VSilant@gmail.com (V.V. Silantiev), Milyausha.Urazaeva@kpfu.ru (M.N. Urazaeva), veronika.zharinova.kpfu@gmail.com (V.V. Zharinova), svzorina@yandex.ru (S.O. Zorina), bulat@gareev.net (B. Gareev), d.v.vassilenko@gmail.com (D.V. Vasilenko).

https://doi.org/10.1016/j.palaeo.2021.110432
Received 19 November 2020; Received in revised form 19 April 2021; Accepted 20 April 2021
Available online 24 April 2021

1. Introduction

The Permian-Triassic mass extinction attracts both scientific and popular attention with its unprecedented scale and evolutionary consequences. The fact that extinction coincided in time with abrupt climate warming (Joachimski et al., 2012), leads some to find analogues of this event in modern climate changes (Payne and Clapham, 2012; Bond and Grasby, 2017; Clapham and Renne, 2019), with the expectation of similar consequences for extant life (biota) as were recorded across the Permian-Triassic transition (Wiens, 2016; Hurd et al., 2018; Neukom et al., 2019; Abatzoglou et al., 2020). Moreover, most experts believe that the extinction was catastrophic and sudden with estimates of duration of approximately 35–40 thousand years from marine strata in South China (Bond and Wignall, 2014; Burgess et al., 2014; Shen et al., 2019). According to this model, the extinction led to the geologically "instantaneous" disappearance of more than 95% of marine and 85% of terrestrial taxa (Hallam and Wignall, 1997; Sepkoski, 2002; Stanley, 2016). On the other hand, various evidence has emerged for a more complex, prolonged, and diachronous extinction pattern (Kerp, 1996; Algeo et al., 2012; Crasquin and Forel, 2014; Schneebeli-Hermann et al., 2015; Kiessling et al., 2018; Song et al., 2018; Fielding et al., 2019), particularly when contrasting marine and terrestrial records.

The Siberian Traps volcanism, including the interaction of intruding sills into volatile-rich basin fill rocks (coal, evaporite and sulfates), is now considered the main cause of this greatest global extinction in the Earth history (Alroy et al., 2008; Reichow et al., 2009; Svensen et al., 2009; Bond and Wignall, 2014; Bond and Grasby, 2017; Ernst and Youbi, 2017; Svensen et al., 2018; Clapham and Renne, 2019). The timing and tempo of Siberian volcanism has been increasingly well constrained with both $^{40}Ar/^{39}Ar$ and U-Pb geochronology (Reichow et al., 2009; Burgess and Bowring, 2015; Burgess et al., 2017). The model developed in these publications proposes that a gigantic ejection of volatile sublimates of the volcanic and intrusive magmatic activity, and in particular their interaction with the organic-rich host rocks, created the kill mechanism (s) of mass extinction on the continents and in the oceans (Burgess et al., 2017; Jerram et al., 2016; Svensen et al., 2018).

The extinction pattern is documented in detail in many marine sections in South China and Iran, where the record of different proxies is exceptionally well defined and calibrated either with high-resolution biostratigraphy (conodonts, ammonoids) or with high-precision CA-IDTIMS analyses, or a combination of both (Jin et al., 2006; Joachimski et al., 2012; Jun et al., 2005; Korte and Kozur, 2005; Korte and Kozur, 2010; Korte et al., 2010; Kozur, 2005; Kozur, 2007; Kozur and Wardlaw, 2010; Mei et al., 1998; Shen et al., 2011; Yin et al., 2014; Yin et al., 2012; Yuan et al., 2019). Marine anoxia, hypercapnia, and ocean acidification are suggested as being the killing factors in the oceans, and have generally been linked to sudden and massive increase of CO_2, methane and sulfates from the Siberian Traps region (Kump et al., 2005; Knoll et al., 2007; Payne and Kump, 2007; Meyer et al., 2008; Algeo et al., 2011; Brennecka et al., 2011; Clapham and Payne, 2011; Bond and Wignall, 2014; Bond and Grasby, 2017). The suggested high content of CO_2 and particularly sulfides in the atmosphere potentially induced widespread acidic rains, that destroyed the forest and soils on the continents and cause the extinction of tetrapods and plants (Retallack and Krull, 1999; Krull and Retallack, 2000; Meyer et al., 2008; Sobolev et al., 2011; Kershaw et al., 2012; Retallack, 2013; Benton and Newell, 2014; Sobolev et al., 2015). It is supposed that the hazards within and around the area of volcanic eruption greatly influenced the regional terrestrial climate, environments, and biota (Kusky, 2008; Latter, 2013; Peate and Elkins-Tanton, 2015). Obviously, the biota of the Siberian Platform and

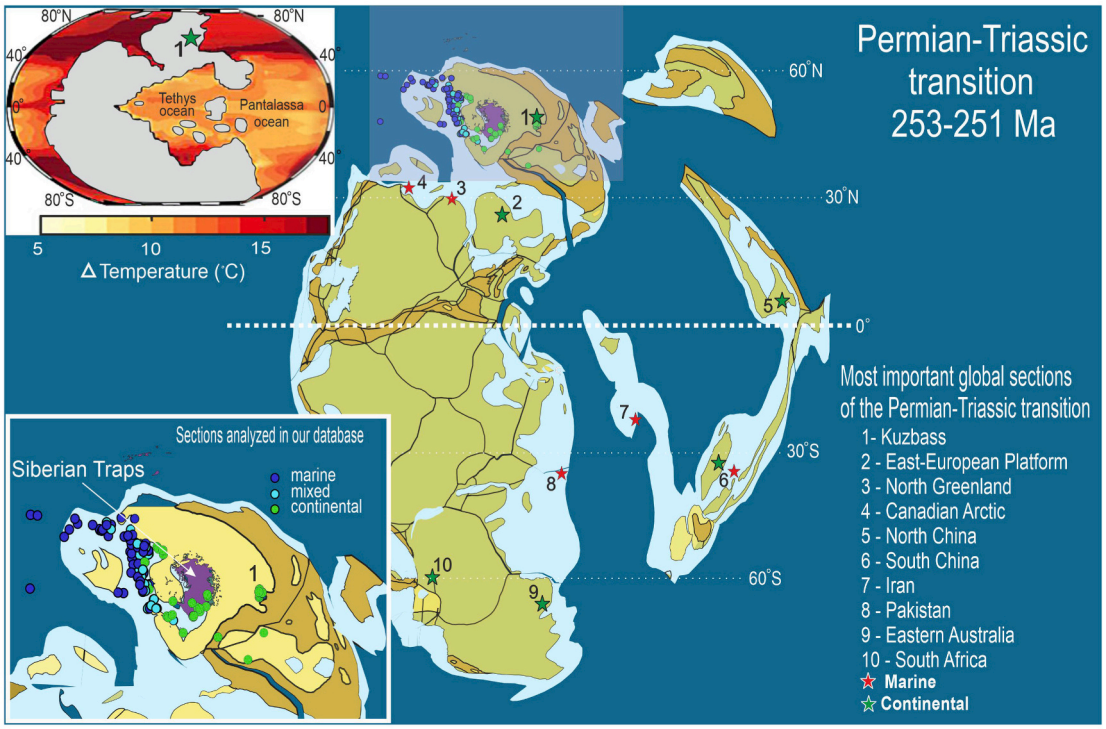

Fig. 1. Global paleogeographic map for the Permian-Triassic transition (PTT) (Developed with the open-source and cross-platform plate reconstruction software *GPlates* (http://gplates.org) and geographic information system *QGIS* (https://www.qgis.org) (Müller et al., 2018). The paleogeographic geometries utilized from datasets of Cao et al., (2017). Stars indicate position of the main Permian-Triassic sections (marine and terrestrial) mentioned in the text. The upper left insert is a paleogeographic map of near surface (0 to 70 m) ocean warming across the PTT (modified from Penn et al., 2018); grey - the continent Pangea and Cimmerian blocks within the Tethys ocean. Note that the greatest temperature increase (delta 15° C or more) occurs in the middle-high latitudes in both southern and northern hemispheres. The lower left insert: analyzed sections in this study (see sections 4.10 and 5.8 for details, list of the sections and their location in the supplemental Table S1-S3). Map from (Cao et al., 2017) and *EarthByte* Large Igneous Provinces and Volcanic Provinces for *GPlates* URL: https://www.earthbyte.org/gplates-2-2-software-and-data-sets/ (Whittaker et al., 2015; Johansson et al., 2018).

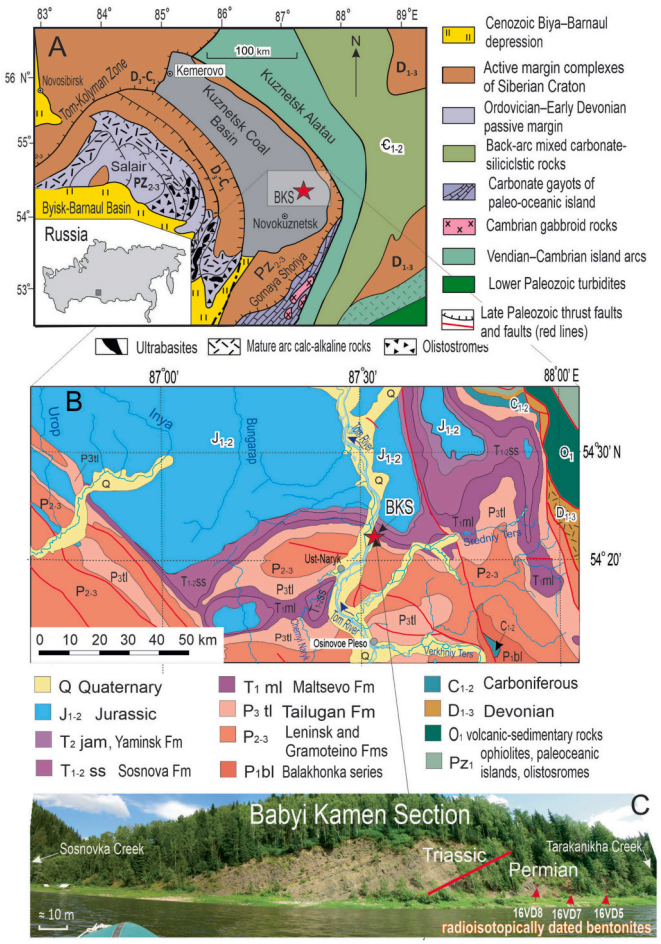

Fig. 2. Geologic and geodynamic framework of the Kuznetsk Basin and adjacent areas. (A) Structural map of the Kuznetsk Basin and adjoining regions. (B) Geologic map of the east-central part of the Kuznetsk Basin (modified from Babin, 2007 unpublished). Red star shows the position of Babyi Kamen section (BKS). (C) View on the Babyi Kamen section along the Tom River, Kuznetsk Basin, Russia. (For interpretation of the references to colour in this figure legend, the reader is referred to the web version of this article.)

adjacent territories, including the Tunguska Basin, Taymyr, Kuznetsk Basin, Verkhoyanie, and Omolon, should be the first and most severely affected victims of the eruptions. However, it was noted that the mass extinction seems to have had less profound effects on the regional land plants and insects (Shcherbakov, 2008; Aristov et al., 2013; Nowak et al., 2019), although different interpretations of the insect and plants biodiversity might be related to age constraint problems in these terrestrial settings.

In the mid-latitudal zones (temperate climate belt within 45–60° N and S) the pattern of regional/local extinction differs from the pattern in South China. In the Canadian Arctic (~50°N during P-T transition) a regional extinction of sponges in marine succession named as the "Arctic extinction event", appears at least 100 kyr prior to the latest Permian mass extinction (Algeo et al., 2012), as it is defined in South China (Shen et al., 2019). In the opposing southern hemisphere, within the Sydney Basin of Australia (~65–75°S), the main end-Permian continental extinction event occurs even earlier, within the analogues of the middle of the *Clarkina changxingensis–C. deflecta* conodont zone of South China (Fielding et al., 2019) and about 400 kyr earlier than the PTB at Meishan (Yin et al., 2001; Shen et al., 2011).

Although the Kuznetsk Basin (Kuzbass) occurs on the periphery of the Siberian Traps and its products distribution (Figs. 1, 2), the basin possessed massive basalt traps in Triassic (Saltymakov complex) and sill bodies within its Carboniferous-Permian strata (Syrkash complex) (Buslov et al., 2010). Therefore, the detrimental effects of the flood basalt volcanism in the Kuznetsk Basin may have been of similar scale as in the main area of Siberian Traps distribution (Tunguska and Taymir basins). The taxonomic records of floral and faunal succession within the Permian-Triassic transition in the Kuzbass and surrounding regions are in fact well documented (Figs. 1, S1-2) (see list in supplemental Fig. S3, Table S1).

The goals of the present study are to (a) document sedimentological, geochemical, paleomagnetic proxies and biotic evolution patterns during the Permian-Triassic transition in the Kuzbass and in the entire Siberian region, (b) better understand the environmental changes during the transition through the geochemical and biotic proxies, (c) constrain the biotic and regional climate events in terms of the International Geologic Time Scale (IGTS) via high precision CA-IDTIMS U-Pb zircon dates, geochemical and paleomagnetic proxies and quantitative correlation tools (CONOP); (d) compare the recognized Kuzbass events with those established worldwide, especially with the events in tropical South China, and the middle-high latitudes (northern Pangaea and Gondwana).

2. Geological settings

The Kuznetsk Basin (Kuzbass) is located in the northern part of the Altai–Sayan Folded Area, southwestern Siberia. In the northwest it is bordered by fold and thrust belts and shear zones that deform Paleozoic rocks and generally verge towards the basin interior (Fig. 2A). In the northeast, it is bordered by the Paleozoic Salair and Tom-Kolyvan Zone. In the south and the east, the basin is bounded by the Gornaya Shoriya and Kuznetsk Alatau mountainous systems, respectively (Fig. 2A). All four regions form part of the vast Altaid collage, which is the orogenic belt that constructed much of the basement of eastern Central Asia during the Paleozoic (Buslov et al., 2010; Davies et al., 2010). The Mississippian succession is carbonate-dominated and is exposed along much of the Kuznetsk Basin margin. These Kuzbass carbonates belong to a widespread Upper Devonian–Carboniferous platform across southern Central Asia. Up to 7000 m of Upper Paleozoic continental coal-bearing sequences (Serpukhovian-Changhsingian) unconformably overlie the Visean-Devonian carbonates, and in turn are conformably or with slight unconformity overlapped by the Triassic siliciclastic, volcaniclastic, and volcanic sediments (Fig. 2B, C). The Jurassic coal-bearing molasse sediments are separated from the overlying and underlying rocks by sedimentation breaks and structural unconformities (Buslov et al., 2010). Several marine horizons (ingressions) are recognized in the lower and upper Permian (Bogomazov et al., 1996). The upper Permian (Lopingian) is the most productive in the regional Kolchugin Series, possessing a thickness of over 4200 m. The Permian-Triassic transition of the Kuzbass region plays a key role in the entire Siberian region as it has the most complete and well exposed succession with abundant fossils – flora, non-marine ostracods, gastropods and bivalves, conchostracans, insects and fish remain.

3. Materials

The Permian-Triassic transition in the Kuznetsk Basin has been studied in a well exposed section at Babyi Kamen (BKS), on the right bank of the Tom River, about 80 km downstream from Novokuznetsk city, South Siberia, Russia (the base at 54.383780 N 87.535120° E, the top at 54.392823°N 87.531947°E) (Figs. 2B,C, S1-S3). We measured in details at Babyi Kamen stratigraphic section (BKS) the succession from the Upper Permian upper Tailugan to the top of the Upper Permian-Lower Triassic Maltsev Formations (Figs. 2–3, S1-S3). Over 500 fossil specimens were collected from within the BKS (Table S1), including non-marine bivalves (150 specimens), gastropods (37 specimens), ostracods, conchostracans (350 specimens), plants (over 200 specimens), and fish remains (61 specimens). Also collected in this context were 331

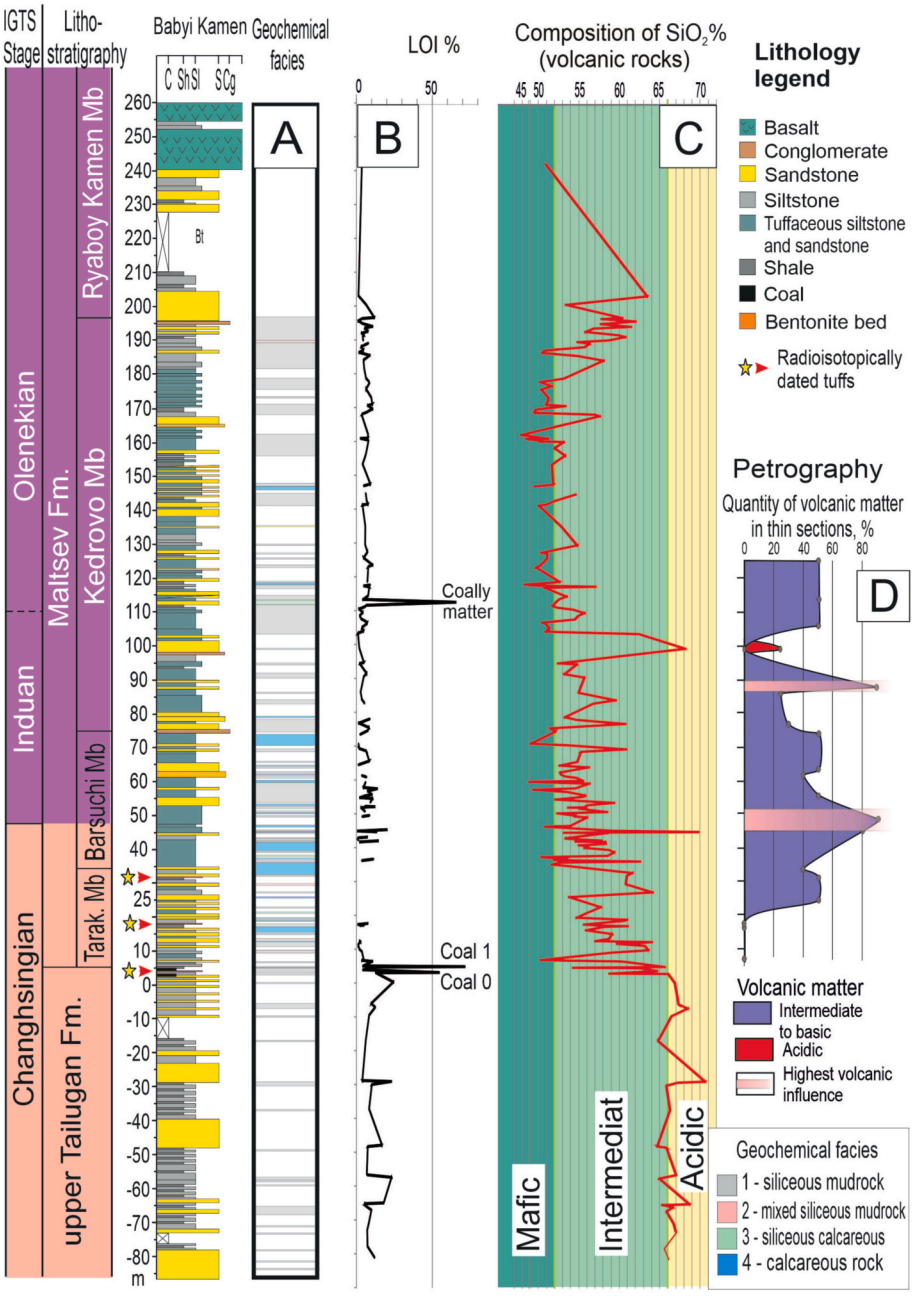

Fig. 3. Geochemical facies, total organic carbon (TOC), and proxies for the volcanic composition in Babyi Kamen Section. A, geochemical facies according to (Baumgardner et al., 2014); B, LOI % ~ TOC; C, composition of SiO_2% in volcanic rock from bulk geochemistry following to Hayashi et al., (1997). Composition: 66–76% acidic, 52–66% intermediate, 45–52% basic; D, composition of volcanic rock from the petrographic study.

samples for geochemical studies (204 for bulk geochemistry, 127 for $\delta^{13}C_{org}$ geochemistry), 160 samples for paleomagnetic studies, 27 samples for radioisotopic age studies and 25 samples for petrographic study (Fig. S1-S9, Table S1).

Well-preserved flora and fauna fossils were collected from the upper Tailugan Formation and entire Maltsev Formation in the present and our previous studies (Karasev, 2015; Dmitriev et al., 2018; Davydov et al., 2019a; Davydov et al., 2019b; Yan et al., 2019; Zharinova, 2019; Silantiev et al., 2020; Silantiev and Urazaeva, 2021; Felker, 2021, (in press)) (Figs. S4-S9). Our original collections were combined with the previously published and unpublished data from this section (Table S1-S2). Fossils were carefully sought bed by bed throughout the stratigraphic sequences. Among abundant insects found in Babyi Kamen and their collections include more than 900 specimens of 17 orders, 28 families, 23 genera and 28 species of the insects (Aristov et al., 2013).

The fossil material in this study is stored in the following institutions: Plants, insects and fish remains – Paleontological Institute of Russian Academy of Sciences, Laboratory of Paleobotany coll. No 5542.; conchostracans, non-marine bivalves, gastropods and ostracods Stuckenberg Museum of Kazan Federal University collections KFU BK1, BK3 and Novokuznetsk Geological Museum, Kuznetsk province (NGM BK3/65–60).

Besides the rock material, we compiled the available published literature and unpublished reports that we were able to obtain (Fig. S1 and Table S2). These abundant sources have been used to develop a database that includes the data from the continental and marine Permian and Triassic sedimentary rocks throughout Siberia. These data were utilized to develop the model of evolution of continental and

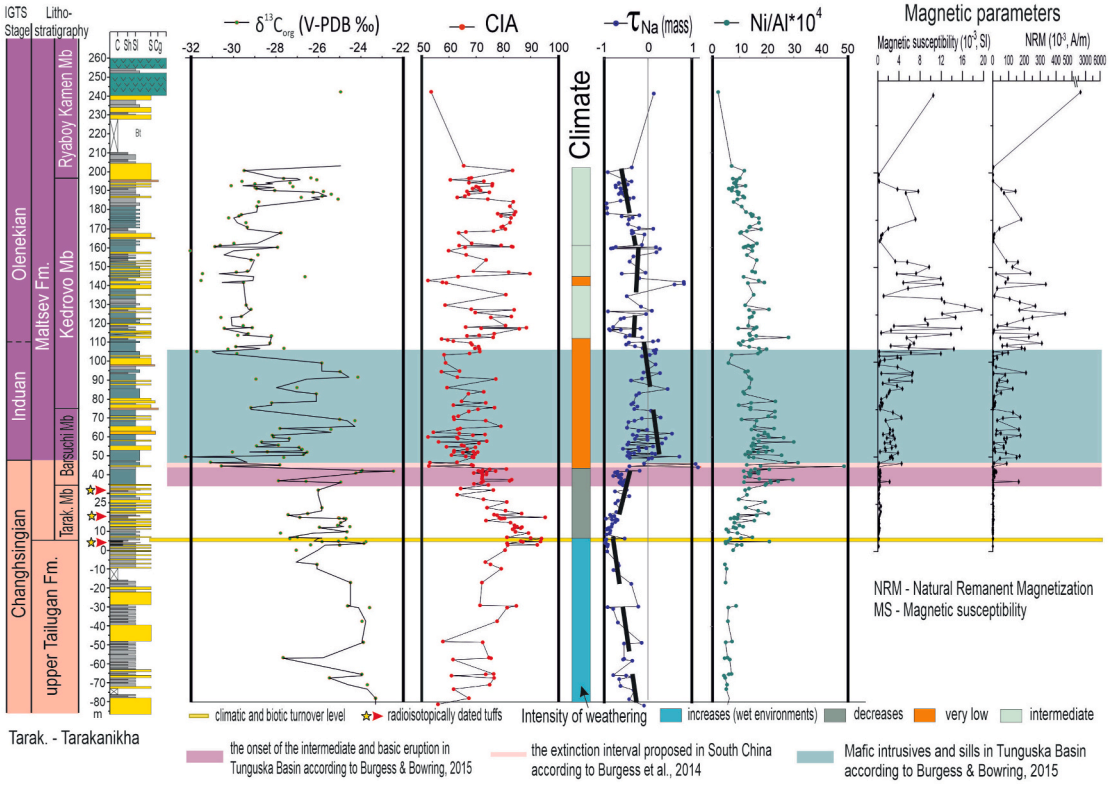

Fig. 4. Different geochemical and magnetic parameters in Babyi Kamen Section.

marine biotas across Siberia. More details regarding the database and data analyses are provided in the sections 4.10 and 5.8.

4. Methods

4.1. Sedimentology

The Babyi Kamen section was measured utilizing a tape at the centimeter to meter scale (Fig. S2, S3). No faults, folds and other tectonic complications were observed during measurements (Fig. 2C). The section is completely exposed along the Tom River, especially well in late summer and autumn (Fig. 2B, S2). The rocks were subdivided into units (bedsets) with a unified lithology. Strike and dip of bedding were measured, but no significant inclination changes are observed in the BKS (Fig. S2). GPS measurements were taken every 25–30 m for the position reconciliation. The section was logged bed by bed and sampled for analyses of paleomagnetic properties, bulk geochemistry, organic carbon isotope studies and for radioisotopic dating as the section was described and where proper rocks were found. The sedimentology has been carefully documented throughout the succession (Fig. S3).

4.2. Bulk geochemistry

The contents of oxides of rock-forming and minor elements from the sedimentary rocks of the BKS were analyzed by X-ray fluorescence analysis (XRF). 205 samples were collected from 59 levels throughout the studied succession (Figs. 3–4, S3, Table S1). Crushed samples were placed in a grinding set of a planetary ball mill, and grinding was carried out for 10 min to achieve the required particle sizes of less than 10 μm.

A 0.5 g aliquot of powdered sample was placed in a ceramic crucible and calcined at 1100 °C for two hours to determine the loss on ignition (LOI). A second aliquot sample with mass of 4 g was weighed on an analytical balance with an accuracy around 100 mg and then mixed with organic wax and pressed onto a substrate of boric acid with a force of 300 kN as a tablet. The elemental composition of the bulk rock was studied on a tablet that was analyzed with the standard Geoquant technique on a S8 Tiger X-ray fluorescence wave dispersion spectrometer (Bruker, Germany) with 4 kW rhodium tube, which allows one to determine the elemental composition of solid, powder, and liquid samples in the range from B to U in a vacuum or helium atmosphere. The obtained spectra were processed by the method of fundamental parameters, automatic recognition errors, spurious peaks were removed, diffraction phenomena and matrix effects were considered; the SPP value was used to consider the undetectable elements.

The volcanic contribution to the sedimentary rock was evaluated with the formula from Hayashi et al., (1997), where the SiO2 content in volcanic rocks can be estimated from the Al_2O_3 / TiO_2 ratio using the following expression: SiO_2 (wt%) = 39.34 + 1.2578 (Al2O3 / TiO2) - 0.0109 (Al_2O_3 / TiO_2). The obtained values of SiO_2 (wt%) In the range of 45–52% correspond to mafic volcanism, 52–66% - to intermediate volcanism, and 66–76% - to acidic volcanism.

4.3. The LOI (loss on ignition)

The dissolution of the carbonate fraction in this analysis was not performed. The procedure for determining LOI was as follows: A dry sample of approximately 0.5 g was placed in a ceramic crucible and weighed on an analytical balance with an accuracy of 0.1 mg, then the sample was calcined at 1100 °C in a muffle furnace in for two hours. After calcination, the sample was weighed again, the difference in the sample mass before and after calcination was determined, and then the percentage of weight loss relative to the initial sample mass was calculated (Table S1).

4.4. $\delta^{13}C_{org}$ organic carbon isotopic

The $\delta^{13}C_{org}$ organic carbon isotopic composition of siliciclastic rocks was measured by mass spectrometry in 127 samples, collected from 51

levels (Fig. 4, Table S1). The carbonate component in this analysis was removed. The isotopic composition of organic carbon in the rock samples was analyzed on a Delta V Plus isotope mass spectrometer (ThermoFisher Scientific, Germany) with a Flash HT attachment in continuous flow mode. The carbonate component was liberated from a 500 mg aliquot by adding of 10% hydrochloric acid solution until the cessation of reaction, followed by evaporation at 80 °C until to a dry residue. The residue was weighed on a XP6 microbalance (Mettler Toledo, Switzerland) and approximately 200 μg is transferred to a tin crucible. Using an autosampler, each sample crucible is discharged into a helium-blown quartz reactor filled with chromium oxide and copper wire at a temperature of 1020 °C. As a result of the reaction with chromium oxide, tin is converted to oxide, and the sample completely burns with the formation of carbon dioxide. Carbon dioxide is transferred to the mass spectrometer using a helium stream, after passing through a desiccant and a chromatographic column at a temperature of 45 °C. Before the measurements, several portions of standard carbon dioxide with a known carbon isotopic ratio are introduced into the mass spectrometer to calibrate the isotopic ratio. Standard reference materials are analyzed for additional control in a series of samples: USGS-40, which is L-glutamic acid with a known carbon isotopic ratio, and IAEA-CH-7, which is a polyethylene film with a known carbon isotopic ratio.

4.5. Weathering intensity

The following weathering indices were utilized to assess the weathering intensity (paleoclimate): 1) - Chemical Index of Alteration CIA ($CIA = [Al_2O_3 / (Al_2O_3 + Na_2O + K_2O + CaO^*)] \times 100$), where all oxides are in molar units and CaO* represents the CaO in the silicate fraction of the rock (Nesbitt and Young, 1982; McLennan S.M. et al., 1993);

2) - Sodium depletion index τNa $[Na_5 / Zr_5) / (Na_p / Zr_p) - 1]$, where subscripts s and p represent the contents of corresponding elements in sediments and protolith, respectively (Rasmussen et al., 2011). The average composition of upper continental crust from (Rudnick and Gao, 2014) was used to calculate τNa in the BKS (Fig. 4). The parameter τNa is sensitive to sedimentary recycling and sorting-induced accumulation of quartz and zircon, which generally does not affect the CIA value (Garzanti et al., 2013).

4.6. U-Pb geochronology

Heavy minerals were separated from hand samples by conventional density and magnetic methods. All prepared zircon separates were placed in a muffle furnace at 900 °C for 60 h in quartz beakers to anneal minor radiation damage; annealing enhances cathodoluminescence (CL) emission (Nasdala et al., 2002), promotes more reproducible interelement fractionation during laser ablation inductively coupled plasma mass spectrometry (LA-ICPMS) (Allen and Campbell, 2012), and prepares the crystals for subsequent chemical abrasion (Mattinson, 2005). Hand-picked aliquots of grains were then prepared as 1-in. diameter cold-mounted two-part epoxy mounts, ground to the average center of grains, and polished with SiC lapping film and 0.3 μm alumina. The finished mounts were carbon coated, and digitally photomicrographed in cathodoluminescence (CL) using a Gatan Mini-CL detector mounted on a JEOL T300 scanning electron microscope. From these compiled images, selected grains with consistent CL zoning patterns were picked for chemical abrasion isotope dilution thermal ionization mass spectrometry (CA-IDTIMS).

U-Pb geochronology methods for isotope dilution thermal ionization mass spectrometry follow those previously published by Macdonald et al. (2018). Individual zircon crystals were subjected to a modified version of the chemical abrasion method of Mattinson (2005), whereby single crystal fragments plucked from grain mounts were individually abraded in a single step with concentrated HF at 190 °C for 12 h. U-Pb dates and uncertainties for each analysis were calculated using the algorithms of Schmitz and Schoene (2007) and the U decay constants of Jaffey et al. (1971). Uncertainties are based upon non-systematic analytical errors, including counting statistics, instrumental fractionation, tracer subtraction, and blank subtraction. These error estimates should be considered when comparing our $^{206}Pb/^{238}U$ dates with those from other laboratories that used tracer solutions calibrated against the EARTHTIME gravimetric standards. When comparing our dates with those derived from other decay schemes (e.g., $^{40}Ar/^{39}Ar$, ^{187}Re-^{187}Os), the uncertainties in tracer calibration (0.03%; Condon et al., 2015; McLean et al., 2015) and U decay constants (0.108%; Jaffey et al., 1971) should be added to the internal error in quadrature. Quoted errors for calculated weighted means are thus of the form ±X(Y)[Z], where X is solely analytical uncertainty, Y is the combined analytical and tracer uncertainty, and Z is the combined analytical, tracer and ^{238}U decay constant uncertainty.

4.7. Bayesian age modeling

We used the Bayesian age modeling software modified Bchron (Trayler et al., 2020), an open-source R package evolved from the package Bchron (Haslett & Parnell, 2008) for deep time applications. These packages are identical in their use of a compound Poisson-gamma distribution of accumulation events under the constraint of stratigraphic superposition to describe the prior probability of an ensemble of piece-wise linear sedimentation paths, which are conditioned by likelihood functions describing dated horizons (Haslett & Parnell, 2008). Additionally, modified Bchron uses an adaptive proposal algorithm in its Markov Chain Monte Carlo engine to remove any necessity for user scaling of the space or time domains, and still ensure effective and efficient sampling of the posterior parameter distributions (Trayler et al., 2019). Above and below the dated horizons, the posterior samplings for the first and last pairs of dated horizons were linearly extrapolated to yield a median and credible interval.

4.8. Paleomagnetic study

Analyses of 150 samples, from which the primary components were recovered in 95, represent the characteristic high-temperature component of magnetization of different polarity (Figs. 4, S10). Within the interval of 3 to 120 mab (meters above the base), samples were taken on average every meter (Fig. S3). Upward, from 120 mab up to about 200 mab, samples were obtained every 2–3 m. In 2016 the collected large hand samples were oriented with Brunton compass and several one-inch cylinders from each sample were drilled in the laboratory of the Institute of Geology and Oil-Gas Technologies of Kazan Federal University. In 2018, field sampling was carried out with a drilling equipment. Two or more cylinders from each sample were available for the paleomagnetic analyses. The sedimentologic affinity of each sample can be seen in Fig. S3. The average paleomagnetic directions were calculated for the high-temperature component of the normal and reverse polarities, as well as the average for all samples (Fig. S10) (Kuzina et al., 2019a, 2019b).

4.9. Petrographic studies

The volcanic and volcaniclastic components and their amount and composition in the Permian-Triassic transition at Babyi Kamen' section have been studied by petrographic analysis. The study was conducted utilizing a Carl Zeiss AxioLab polarizing optical microscope equipped with an Axiocam 506 colour digital camera. Twenty-five samples were evenly collected throughout the main part of the section from the Tailugan Formation into the Barsuchi Member of Maltsev Formation (7.1–125.2 mab) (Fig. S3) and petrographic thin sections were prepared from each sample (Table 2). No volcanic or volcaniclastic materials are found in the Tailugan Formation but have been recognized in bedsets 11

through 30 (24.6–125.5 mab) in the Maltsev Fm (Fig. 3C). The prevailing lithotypes there are tuffaceous siltstone and sandstone (Fig. S3). The siliciclastics consist mainly of angular or slightly rounded quartz grains and corroded fragments of siliceous and metamorphic rocks (Figs. S12-S16).

4.10. Databasing and quantitative stratigraphy

In order to integrate all types of the data that we obtained in our study with those from published and unpublished sources into the content of the International Geologic Time Scale, we developed the web accessible PTB Siberia project database (DB) and additional tools to operate with CONOP (Constrained Optimization) (Sadler, 2006) quantitative correlation methods and corresponding software. The DB includes 99 references and 23 unpublished sources, 21,000 events in 453 sections and 123 unpaired events (magnetozones, coals, bentonites, radioisotopic ages and several others); the taxonomic dictionary comprises 6149 taxa of marine and non-marine animals and plants.

We did not include insects in the compositing process, as they are relatively rare in the Permian and Triassic of Siberia. In BKS, rare specimens occur in in lower part of Tarakanikha Member (Fig. 10). The most abundant assemblage of insects in the Kuznetsk Basin found in the narrow horizon in the uppermost Barsuchi Member, at 188–189 m above the base (Fig. 10). Among identified 17 orders, 28 families, 23 genera and 28 species of the insects, eleven genera and 28 species are endemic (Fig. 10). All orders and families and non-endemic genera in the BKS are ranged from the Changhsingian through mid-Olenekian with no extinct taxa around the end-Permian extinction event of South China. Four families that are elsewhere known from the late Permian disappear at the mid-Olenekian and four families first appear at this stratigraphic horizon (Fig. 10). One newly described family Babalidae (Aristov 2020) is endemic. All other families that are recognized in Babyi Kamen are known elsewhere at least in the upper Permian and Lower Triassic (Fig. 10). A short summary on the insects in Babyi Kamen can be found in the supplemental files.

For the analysis of the DB, tools based on external services have been integrated (GPLATES software, QGIS software and others). For the data input we utilized Google Sheet utility to be able to work remotely from different sites (USA, Florida and Russia: Kazan, Moscow, Yakutsk, Magadan). The system integrated Google Sheet (GS) tables were run through the newly developed on-line engine, Conman Online, a web application at https://conman.online developed in this project to operate with the quantitative stratigraphic tools including CONOP (constrained optimization, (Sadler, 2006). Conman Online converts our Google Spreadsheets (GS) data into CONOP9 format input files. This approach speeds up the process of obtaining the input files and lets the user directly and efficiently reach any data in the DB (references, sections, taxonomy, events, unpaired events). The minimalistic interface of Conman Online and defined presets for the input files make this application very useful in the integration and analysis of data. The presets in the input files for the Conman online quickly generate an unlimited number of input files for the CONOP9 with different sets of sections. The interaction of the user is restricted to one button on the screen. When the button is clicked, the Conman Online downloads the selected sections from our database GS tables and converts them into CONOP input files. The manipulation with the parameters of the input files (level of the taxonomy, number of the sections with common taxa, what clades include-exclude, synonyms, level of synonymy and several other) can be done in a special GS table that is integrated into the database. Our other application is the COMPARESEC tool, which is developed for the analyses of the integrated data obtained from the CONOP9 analyses. The input file for the application is directly imported from CONOP9 (cpcht.txt). The application in the first step builds the range-through diversity graphics for each of the selected clades or other taxonomic entities of flora and fauna. The package Shiny for the R language and the Shinyapps platform for hosting our Shiny web application is utilized (RStudio Team, 2015). The COMPARESEC application retrieves from cpcht.txt file ranges of the taxa selected for the analyses, and links those with the taxon dictionary in our database GS. The composite is divided into bins and four types of the taxa (N_{fl} - single-interval taxon (appears for the first and last time in the interval); N_t - top crosser; N_b - bottom crosser; N_{bt} - bottom and top crosser) proposed by Foot (2000) and Alroy (2014) are calculated for each bin. Then, the taxon ranges are summarized and replicated in the graphics (Figs. 7–10). The COMPARESEC tool can analyze the stratigraphic distribution of any taxa within the developed composite and trace any stratigraphic range and taxon throughout the sections, included for the developed composite section. The COMPARESEC application is accessible through https://mironcat.shinyapps.io/comparesec. All developed applications and DB can be downloaded on the local workstation and utilized in offline environments.

We utilized the approach that was successfully used in our previous studies (Davydov et al., 2010; Schmitz and Davydov, 2012) to develop and calibrate the composite section of the entire Permian and Lower Triassic in Siberia with CONOP quantitative correlation tool (Sadler, 2006) (Figs. 11–12, Table S2).

Three types of the sections were analyzed in the compositing process: marine, mixed marine-continental and pure continental (Fig. S1). The marine sections occur in Taymir (mostly Triassic), northern and eastern passive margins of Siberian Platform (Verkhoyanie foredeep), in Omolon and Okhotsk Microcontinents, and in a series of deep-water basins between these Microcontinents and the passive margin of the Siberian Platform (Ayan-Yuryakh, Balygychan Sugoy basins) (Davydov et al., 2016). Continental sections occur in the Tunguska and Kuznetsk Basins and northern Kazakhstan, and mixed marine-continental sections occurs in the west from the marine sections of Verkhoyanie foredeep (Fig. S1).

The compositing process divides into several steps: (1) constructing an overall ordering of events (ordinal composite sequence) compiled from a database that involves both biologic paired events (first and last occurrences of taxa, for which range extensions are allowed) and unpaired dated events (radiometrically dated ash beds) in a variety of stratigraphic sections; (2) scaling of the intervals between events in the composite sequence according to the relative position of events in all the measured sections and constrained by the absolute positions of dated events and conventionally proposed stadial boundaries, after the observed ranges have been extended and missing taxa inserted to match the best-fit composite sequence; (3) identifying key index taxa to locate the relative age of standard zone and stage boundaries within the scaled composite section and assign the absolute age in according with the International geologic timescale [IGTS] (Henderson et al., 2012; Ogg, 2012); and (4) absolute numerical calibration of all events (including standard zone and stage boundaries) in the composite via the radioisotopically dated ash beds and conventionally established IGTS stage boundaries (Schmitz and Davydov, 2012). The results of the compositing are presented in Table S2.

5. Results

5.1. Sedimentology

Six elementary progressive cycles incising each other and forming coastal-floodplain coal-bearing deposits of the Tailugan Formation were recognized in the lowest part of the BKS, (minus 2 to 4 mab). In the overlaying Maltsev Formation (Neiburg, 1936; Radchenko, 1973; Betekhtina et al., 1986), bedsets 5–9 (7.5–12.5 mab) represent a coastal pro-cycles, shallow-basin, light-grey siltstones with a conchoidal fracture (Fig. S3). Bedsets 10 and 11 (12.6–16 mab) are represented by the coastal fine- to medium grained sandstones, with ripple marks are visible, imprints of fossil flora and conchostracans. This is the regressive part of a large cycle, possibly delta, with a capacity of more than 12–15 m. Such rocks associations are sometimes characteristic of the near-edge areas of the coast of paleo-basin. In the bedsets from 12 to 17 (21.0–45.0 mab), basal shallow levels (prograding cycles) compose a thick (22.2 m)

meso-cycle, represented mainly by fine-grained siltstones (Fig. S3). Bedset 18 (45–55.5 mab) is similar to the underlying cycle, but the presence of tuffaceous material and randomly distributed analcime-rich siderite nodules are observed in the field. Siltstones of the bedset 18 at 53 m pass into sandstones enriched with tuffaceous material. Bedset 19 (55.5–61.0 mab) consists of coastal-marine fine-grained siltstones with concretionary interbeds of the flyschoid type and an admixture of tuffaceous material. There are large coarse sandy coastal "tongues" and/or lenses in beset 20 (61.0–65.0 mab). Bedsets 16 through 22, inclusive, are assigned to the Barsuchi Member, and represented mainly by fine-grained siltstones.

In general, the overlying part of the described section is represented by significantly more highly dynamic prograding cycles, in which their basal levels are represented by medium-coarse-grained sandstones wrapped in "rolls" with convolute bedding. Above, at the bottom of bedset 22 (73.3–76.0 mab), there is another highly dynamic level, represented by rapidly pinching out coarse-grained sandstones, gravel conglomerate and conglomerate. Similar conglomerate occurs at the bottom of bedset 25 (97.5–100.2 mab). The dynamics of this gravitational process decrease upwards (Fig. S3).

5.2. Bulk geochemistry and climatic proxies

The geochemical measurement results are presented in graphical form in Figs. 3–4. Geochemical facies were determined by Si, Al, K, Ca (Fig. S11), utilizing the method of (Baumgardner et al., 2014). This method is a rather convenient evaluation system of lithophilic elements for classifying siliciclastic rocks (including fine-grained ones) in terms of geochemical facies, since it uses the ratio of residues (Si is represented in the diagram); hydrolysates (the diagram shows Al, K) and carbonates (the diagram shows an increased Ca content) Ca). Most of the samples belong to the geochemical facies 1 (*siliceous mudrock*). The second most common is the geochemical facies 4 (*calcareous mudrock*). Samples from geochemical facies 2 (*mixed siliceous mudrock*) and 3 (*siliceous calcareous mudrock*) are rare.

The most substantial indicators of the composition of the studied samples are SiO_2, Al_2O_3, TiO_2, Fe_2O_3, Na_2O, K_2O, CaO, MgO, MnO, P_2O_5; Sr, V, Cr, Cu. In the group of "siliciclastic elements" (SiO_2, Al_2O3, TiO_2, Fe_2O_3, Na_2O, K_2O), abnormally high levels are noted in the calcareous beds at 40–55 m above zero of the section (mab) (Fig. S11), in which a decrease in the concentrations of these oxides is observed. The prominent increase of the concentrations of CaO, MgO is observed in this interval as well. An abnormally high V content is seen at 112.5 mab (coaly bed) (2435 ppm), and a low V content in - 73 mab (57 ppm). The concentration of this element in the rest of the samples varies between 100 and 400 ppm (Fig. S11). The content of Mn and Cr increases in calcareous rocks and is especially anomalous (about an order of magnitude greater than in other beds) in bedsets 16c – 21 (31–73 mab) (Fig. S11).

The following outstanding geochemical events can be observed in the graphics of the geochemical indicators for the section (Figs. 3–4). There are coal benchmarks at depths of 3.1 mab (sample G2, layer −1, LOI 54.4%), 4.85 mab (sample G5, bedset 1, LOI 71.33%), 112.5 mab (sample G45, bedset 27c, LOI 65.36%). The last sample is characterized by an abnormally high V content (996 g / t) (Figs. S11). Within the interval 35.3–71 mab (the zone of the bedsets 16–21) are abnormal fluctuations in the Mn and Cr contents, with the most crowded range of the fluctuations within 35.3–64 mab. There are peaks of acidic magmatism within the lower Barsuchi Member, where dominant magmatic component is intermediate in composition, at the depths of 44.9 m (sample PM35, top of the bedset 17, SiO_2 content by Hayashi 69.66%), 99 m (sample PM56, layer 25, SiO_2 content by Hayashi 68.04%). The geochemical data interpreted as magmatic distributions and compositions are well correlated to the interpretations from petrographic analysis (see above).

The magmatic component in the sedimentary rocks was established according to the SiO_2 indicator proposed by Hayashi (Hayashi et al., 1997). The composition of magma varies from acidic composition (Tailugan Formation −80 to 3 mab) to intermediate magma (Tarakanikha Member of Maltsev Formation within 3–35 mab) and intermediate to basic magma within 35–195 mab (Barsuchi and Kedrovsky Member). At 45 and 98–103 mab (bedset 18) abnormal and very narrow peaks of acidic magmatism are distinguished (Fig. 3C). The magmatic component is consistent with the Ni/Al ratio within the BKS.

The LOI (loss on ignition) values are usually considered comparable to organic matter content. In the upper Tailugan Formation it is around 20% in average, but drastically decreases above the last Permian coal bed at 5.0 mab. Immediately after, the LOI decreases to less than 10% from 5 to 35 mab (Fig. 3B). The LOI is still low between 35 and 75 mab, except for the presence of sharp peaks (up to 30%) in the values associated with calcareous facies (Table S1) From 75 mab to the top of the section the LOI is less than 10%.

The variation in δ^{13}Corg values is shown as measurement points and a trend line constructed using linear filtering at a value parameter points equal 2. The organic carbon isotope values in the Tailugan Formation (−80 to −5 mab) are relatively stable, i.e., around −24‰ (Fig. 4, Table S1). Within the Tarakanikha Member of Maltsev Formation (5 to 35 mab), the variation ranges from −24‰ to −28‰. The sharpest changes occur within the lower Barsuchi Member (45–50 mab), with a negative carbon isotope excursion down to value as low as −32‰, returning to −27‰ within a few meters (Fig. 4, Table S1).

The Ni/Al x10^4 index is considered as an indicator of Siberian Traps eruption in southern latitudes (Fielding et al., 2019), and was obtained in our study of the BKS. In the upper Tailugan Formation, the Ni/Al ratio has little variance with values of around 5.0. In the very top of the Tailugan Formation and into the Tarakanikha Member, this index gradually rises to a value of 20 with greater variance (Fig. 4). The greatest value of the Ni/Al ratio occurs at 45.5 mab, where an excursion reaches a value of 50, which is an order of magnitude higher than in the Tailugan Formation. The Ni/Al ratio varies from 15 to 30 in the rest of the stratigraphy and doesn't decrease to levels less than 5.0 until the Ryaboi Kamen Mbr. The Ni/Al ratio correlates with the level of changing magmatism from acidic to intermediate-basic according to the Hayashi index (Figs. 3C-4).

5.3. Evaluation of weathering intensity

Overall, the τNa values vary from −0.99 to +1.18, averaging −0.41 ± 0.33. The interval up to the level of 6,4 mab, above the coal 1 (Fig. 4, S11), encompasses an increase of CIA values from 55.9% to 94% and a decrease of τNa from a baseline of ~ − 0.00 values to −0.97. CIA values then recover to a baseline of ~52% at the level around 45 mab and τNa values increase to a baseline of ~ + 1 at the level 44.7 mab. The interval 44.7–111.6 mab includes CIA values <80% and τNa values between ~ + 0.5 and ~ −0.5 before rising to CIA values varying between ~57% and ~ 90% and falling to τNa values between +0.25 and − 0.95 in the interval 111.6–203 m with a peaked excursion to CIA value 52.2% and τNa value +0.8 at the level of 142.5 m.

According to these indices the weathering intensity (climate humidity) in the Tailugan Formation increases towards the top. In most of the Tarakanikha Member and lower Barsuchi Member (5–43 mab), the weathering intensity rapidly dropped (Fig. 4). In the middle Barsuchi Member (44–111.6 mab), the average weathering intensity is relatively low. The intensity parameter in the upper Barsuchi and Kedrovski Members (113.3–203 mab) is moderate with cyclic fluctuation towards high to lower values of CIA (Fig. 4, S11).

5.4. Paleomagnetism

The results of the paleomagnetic studies within the Permian-Triassic succession in Babyi Kamen section are already published (Kuzina et al., 2019a; Kuzina et al., 2019b) however, the previous results were recently

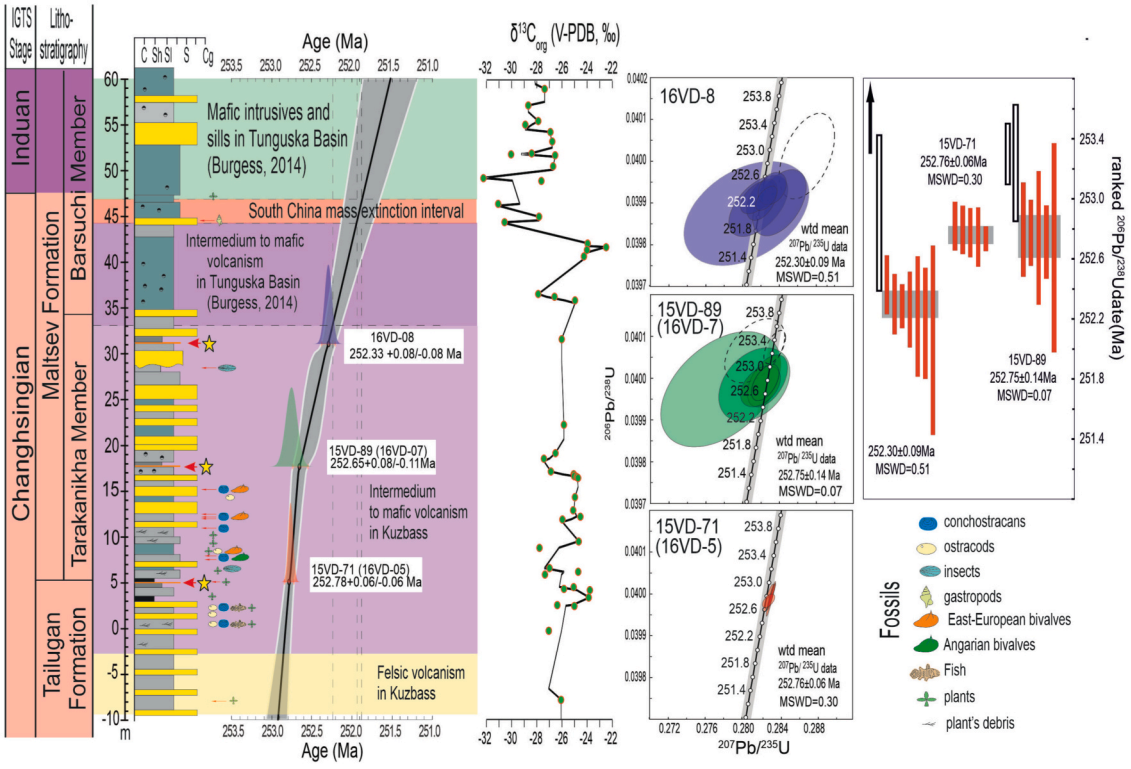

Fig. 5. Babyi Kamen section and modified *Bchron* age model constructed from three radioisotopically dated volcanic tuff horizons. To the right are U—Pb concordia diagrams for each volcanic tuff zircon sample. Conditioning likelihood distributions as weighted mean $^{206}Pb/^{238}U$ zircon ages are represented as normally distributed probability density functions on the age model; posterior ages from the Bayesian analysis are listed to the right of each distribution. Key event horizons including the initiation of Siberian Traps volcanism, end-Permian mass extinction horizon, and Permian-Triassic boundary are extracted from the age model and illustrated. The largest negative organic carbon isotope excursion in the BKS coincides precisely with the predicted level of the mass extinction event in South China.

updated (Fig. S10). Magnetic Susceptibility (MS) values vary over a wide range from $0.06 \times 10^{-5} - 20 \times 10^{-3}$ SI. Natural Remanent Magnetization (NRM) values also fluctuate significantly from 0.26 to 457 mA/m. Basalt samples (2 samples from the upper part of the section) differ in magnetization and reach a value of 6 A/m (Fig. S10). The degree of anisotropy of magnetic susceptibility, except for rare samples, does not exceed 6–7% (Kuzina et al., 2019a).

Two zones with different magnetic parameters can be distinguished in the section. In the Tailugan Fm and in Tarakanikha and lower Barsuchi members (up to 48 mab) of the Maltsev Formation the values of the MS and NRM are remarkably low (Fig. S10). A zone of normal polarity has been recognized in the lower 18 m of the section. Within 19–37 mab in the section, there is a zone with a frequent change of magnetic polarity. It is followed by a zone of stable normal magnetic polarity, which extends up to the level of 89 mab (Figs. 6, S10). It should be specially noted that a sharp change in scalar magnetic parameters (MS and NRM) occurs inside this zone at 48 mab. A frequent change of a small subzone of reverse polarity occurs at 90–95 mab, which is replaced by the continuous zone of normal polarity. Near the top of Kedrovy Member in BKS (165–195 mab), a reverse polarity zone is confidently established (Figs. 6, S10). The sharp changes in magnetic parameters are usually linked to an increase in the input of volcanic origin particles and weathering products of basic magmatism (increase of magnetite and other magnetic minerals). However, this magmatism occurs in BKS much earlier, at the beginning of Maltsev Fm deposition (approximately 800 kyr earlier than the Permian-Triassic boundary, according to our geochronologic studies) and may have different consequent origins.

The magnetostratigraphic zones in BKS were obtained from the established paleomagnetic directions. These magnetic polarity zones are confidently distinguished only when two or more samples are sequentially magnetized in the same polarity (Figs. 6, S3, S10). In the section, the reverse zones are recognized at the intervals 18–34, 50–57, 78–93, 241–256 mab. Zones of reverse polarity were also identified in the upper part of the section based on two samples (166, 195 mab, Kedrovy Member), however no reliable data were obtained between these two samples. Reverse polarity zones are distinguished in the intervals 7–18, 34–49, 57–78, 93–165, 195–203 mab (Figs. 6, S10).

5.5. U-Pb geochronology and age modeling

Three volcanic tuff samples were dated by CA-IDTIMS U-Pb zircon geochronology within the Permian-Triassic transition in the BKS. All three bentonitic horizons contained abundant populations of sharply faceted prismatic zircon crystals with uniform CL zoning patterns. Seven crystals were analyzed from sample 15VD71, near the top of the Tailugan Fm at 5.0 mab. Excluded two older grains interpreted as inherited, the remaining five crystals yielded concordant and equivalent isotope ratios, with a weighted mean $^{206}Pb/^{238}Pb$ age of $= 252.78 \pm 0.06$ (0.14) [0.30] Ma (2 s; MSWD = 0.30) interpreted as the eruption and deposition age of the tuff (Figs. 5, Table S3). Five crystals from the next sample 15VD89 within the Tarakanikha Member at 17.6 mab yielded a weighted mean $^{206}Pb/^{238}U$ age of $= 252.65 \pm 0.08(0.18)[0.11]$ Ma (2 s; MSWD = 0.07). The third sample with abundant volcanic zircons, 16VD08, was collected near the top of Tarakanikha Member at 31.0 mab. Excluding three grains with older, inherited components, seven crystals yielded concordant and equivalent isotope ratios with a weighted mean $^{206}Pb/^{238}U$ age of $= 252.33 \pm 0.08$ (0.20)[0.33] Ma (2 s; MSWD = 0.93 ($n = 7$) (Fig. 5, Table S3). All three samples reside in the uppermost Changhsingian Age of the Lopingian Epoch in the Permian Period of the IGTS (Henderson et al., 2012).

We constructed a Bayesian age-depth model for the BKS in order to provide quantitative interpolation and extrapolation beyond the dated

horizons and transform our proxy records from stratigraphic height into a numerical age reference frame (Fig. 5). According to this model the median accumulation rate in the upper Tailugan Fm and into the lower Tarakanikha Member of the Maltsev Fm at BKS is 106 mm/kyr, a rate that is consistent with accumulation in other coal basins (Hunt, 1988; van Hinsbergen et al., 2015). From 17 mab and above in the section the sedimentation decreases to a median value of 37 mm/kyr (Fig. 5). Most probably the sedimentation in the lower Tarakanikha Member changed transitionally.

5.6. Petrographic results

Chloritized volcanic glasses of intermediate-basic composition appear in the section, starting from PM-20 (bedset 8, 11 mab, Fig. S3, Table S1) - confidently. In sample PM-14 (Fig. S3), the tuffaceous material can only be identified conventionally. Volcanic glasses are traced in each sample from PM 14 upwards (Figs. S12-S16). Volcanic glasses are quite fresh, most glasses have an angular appearance. Chloritization indicates that the glasses have generally basic composition, because this process mainly affects mafic (non-acidic) glasses. Fragments of ultramafic rocks are most likely found in thin section PM-90 (bedset 22, 73.5 mab). In other thin sections, they are either absent, or so strongly altered and cannot be diagnosed. The presence of analcime in thin sections PM-64 (bedset 17, 44.9 mab) and PM-68 (bedset 18, 49.2 mab) is noted. The amount of fresh tuffaceous material of intermediate-basic composition varies unevenly along the section. In the bedset 14–16 (25–43 mab) it is 30–40% of the rock amount, in the bedsets 17 and 18 (43–55 mab) the glass composed of 80–90% rock, which is consistent with the monomineral precipitates of zeolite filling the cores of ostracods and gastropods, which is typical in mafic volcanic tuffs. The siltstone of these bedsets is almost entirely composed of a smectite-like non-translucent matrix and can be assigned to bentonites. It is characterized by a fluid texture typical for effusive rocks. Higher in the section, in the bedsets 20–22 (61–82 mab), the number of volcanic glasses is 40–50%. Bedset 23 (87.3–94.0 mab) again contains a burst of fresh pyroclastic content - up to 80–90%. Then, in bedsets 26, 30 and 33 (103–134.8 mab), the number of volcanic glasses is approximately the same and amounts to 40–50% of the thin section area (Figs. S3, S12-16).

Crystalline zeolite aggregates (analcime?) are developed in the microcracks, nuclei of numerous well-preserved ostracods, and in oval cavities (Fig. S12-16). Zeolitization also occurs in the bulk rock, in which the zeolite content reaches 30%. Zeolite grains are idiomorphic fresh in appearance and filling cracks. In contrast, zeolites in the rocks are strongly altered, metastable, most likely converted to smectite, although exhibiting similar optical behavior as zeolites developed in cracks and cavities. The petrographic data are quite consistent with the magmatic component geochemical proxies (see section 5.2 above) (Hayashi SiO_2 index, Fig. 3).

5.7. Databasing, quantitative stratigraphy and biodiversity

Several goals were achieved in the compositing process:

1. Integrating all types of the data that were involved in the compositing process, including paleontological, geochemical and radioisotopic.
2. Calibrating the entire composite with radioisotopic ages that were previously obtained in Siberia (Davydov et al., 2016; Davydov et al., 2018; Biakov et al., 2020)
3. Calculating Classical Rarefaction (CR) and Shareholder Quorum Subsampling (SQS) to account for the Signor-Lipps effect.

Once the entire dataset was calibrated, we were able to visualize the diversity of different groups of the fossils (marine, non-marine; fauna and flora etc.) as a function of time (Figs. 12–13). The composite also provided the basis for the subsampling standardization (Fig. 14).

Our results from the quantitative correlation and compositing process revealed the following. The long-term trends in diversity of the marine and continental biotas in the Siberian basins progressively and slowly increased in the Cisuralian, and progressively and slowly declined from the middle Roadian, i.e., P3 global glaciation event (Fielding et al., 2008; Metcalfe et al., 2015; Davydov et al., 2016), towards the end of the Permian. It reached the minimum within the Permian-Triassic transition but remains quite conspicuous, i.e., around 50–60 species in the animals and about 25–30 species of the plants (Figs. 12–13). The most significant turnover in the biota occurs at the base of the Tarakanikha Member, dated to 252.76 Ma in our age model, where flora and fauna drastically change taxonomically and in diversity (Figs. 7–9). Among the animalia, non-marine bivalves that are relatively diverse in the Tailugan Fm nearly disappear in the Maltsev Fm. Only one species of bivalve occurs in the lower Tarakanikha Member and one in the Kedrovsky Member (Fig. 7).

Near the base of the Maltsev Formation a significant reduction occurs in non-marine bivalves and fishes, but their disappearance is explained by the climate shift from humid to arid, as suggested by geochemical and biotic proxies (Figs. 4, 7–13). Taxonomic changes occur among conchostracans and ostracods, but their diversity in the Maltsev Formation remains the same or increased in the latest Changhsingian and early Triassic and did not sharply decline within the transition (Figs. 7–9).

The conchostracs that are quite diverse in the upper Tailugan Fm (11 species) slightly decreased in diversity in the Tarakanikha Member (9 species) at BKS (Fig. 7). The ostracods are among the most abundant fossil groups and commonly occur throughout the Permian-Triassic succession in the Kuznetsk Basin (Andreeva et al., 1956; Kukhtinov et al., 1986; Neustrueva, 1966; Vladimirovich et al., 1967). In the upper Tailugan Fm at the BKS nineteen species are known. Their diversity is slightly greater (21 species) in the Tarakanikha Member (Fig. 7). The ostracods are the most abundant fauna in the rest of the Maltsev Fm in the BKS.

The biotic diversity in Siberia rises to very high numbers during the Early-Middle Triassic with over 400 species of animals and around 150 species of plants by the Middle Triassic (Fig. 13A). The ammonoids and marine bivalves re-occur again within this transition and quickly become the most abundant faunal groups (Dagis and Ustritsky, 1971; Kurushin, 1992; Brayard et al., 2009) (Figs. 12, 13A).

The flora in the BKS demonstrates even more prominent turnover at the base of the Maltsev Formation. All cordaites (sensu lato), a dominant flora in the Permian wetland of Angarida (Meyen, 2002), disappear at this boundary (Fig. 8). The progressive decline of the cordaites (sensu lato) in Angarida is observed since the late Capitanian time and accelerated in Wuchiapingian and Changhsingian time. The last cordaites, *Cordaites minimus* occurs in the very top of the Tailugan Fm (Neiburg, 1936; Radchenko, 1973), no younger than 252.78 ± 0.06 Ma (Figs. 2–4, S4-S6). These eight species of humid-adapted cordaites (sensu *lato*) were replaced by the semi-dry adapted and diverse ferns, lycopsids and sphenopsids and dry adapted gymnosperms, cycades, conifers, ferns, and pteridosperms, (Figs. 8, 11, 12).

The rest of the clades, including sphenopsids, lycopsids, ferns, cycads and pteridosperms increase in diversity especially in the Tarakanikha Member (12 species, including cordaites, in the Tailugan Fm vs 29 species in the Tarakanikha Member). The flora from the Tarakanikha and lower Barsuchi members does not show xerophytic. Cycads, i.e. *Tomia* and *Glossozamites* (Figs. 8, S5 D, F) are usually considered belonging to wet and warm climate (Moisan et al., 2011; Whitelock, 2002), and their occurrence indicates this type of the climate in the BKS. The diversity of the flora in the middle-upper Barsuchi Member (Induan) slightly declined, associated with the maximum aridity of the climate around the Permian-Triassic boundary in the lower Barsuchi Member at this time, as suggested by the geochemical proxies (Figs. 4, 8, S4-S6), but the assemblage is still fairly diverse (11 species). The assemblage there includes pteridosperms *Lepidopteris arctica* (Figs. S4 A, B) and conifers shoots of *Quadrocladus sibirica* (Figs. S4 C-D). In the Kedrovsky and

lower Ryaboy Kamen Member, fern diversity slightly increased and flora there possessed 17 species. Only four species of plants are found in the Ryaboy Kamen Member, but this may be a taphonomic bias linked to the predominance of sandstone and basalts in this part of the section (Fig. 8).

Near the base of the Maltsev Formation a significant reduction occurs in non-marine bivalves and fishes, but their disappearance is explained by the climate shift from humid to arid, as suggested by geochemical and biotic proxies (Figs. 4, 7–9, 11–13). Taxonomic changes occur among conchostracans and ostracods, but their diversity in the Maltsev Formation remains the same or increased in the latest Changhsingian and early Triassic and did not sharply decline within the transition (Figs. 7–9, 11–13).

At the generic level in the *Animalia*, the extinction occurs among some fishes and bivalves. Only a few fish and bivalve genera disappear at the base of the Maltsev Fm, while many new genera of conchostracans and ostracods first appear there (Fig. 9).

Among the plants, eight species of humid-adapted cordaites (sensu *lato*) were replaced by the semi-dry adapted and diverse ferns, lycopsids and sphenopsids and dry adapted gymnosperms, cycades, conifers, ferns, and pteridosperms, (Fig. 8).

The cordaites (sensu lato) do go completely extinct (four genera) at the base of Maltsev Fm. Among the other plants, few genera cross this turnover line and extend up to the top of the section. At the same time 29 new genera appear in the Tarakanikha, Barsuchi and Kedrovsky Members of the Maltsev Fm., i.e., within the Permian to Triassic transition (Fig. 9). There are no clade extinctions at the base of the Maltsev Formation either in *Animalia* or in plants, except the extinction of cordaites among the latter kingdom (Mogucheva and Naugolnykh, 2010). Two orders of fishes and bivalves disappear at the turnover level (Fig. 11). Most of the animal and plant clades and orders in the BKS are sustained across the Tailugan-Maltsev formation boundary and the equivalent of the end-Permian mass extinction boundary as it is designated in South China (Fig. 11) (Shen et al., 2019).

At the generic level, the pattern of the diversity remains the same as the species level, except, the number of the genera is around half that the species (Fig. 13B). In the *Animalia*, the extinction of genera occurs among some fishes and bivalves at the base of the Maltsev Fm, while many new genera of conchostracans and ostracods first appear there (Fig. 9). At the taxonomic order level, the diversity of the taxa remains generally the same throughout the Permian and the number of the orders are slightly increased in the Triassic with no significant decline during the Permian-Triassic transition (Fig. 13C). The diversity of the non-marine fauna and the flora at the species level in Siberia generally remains the same throughout the Permian and slightly increased throughout the Triassic (Fig. 13A). Most of the animal and plant clades and orders in the BKS are sustained across the Tailugan-Maltsev formation boundary and the equivalent of the end-Permian mass extinction boundary as it is designated in South China (Fig. 11) (Shen et al., 2019).

To account for the Signor-Lipps effect we calculate the data with Classical Rarefaction (CR) and Shareholder Quorum Subsampling (SQS) methods. The classical Rarefaction method is often criticized for unnecessary data loss (Gotelli and Chao, 2013; Alroy, 2014), but we decided to add this results because it remains the most commonly used and understood way to standardize samples. At the same time, SQS is the most accurate standardization method with respect to reconstructing the relative magnitude of taxonomic diversity trends (Alroy, 2014; Reddin et al., 2019). The initial data for assessing the diversity of the composite obtained with CONOP were stratigraphical range charts of local sections. We treat such local range chart as a sample for each time intervals. The data on the number of samples for each interval was obtained from the "IncrPlot.txt" file, which is included in the output files of the CONOP software and contains information on the number of ranges in local sections for each level of the composite section and for each taxon. This data was converted to the format accepted by the function's "subsample" from the "DivDyn" R package (Kocsis, Reddin et al., 2019) and executed with the following parameters: number of iterations was 100, the quorum for SQS was 0.4, and the number of occurrences parameter for the CR was 50.

With the obtained curves of standardized diversity, we were able to estimate the influence of the volume of the initial data on the amount of diversity in each of the measured intervals. In addition, these curves show how resistant the obtained taxonomic diversity trends are if the data sample size for each is decreased. The obtained sample-standardized curves show that large volumes of initial data have the maximum effect on the Triassic part of the graph, and less on the Permian part. Nevertheless, the main trends in the variation of diversity persist throughout the entire chart, including part of the Permian-Triassic boundary transition (Fig. 14).

6. Discussion

6.1. The Permian-Triassic boundary in the Kuzbass

The Permian-Triassic boundary in the Kuznetsk Basin has been traditionally placed at the base of Maltsev Formation, above the last coal of the Tailugan Fm in the type-section of the Maltsev Fm along the Tom' River at BKS (Fig. S2-S3). This is the boundary where the most drastic changes in the facies occur and grey, coal-bearing siliciclastics of the Tailugan Formation are replaced by the red-colored volcaniclastic with no coals. The most significant changes in floral communities within the Permian-Triassic transition also occurs at this level (Figs. 8–9) (Vladimirovich et al., 1967; Mogucheva, 1973; Radchenko, 1973; Sadovnikov, 2008).

The lithostratigraphic uncertainty (from 5 to 20 m above the last coal) in the boundary position has been related to definition of the "last" coal in the Tailugan Fm (Radchenko, 1938; Vladimirovich et al., 1967; Radchenko, 1973; Betekhtina et al., 1986; Dobruskina, 1994; Papin and Lezhnin A. I., 1998; Dobruskina and Durante, 2004; Papin and Chunikhin, 2007; Mogucheva, 2016). Thin cm scale coals and/or coal lenses could be missed or not considered and therefore the boundary position slightly varied among geologists. The original base of the formation was defined by the occurrence (First Occurrence Datum, FOD) of prominent Triassic plants such as *Cladophlebis, Tomia, Rhipidopsis, Sphenobaiera* and *Pseudoaraucarites* (Radchenko, 1938; Vladimirovich et al., 1967; Radchenko, 1973; Mogucheva, 2016). The most recent definition of the boundary at the top of the 10 cm coal that occurs 12 m above the midline of Medvezhy (Tarakanikha) Creek (Betekhtina et al., 1986) is now recognized as the official base of the Maltsev Formation in the Kuznetsk Basin (Budnikov, 1996) and this boundary position (at 5.5 mab in BKS, Figs. 11, S3) is accepted in our study.

The base of the Maltsev Fm in the BKS was previously defined by several attributes (features): 1) the sharp change in the lithology with disappearance of the coals (the onset of the coal gap); 2) the occurrence of intermediate to mafic volcanic material in siliciclastics; 3) the extinction of the paleophyte and appearance the mesophyte type flora; 4) a sharp increase in the floral diversity and decreased paleofloristic provincialism in the Early Triassic, as opposed to the less diverse and strongly provincial Late Paleozoic flora; 5) the co-occurrence of the Induan floras and diagnostic conchostracans (Papin and Lezhnin A. I., 1998; Kazakov, 2002; Mogucheva, 2016; Davydov et al., 2019b).

The decrease in paleofloristic differentiation is distinguished by the distribution of early Triassic plant associations known in all paleofloristic provinces. For example, the widely distributed Early Triassic genus *Pleuromeia* has been found in both tropical and temperate (Siberia) climatic zones (Dobruskina, 1994). The taxonomic composition of the Triassic conifer-fern flora testifies to the widest migration of plants to the central regions of Angarida both from the peripheral parts of the Angara kingdom and, apparently, from the tropical belt. Such a migration, obviously, indicates a sharp weakening of floristic differentiation, and elimination of most paleofloristic barriers between different paleofloristic provinces in the Late Paleozoic (Dobruskina and Durante,

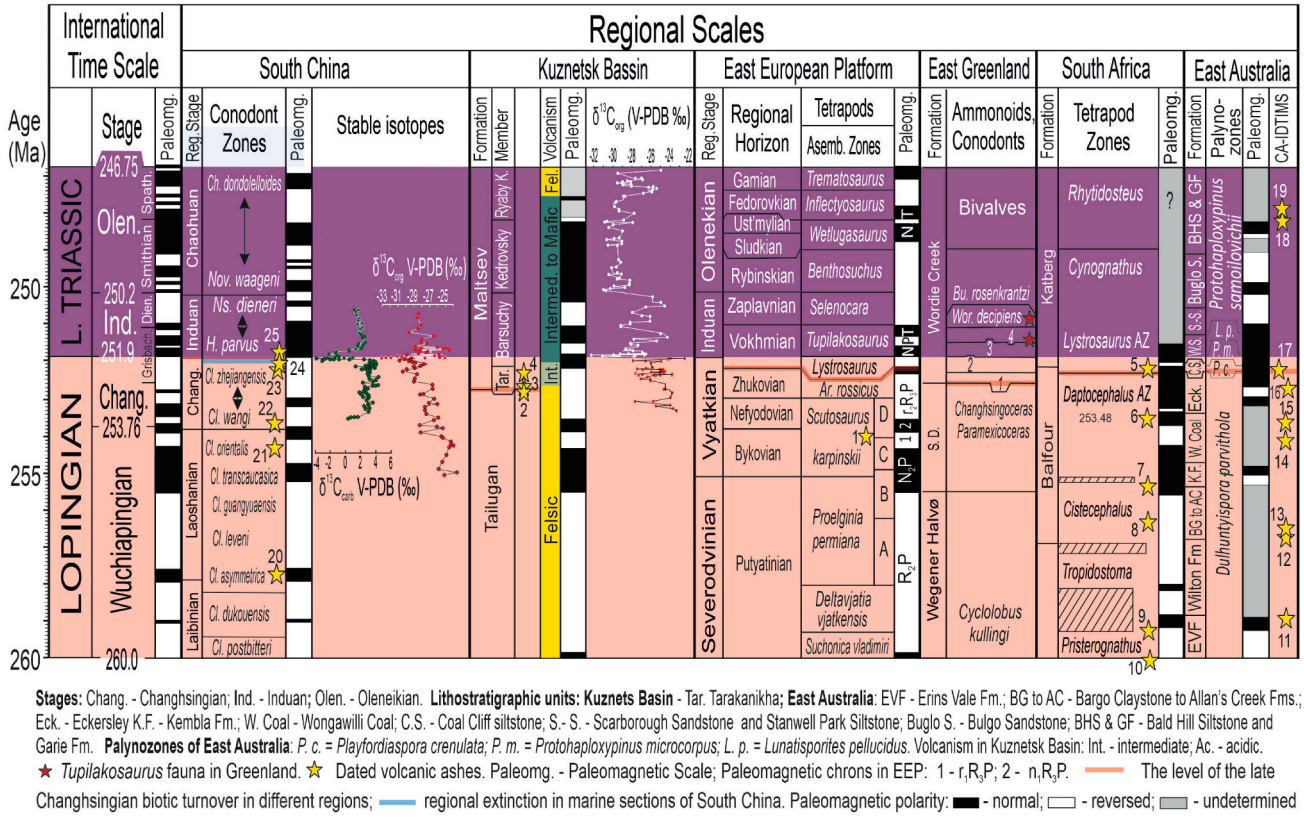

Fig. 6. Correlation chart of the main global sections mentioned in the text. Terrestrial and marine sections now are well correlated via U—Pb radioisotopic ages, paleomagnetic and geochemical ($\delta^{13}C_{org}$) proxies and fauna and flora. The biotic turnover within Permian-Triassic transition (red transparent line) occurs in a mosaic pattern in the different regions. The earliest turnover occurs in Kuznetsk Basin at 252.76 Ma. In the other region's turnover occurs between 252.3 and 252.1 Ma depending upon paleogeography, the regional landscape and land-ocean configuration. The extinction in marine sections in South China occurs 820–350 kyr later that the turnover elsewhere. Assuming the factor is the same in all cases, which, given the lack of synchronicity, is questionable. Faunistic abbreviations. Six Changhsingian *Clarkina* zones in South China (upwards): *Cl. wangi*, *Cl. subcarinata*, *Cl. changxingensis*, *Cl. yini*, *C. meishanensis*, *Cl. zhejiangensis.* Tetrapods: A - *Chronisaurus dongusensis*; B - *Chronisaurus levis*; C - *Jariulinus mirabilis*; B - *Chronisuchus paradoxus*; Ar. – *Archosaurus*. Conodonts: Cl. – *Clarkina*; H. – *Hindeodus*; *Ns.* – *Neospathodus*; *Nov.* – *Novispathodus*; Ch. – *Chiosella*. Biozones in Greenland: 1, *Otoceras concavum - Hypophiceras triviale*; 2, *Otoceras boreale - Metophiceras subdemissum*; 3, *Tompophiceas pascoei - Hindeodus parvus*; 4, *Ophiceras commune*. Dated volcanic ashes (yellow stars): *East European Platform* - 1, 253.95. *Kuzbass* - 2, 252.76; 3, 252.75; 4, 252.33. *South Africa* - 5, 252.24; 6, 253.48; 7, 255.2; 8, 256.25; 9, 259.26; 10, 260.26. *East Australia* - 11, 259.1; 12, 256.77; 13, 256.49; 14, 254.1; 15, 253.59; 16, 252.6; 17, 252.31; 18, 248.23; 19, 247.87. *South China* - 20, 257.79; 21, 254.31; 22, 253.60; 23, 252.36; 24, 251.94; 25, 251.88. Data in *S. China* from Cao et al., 2008, Shen et al., 2011, Yuan et al., 2019, Burgess et al., 2014; in East-European Platform and North Greenland – from Davydov et al., 2020; in South Africa – from Gastaldo et al., 2018, 2020; in Australia – from Belica, 2017, Fielding et al., 2019. Lower Griesbachian according to the data from the type sections in Canadian Arctic (Algeo et al., 2012) and Greenland (Davydov et al., 2020), belongs to Upper Permian. (For interpretation of the references to colour in this figure legend, the reader is referred to the web version of this article.)

2004). The evolution of the Permian-Triassic Angarian flora generally replicates that of Gondwanan flora (Mays et al., 2019). Although the taxonomy of Permian and Triassic floras differs markedly, the foundations of these differences to a greater degree lie in the previous history of the autochthonous development of flora, rather than in climatic contrasts, as was the case in the Late Paleozoic floras (Dobruskina and Durante, 2004).

The Permian-Triassic boundary is defined chronostratigraphically at the base of the bed 27c in Meishan, South China coinciding with the first occurrence of conodont species *Hindeodus parvus* in this section (Yin et al., 2001) and numerically as between an age of 251.94 ± 0.04 Ma for Bed 25 and an age of 251.88 ± 0.03 Ma for Bed 28 of the Meishan section in South China (Burgess et al., 2014). Using the Bayesian age model, we developed in BKS, we can project these key temporal markers into the studied section (Fig. 5). The onset of Siberian Traps LIP extrusive eruptions, as it is designated in the Norilsk and Maymecha-Kotui regions (Burgess and Bowring, 2015), occurs at 33 mab in the BKS, i.e. near the top of the Tarakanikha Member (Fig. 5). The onset of the end-Permian extinction as it is recognized in South China (Burgess et al., 2014; Shen et al., 2019), is projected into the BKS at 44 mab, in the lower Barsuchi Member (Fig. 5). The Permian-Triassic boundary at Meishan in South China (251.90 ± 0.03 Ma; Burgess et al., 2014) correlates in the BKS at 46 mab within the Barsuchi Member (Fig. 5) according to our Bayesian age model conditioned by the three CA-IDTIMS zircon ages (Figs. 5, S2, S3, Table S3). In this part of the section, around the upper dated tuff (sample 16VD8) and especially above it for at least 40 m, the sedimentation pattern is very consistent: accumulation of tuffaceous, fine clastic mudstones and siltstones. Therefore, with a high degree of probability, we consider that the sedimentation rate within this succession was consistent (Figs. 5, S3). The sedimentation within the rest of the Babyi Kamen' section we assumed approximately the same as in the lower Barsuchi Member (Fig. S3). Given the overall high sedimentation rate in the upper Tarakanikha and Barsuchi Members (an average of 35–40 mm per thousand years) and taking into account the statistical uncertainty of the radioisotopic ages, the uncertainty for the Permian-Triassic boundary at BKS is ±220 kyr in terms of absolute time (Figs. 5, S3). This is the most accurate Permian-Triassic boundary ever established in the sedimentary strata of Siberia and adjacent territories. The Induan-Olenekian boundary in the BKS extrapolated with the Bayesian model and sedimentation rates, is proposed to be at 115 mab in

the Babyi Kamen Section (Figs. 7–9, S3), which is consistent with interpretations from flora (Mogucheva and Krugovykh, 2009).

Besides the radioisotopic ages, the boundary position is further substantiated and refined by the major negative shift and excursion in the organic carbon isotope values in the BKS (Figs. 4–5, Table S1). Relatively stable values fluctuating between $\delta^{13}C_{org}$ 24‰ to −28‰ characterize the late Permian Tailugan Formation and lower Tarakanikha Member of the Maltsev Formation (Figs. 4–5). The sharpest changes in isotopic composition of organic carbon occur within the lower Barsuchi Member (42–49.5 mab), where $\delta^{13}C_{org}$ values rise to −22.5‰ and then sharply decrease to −32‰ at 44.5 mab (equivalent to an age of 251.94 Ma in the BKS age model). The $\delta^{13}C_{org}$ partially recover to values of −29‰ to −27‰ by 49.5 mab (251.80 Ma in the BKS age model) but remain low through the interval extending to 60 mab (251.50 Ma in the BKS age model). The $\delta^{13}C_{org}$ recovers to pre-excursion values by 70 mab (251.25 Ma in the BKS age model). These patterns are quantitatively similar to the complex negative carbon isotope excursion occurring before, during and after the extinction interval at the GSSP of the Permian-Triassic Boundary (PTB) and in the Meishan-1 core (Cao et al., 2008; Burgess et al., 2014; Burgess and Bowring, 2015).

Similar carbon isotope excursions around the P-T boundary are recorded in $\delta^{13}C_{carb}$ and $\delta^{13}C_{org}$ in many sections global-wide, but often with less prominent shift and/or with less constrained chronostratigraphic and numeric age precision (Cao et al., 2008; Hermann et al., 2010; Grasby et al., 2013; Metcalfe et al., 2015; Sanson-Barrera et al., 2015; Zhang et al., 2016; Fielding et al., 2019; Shen et al., 2019; Brookfield et al., 2020; Wignall et al., 2020; Wu et al., 2020; Zakharov et al., 2020; Zheng et al., 2020; Zuchuat et al., 2020, in press).

A major $\delta^{13}C_{org}$ excursion has been found at the base of the Triassic in southern Guizhou (Nanpanjiang basin), South China (Bagherpour et al., 2020) associated with the boundary between conodont Unitary association zone 2 (UAZ2) and UAZ 3. This boundary coincides with the base of the extended FAD of *Hindeodus parvus*, i.e., slightly below the official GSSP of the P-T boundary at Meishan (Yin et al., 2001; Brosse et al., 2016). In the temperate climatic zone of the Northern Hemisphere (Canadian Arctic, North Greenland), a similar excursion has been found at the interpreted Permian-Triassic boundary (Zuchuat et al., 2020, in press) or slightly lower (Algeo et al., 2012). The boundary position in both cases is conventional, but evidently the excursion occurs close to or slightly later than the level in BKS.

The Permian-Triassic boundary position in the Kuzbass can be also constrained with paleomagnetic proxies. Our studies (Kuzina et al., 2019a; Kuzina et al., 2019b) and previous data (Kirillov, 1971) suggest the presence of a reversed paleomagnetic zone with small normal polarity subzone in the upper Tailugan and lowermost Tarakanikha Member (Figs. 6, S10). Starting from the Barsuchi Member up to the top of the Maltsev Formation, a normal polarity zone predominates with the many narrow intervals where the polarity is uncertain (Fig. S10). According to the global Permian-Triassic paleomagnetic standard (Hounslow and Balabanov, 2018), the Permian-Triassic boundary in BKS has to occur above the base of Barsuchi Member (above 37 mab).

The Permian-Triassic boundary position in BKS may be also constrained with the magnetic susceptibility (MS) and natural remanent magnetization parameters (NRM). In the Meishan section, South China, and several other sections in different regions of the world, a strong increase in the values of NRM and MS occurs exactly at the Permian-Triassic boundary (Hansen et al., 2000; Peng et al., 2001; Yuan et al., 2003; Algeo et al., 2007; Guo et al., 2008; Lehrmann et al., 2015; Belica, 2017; Xu et al., 2017). In the BKS, the MS and NRM synchronously shift within the Barsuchi Member (45–50 m) towards higher values (Fig. 6). Below 47 m the average MS is $0.32 \cdot 10^{-3}$ SI, and above 50 m in BKS it is $4.27 \cdot 10^{-3}$ SI. In other words, the magnetic susceptibility at the age modeled Permian-Triassic boundary in the BKS increased by more than the order of magnitude (Figs. 6, S10) (Kuzina et al., 2019b).

NRM is less utilized in magnetostratigraphic studies and rarely published in the literature. In the BKS the NRM synchronously changed with the MS (Fig. S10). Below 47 m in Tailugan Fm and Tarakanikha Member of Maltsev Fm in the BKS, the average NRM is $6.6 \cdot 10^{-3}$ A/m and above this level it is over ten times greater, i.e., $81.2 \cdot 10^{-3}$ A/m (Fig. S10). Again, as in case with the MS, the NRM increased at the age modeled Permian-Triassic boundary in the BKS by over ten times.

In summary, the high-precision CA-IDTIMS ages and the derived age model, combined with $\delta^{13}C_{org}$ geochemical proxies and paleomagnetic data provide a continuous chronostratigraphic framework and a firm correlation for the end-Permian extinction interval and Permian-Triassic boundary between 44 and 47 m in the BKS, correlative at *ca* 200 kyr resolution to the PTB established in the Meishan section of South China (Yin et al., 2001; Burgess et al., 2014).

6.2. The record of Siberian Traps magmatism in the Kuzbass

The eruption and emplacement history of the Siberian Traps has been the subject of numerous U—Pb geochronological studies (Reichow et al., 2009; Svensen et al., 2009; Burgess and Bowring, 2015; Burgess et al., 2017), such that a consistent chronostratigraphic framework for eruptions and the extinction has emerged (Burgess et al., 2017). The Siberian Traps magmatism is divided into four intervals: (1) an opening pyroclastic eruption phase; (2) an extrusive lava-producing phase (2/3 of erupted volume) constrained to begin at 252.2 ± 0.1 Ma based upon U—Pb perovskite dating of basal alkaline lavas of the Maymecha-Kotuy area; (3) an intrusive sill emplacement phase starting at 251.91 ± 0.07 Ma; (4) and a renewed extrusive phase from 251.48 ± 0.09 Ma until at least 251.35 ± 0.09 Ma. The model of Burgess et al. (2017) highlights a temporal coincidence of the marine extinction interval with the abrupt change in the emplacement style from extrusive volcanism to intrusive magmatism at 251.91 ± 0.07 Ma, and calls upon this transition as the trigger for mass extinction through "…a massive, short-lived input of greenhouse gasses (e.g., CO_2, CH_4) to the atmosphere, which is thought to have been generated in sufficient quantity either by contact metamorphism of crustal sediments during Siberian Traps LIP magma emplacement, or during LIP plume-related melting at the base of the lithosphere." (Burgess et al., 2017, p. 2).

An outstanding question for this model is the initiation of Siberian Traps LIP (SLIP) magmatism and its environmental consequences, given that the opening stage of pyroclastic volcanism is not constrained by existing geochronology (Kamo et al., 2003; Reichow et al., 2009; Burgess and Bowring, 2015). The Kuzbass was actively accumulating sediments including volcanic detritus in the prelude to the SLIP and end-Permian extinction. Our petrographic and geochemical data document an abrupt appearance and sustained production and deposition of mafic volcanic material in the BKS beginning at 24.6 mab in the Maltsev Fm, which is bracketed between our geochronological samples and can be assigned a precise age of 252.47 ± 0.14 Ma based upon our Bayesian age model (Figs. 3C, S12-16). We adopt this as the best available age estimate of initiation of the opening pyroclastic phase of the Siberian Traps LIP. This estimate is consistent with constraints on the age of eruption of the overlying lavas elsewhere in the Siberian Traps. While this result quantifies extension of the pre-extinction interval record of Siberian Traps LIP volcanism, it also contradicts a correlation between Siberian Traps LIP eruptions (Davydov, 2021 in press) and the older climatic and biotic transitions at the base of the Maltsev Formation dated to 252.78 ± 0.06 Ma.

6.3. Environmental and climate perturbation across the Permian-Triassic transition in the Kuzbass

Two significantly different intervals in terms of sedimentology, geochemistry, biota and environments characterize the Tailugan and Maltsev Formations of the BKS. The coal-bearing Tailugan Formation is reconstructed to record a humid climate with high levels of precipitation, as indicated by the CIA and tNa geochemical indices (Fig. 4, Table S1). The Tailugan Formation is characterized by the highest coal

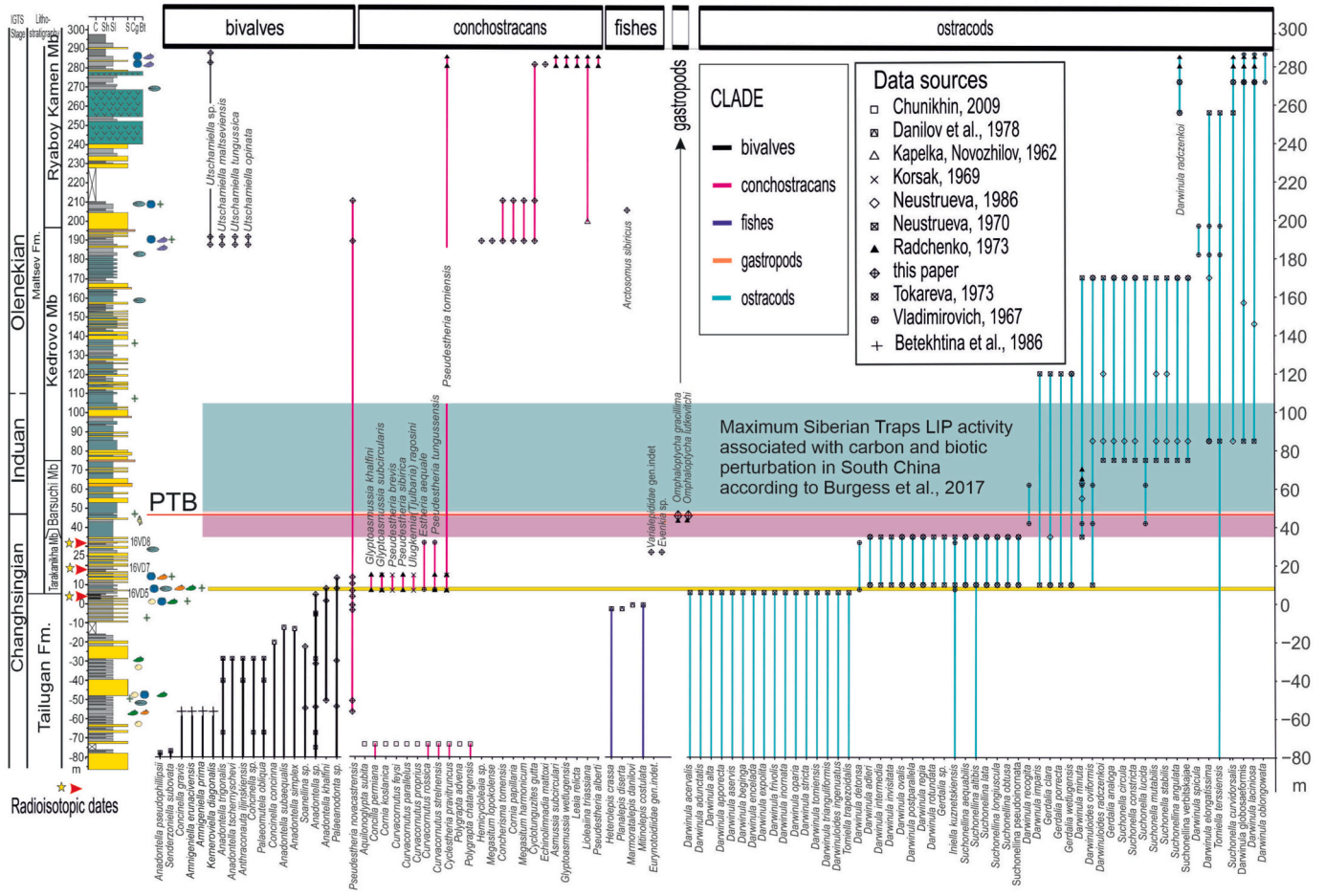

Fig. 7. Faunistic species distribution in Babyi Kamen Section. PTB – Permian-Triassic Boundary. The thick yellow line at 5 m above 0 m of the section (mab) shows the evolutionary turnover in Babyi Kamen Section. Purple highlight – marks the onset of the Siberian Large Igneous Province (SLIP) and greenish highlight – marks the intrusive and sill magmatism in Tunguska Basin according to Burgess and Bowring (2015). The pink line below the PTB is the projection of the onset and cessation of the extinction event as expressed in South China (Shen et al., 2019). For the rest of explanations see Figs. 4–5. (For interpretation of the references to colour in this figure legend, the reader is referred to the web version of this article.)

density in the entire middle-upper Permian succession of the Kuzbass (up to 15–18% of the Tailugan Fm) (Cherepovskiy, 2003). This suggests wetland/swamp dominated ecosystem in an ever-wet climate during most of Changhsingian time (DiMichele, 2014).

The abundant coal-bearing succession in the Tailugan Fm of the Kuznetsk basin was terminated by the climate change towards much drier climate, as suggested by the complete disappearance of coals and by the CIA and τNa geochemical indicators starting at the base of the Maltsev Fm (Fig. 4). Within the Tarakanikha Member of the Maltsev Fm, both geochemical indices suggest the shift towards lower weathering rates and a drier climate (Fig. 4). The peak of extremely dry climate occurs within the lower Barsuchi Member at the level reconstructed via our modeling as the PTB in the BKS. An arid climate continued throughout the entire Induan, changing to intermediate conditions into the Olenekian (Fig. 4).

The biota in the Kuznetsk Basin demonstrates similar patterns in response to climate changes as the geochemical proxies. Regional and local extinction events may often be taxon- or region-specific that can be best exemplified in extinctions by Mesozoic ammonites at various horizons (Oppel, 1853). Such extinctions are important events in the local or regional history of life, however their restricted taxonomic scope, geographic extent, and magnitude of changes, set them apart spatially and temporarily and creating mosaic pattern that is not necessarily tied to the global environmental/ecological factors. Some of these taxon-specific extinction events may also be characterized by high origination rates, thus resulting in high evolutionary turnover with little effect on standing diversity (Flessa et al., 1986).

The difference among Tailugan and Maltsev Fms in the pattern of freshwater bivalves and fishes versus crustaceans (conchostracs and ostracods) can be explained by their ecological preferences. All non-marine bivalves are highly dependent upon oxygen for metabolism and detrital organic matter for nutrition. Hence, they need running water with a high oxygen concentration and organic debris for food. Therefore, bivalves mostly prefer high-energy environments, i.e., rivers, creeks, and other water streams (Betekhtina and Gorelova, 1965; Thorp et al., 2019). The ecological niches of both crustaceans, i.e., ostracods and conchostracs, are nearly the same, and by contrast they prefer low energy environments of swamps, estuaries and temporary ponds and lakes. The bivalves in that environments are usually rare, thin-walled, and small (Papin and Lezhnin, 1998; Karanovic, 2012; Błędzki and Rybak, 2016). In Tailugan wetland time, where freshwater streams were typical in the landscape, the bivalves were common and diverse (Betekhtina, 1974; Betekhtina et al., 1988; Betekhtina, 1990; Silantiev, 2018). They disappear within the transition of the Tailugan and Maltsev Fms and become very rare in the latter formation due to sharp climate shifts from wetland into dry savannah, and the reduction of active water streams and the dominance of small lakes and pond among the water sources.

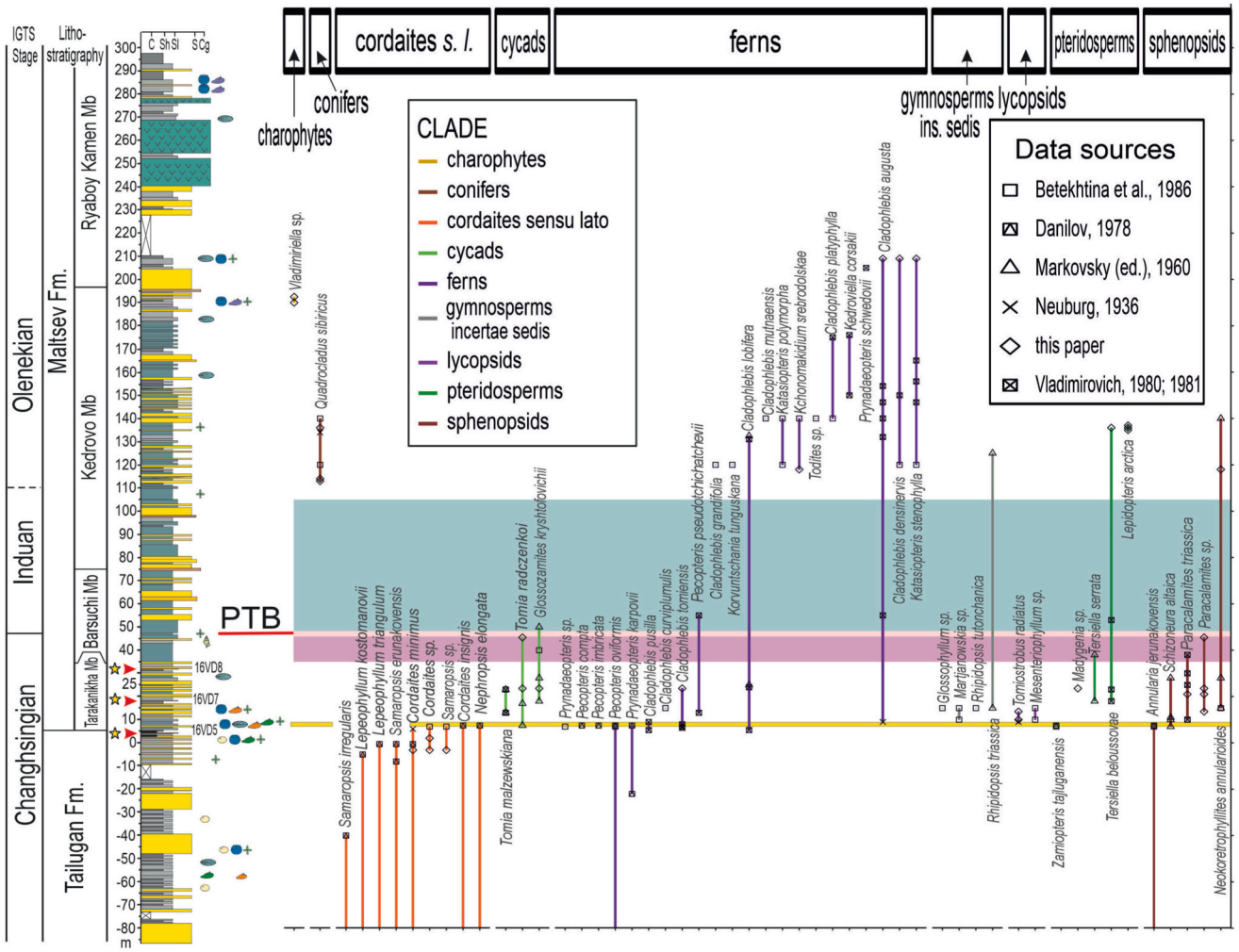

Fig. 8. Floral species distribution in Babyi Kamen Section. The extinction of cordaites (sensu lato) and evolutionary turnover occurs at 5 mab in the section. The species diversity drastically increased at the turnover. For the rest of explanations see Figs. 4–5, 7.

6.4. Biotic diversity across the Permian-Triassic transition of the Kuzbass and elsewhere

The Permian-Triassic biotic event is commonly called the greatest extinction in the Earth history (Newell, 1967; Raup and Sepkoski, 1982; Sepkoski, 2012). The extinction is considered catastrophic, sudden, and very short in time with the duration estimated in marine sections of South China within approximately 35–40 thousand years or even less (Chen and Benton, 2012; Payne and Clapham, 2012; Clapham, 2013; Bond and Wignall, 2014; Burgess et al., 2014; Bond and Grasby, 2017; Burgess et al., 2017; Song et al., 2018; Zhang et al., 2018; Clapham and Renne, 2019; Shen et al., 2019; Racki, 2020). According to this model, the extinction led to a geologically instant disappearance of most of the biotas although the estimates vary from 78% to more than 95% of marine taxa and 75 to 85% in terrestrial biota (Hallam and Wignall, 1997; Sepkoski, 2002; Alroy et al., 2008; Stanley, 2016). However, recent emerging evidence suggests that some faunas and flora began to decrease in diversity before the generally accepted level of extinction in South China (Algeo et al., 2012; Crasquin and Forel, 2014; Schneebeli-Hermann et al., 2015; Kiessling et al., 2018; Song et al., 2018). The recent data from terrestrial successions in North and South China, South Africa, Pakistan and Australia suggest the occurrence of the turnover of the Permian biota to those of Triassic character well before the ALESC, i.e., at least 370 kyrs prior to the designated marine extinction event in *S. China* (Roopnarine and Angielczyk, 2015; Schneebeli-Hermann et al., 2015; Chu et al., 2016; Fielding et al., 2019; Botha-Brink et al., 2020; Feng et al., 2020; Gastaldo et al., 2020).

The end-Permian extinction was one of the earliest that was clearly recognized in the geologic record (Newell, 1962; Raup and Sepkoski, 1982). The mass extinction was distinguished in the fossil record by the abrupt disappearance of most of the taxa, sometimes associated with a discrete transitional “boundary bed” (Logan and Hills, 1973). Some of the authors considered the short duration (i.e., less than 1 million years) as a main feature of the mass extinction (Newell, 1962; Walliser, 1990; Bowring et al., 1998; Bowring et al., 1999; Mundil et al., 2001; Mundil et al., 2004). The application of quantitative biostratigraphic tools on the data from the Permian-Triassic transition narrow the duration of the Permian-Triassic extinction in South China down to <100 kyr (Wardlaw and Davydov, 2005; Wang et al., 2014). This rapidity has been confirmed and robustly quantified with the most recent geochronologic studies in Meishan and other sections in South China (Shen et al., 2011; Burgess et al., 2014; Baresel et al., 2017). Recently, a nearly instantaneous extinction in marine biota in Meishan and Penglaitan sections at the top of a narrow stratigraphic interval limited to 30 ± 31 kyr (or 9 + 29/−19 kyr in different calculation) in South China has been suggested (Shen et al., 2019). In the opinion of the authors of the latter publication, this duration fits with the model of the Siberian Traps volcanism as a killing mechanism (Burgess et al., 2017; Shen et al., 2019).

Mass extinctions in the common sense are defined as “… substantial increase in the amount of extinction (lineage termination) suffered by

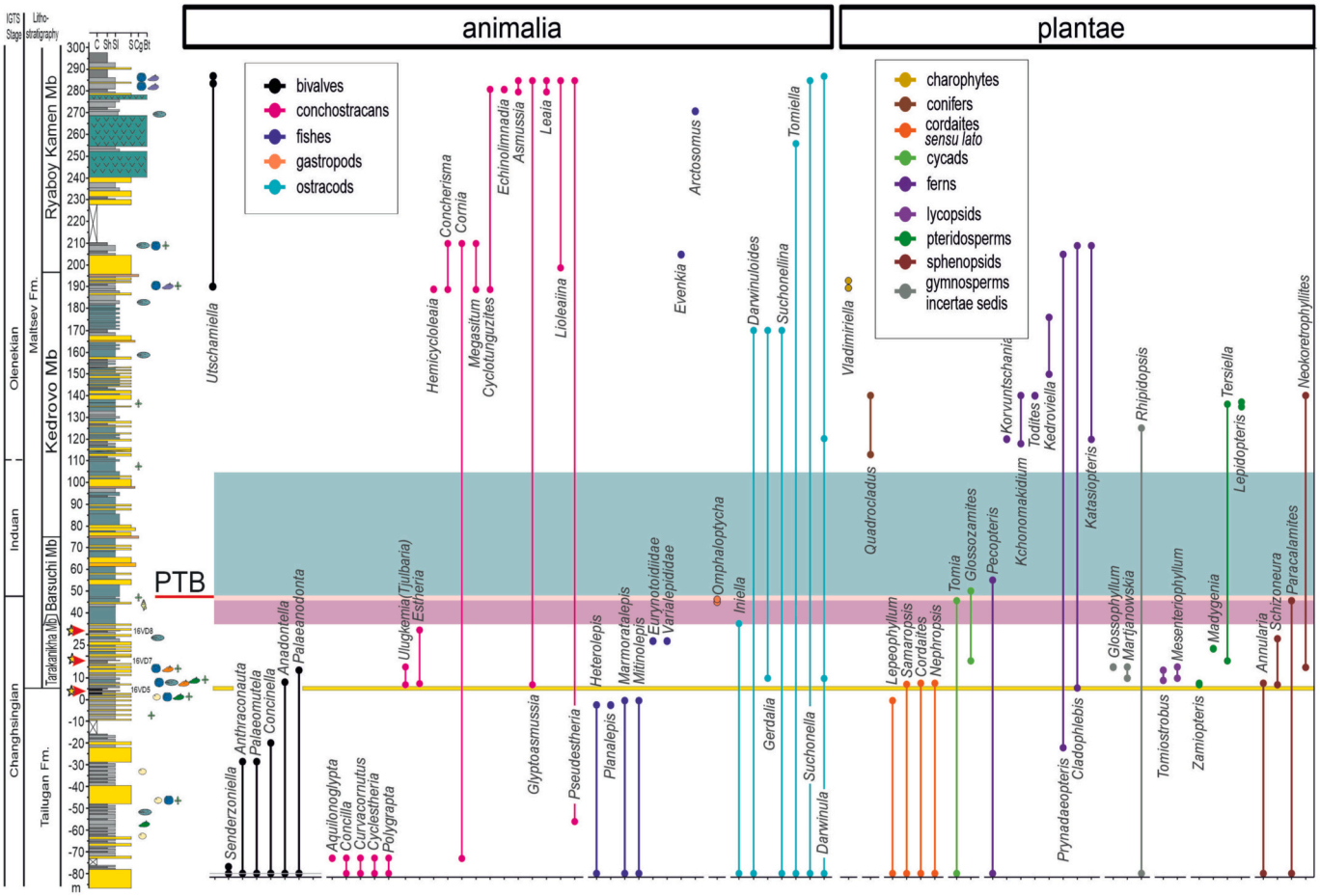

Fig. 9. Floral and faunal distribution of genera in Babyi Kamen Section. Many genera crossing the turnover event in Babyi Kamen event and at the level corresponding to the extinction event in South China. The genera in optimal climatic environments (Tarakanikha and Kedrovo Members) are quite abundant. For the rest of explanations see Figs. 5, 7.

more than one geographically wide-spread higher taxon during a relatively short interval of geologic time, resulting in an at least temporary decline in their standing diversity" (Sepkoski, 1986) p. 278). The more concise description defines a mass extinction as "… an extinction of a significant proportion of the world's biota in a geologically insignificant period of time" (Hallam and Wignall, 1997). Stanley (2016) defines mass extinction qualitatively as an event in which an unusually large percentage of higher taxa in several biological groups died out globally within a brief interval of geologic time. Three major components of the mass extinction can be selected from these definitions: (1) a short duration of extinction event, i.e., around 1 million years or less; (2) a sharp reduction in diversity of most of taxonomic groups within the extinction time interval; (3) elimination of a large percentage of higher taxa (families, orders, classes) in several biological groups at the extinction interval. The above-mentioned traits are not this obvious in the evolution of transitional Permian-Triassic biota in the Kuznetsk Basin, as compared to marine setting in South China (Figs. 7–11).

Within the Permian-Triassic transition in the Kuznetsk Basin, the evolutionary turnover at the base of Maltsev Fm. may be considered as an analogue of the similar diversity decline in South China occurring around 253 Ma (Wang et al., 2014), i.e., 820 kyr earlier than the PTB in Meishan (Shen et al., 2019). An earlier evolutionary turnover in the flora of South China has been proposed by (Xiong and Wang, 2011). A recent floral study in North and South China constrained this turnover to bedsets 23-24b (Chu et al., 2020), around 252.3 Ma (Fig. 6) (Shen et al., 2011; Chu et al., 2016; Yuan et al., 2019).

Although the onset of the Permian-Triassic extinction in South China is considered to occur suddenly at 251.94 Ma (Burgess et al., 2014; Shen et al., 2019) the available data suggest the beginning of the decline of the marine fauna at Meishan and other sections in different regions in China started between 253.0 Ma and 252.0 Ma (Wang et al., 2014; Shen et al., 2019). Several examples from different fossil groups confirm a decline around 252.3 Ma (Feng et al., 2007; Yin et al., 2007; Song et al., 2009; Song et al., 2013; Crasquin and Forel, 2014; Wang et al., 2014). These data document the progressive decline of the diversity in the latest Changhsingian at Meishan, South China (Joachimski et al., 2012), with the acceleration of taxonomic decline towards bed 24e. Similar phenomena are documented in several regions globally, with a high-resolution chronostratigraphic framework (Forel, 2012; Gastaldo et al., 2015; Schneebeli-Hermann et al., 2015; Kiessling et al., 2018; Fielding et al., 2019; Korn et al., 2019; Gastaldo et al., 2020). In other cases, the evolutionary-climatic turnover is well defined in the biotic, sedimentologic and geochemical record, but the precise position of the Permian-Triassic boundary in terms of biotic or numerical calibration is not established, and therefore where the turnover occurs with respect to the International Geologic Time Scale remains undetermined with precision (Smith and Botha-Brink, 2014; Burger et al., 2019; Vajda et al., 2020).

The late Changhsingian turnover among flora and fauna in the Kuznetsk Basin suggest that the factor(s) that enforce the diversity change appear at 252.76 Ma and progressively increased towards the P-T boundary. As noted above, this is about 0.5 Myr earlier than the initiation of SLIP volcanism estimated at 252.24 ± 0.12 Ma (Burgess and Bowring, 2015) or about 0.3 Myr earlier relative to our estimate from

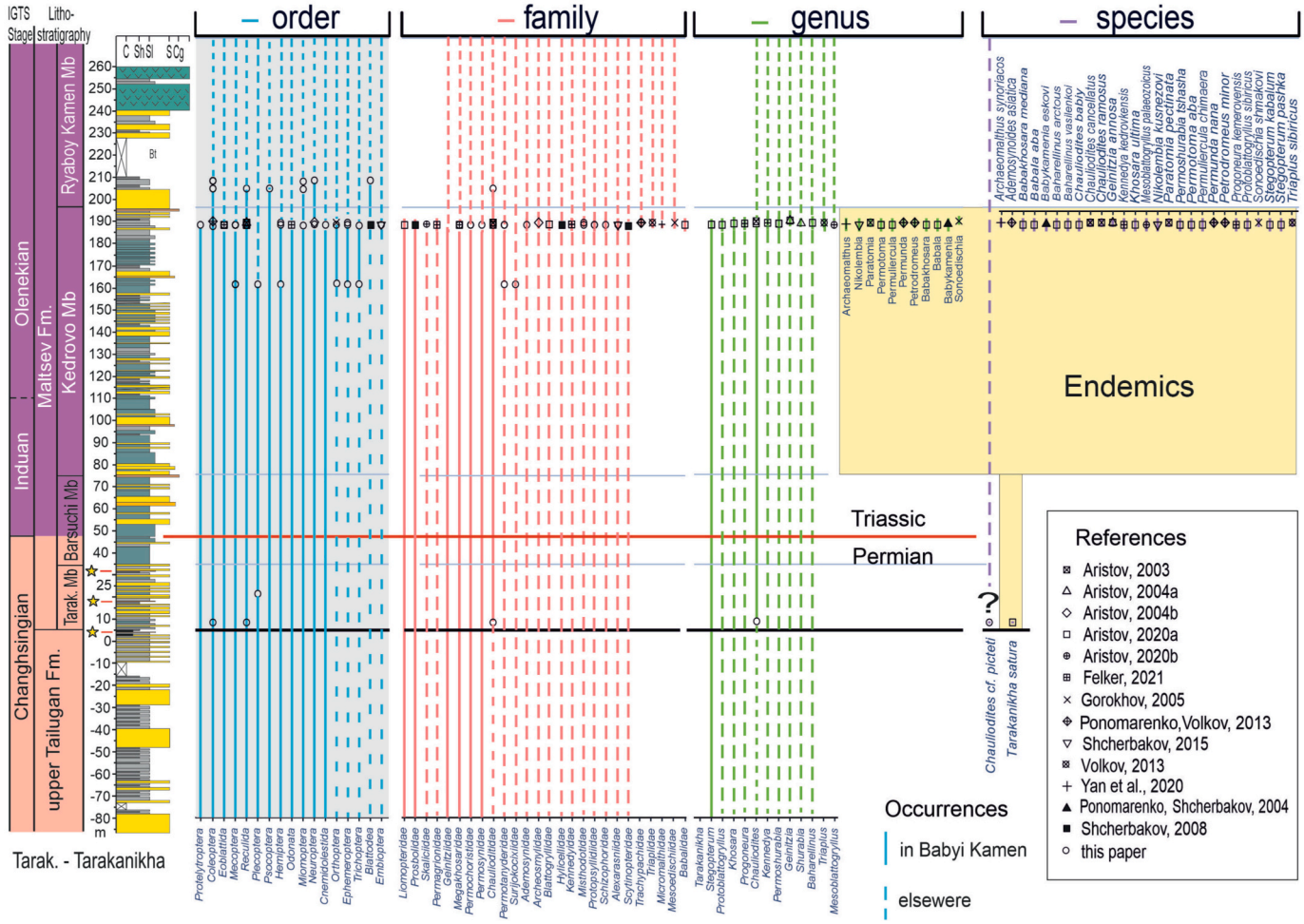

Fig. 10. The distribution of the insects at different taxonomic level (species, genus, family and order) in the Kuznetsk Basin. Sources listed in the box at the lower right corner.

the appearance of abundant mafic volcanic detritus in the BKS at at 252.48 ± 0.12 Ma (Fig. 3). The data from the middle-high latitudes record, including the Kuznetsk Basin, suggest increasing aridification within the latest Changhsingian around 252.76–252.3 Ma in the global continental and marine record (Kerp, 2000; Mogucheva and Naugolnykh, 2010; Algeo et al., 2012; Metcalfe et al., 2015; Schneebeli-Hermann et al., 2015; Chu et al., 2016; Kiessling et al., 2018; Fielding et al., 2019; Feng et al., 2020; Gastaldo et al., 2020; Vajda et al., 2020) (Fig. 6).

In the Kuznetsk Basin the aridification of the environments progressively changed from humid dominated to drier climate beginning near the base of the Maltsev Fm in the BKS at 252.76 Ma (Figs. 4, 6–11), coinciding with the onset of the coal gap in the Kuzbass and surrounding regions (Kazakov, 2002; Mogucheva and Naugolnykh, 2010) (Figs. 7–11, S3). The event also corresponds with the occurrence the intermediate to mafic volcanism in Tunguska, Kuznetsk Alatau and Kazakhstan Basins (Figs. 3, 6). However, this volcanism did not cause the extinction, but rather appears to facilitate the faunal and floral turnover and diversification of the entire biota in the Kuznetsk and Tunguska Basins (our data and Kazakov, 2002; Mogucheva, 2016; Sadovnikov, 2016) (Fig. 12). The input of the volcanism ameliorated the environments for most of the biotic groups (except the bivalves and fishes) and strengthened the diversification of biota in the region. Evidently, the volcanism did not kill the biota in Kuznetsk Basin, that is surrounding the Tunguska Basin, as proposed in many scenarios/models (Kamo et al., 2003; Shen et al., 2011; Bond and Wignall, 2014; Burgess and Bowring, 2015; Chu et al., 2016; Bond and Grasby, 2017; Burgess et al., 2017; Shen et al., 2019). The main force that changed the biota in Kuznetsk Basin was a shift from the cool and humid to warm and dry climate, as registered here with the geochemical and biotic proxies and swamp disappearance (coal gap) that are constrained with the U—Pb ages (Figs. 5–13).

Examining the global record, the onset of the coal gap and the decline of the biota in South China (Wang et al., 2014) occurred in the region around 252.3 Ma. In North and South China and in the low-latitudinal regions of the eastern Tethys, a significant floral composition turnover has been recognized during the late Permian (252.3 Ma) (Kerp, 1996; Xiong and Wang, 2011; Chu et al., 2016; Chu et al., 2020). Similar floral change in western Tethys during the late Permian equatorial lowlands (Kerp, 2000), revealed the appearance of a number of typical Mesozoic plant lineages including cycads, ginkgophytes, *Czekanowskiales* and conifers that gradually became widespread constituents in the succeeding Mesozoic floras worldwide (Kerp, 2000; Krassilov and Karasev, 2009; Blomenkemper et al., 2018; Kustatscher et al., 2019). In Pakistan, the latest Permian flora is characterized by conifers and pteridosperms. At the Permian-Triassic boundary, although the diversity decreases towards the Triassic, gymnosperms and pteridosperms remained the dominant component of the vegetation with no extinction observed within the Permian-Triassic transition (Schneebeli-Hermann et al., 2015).

In South Africa, the newly obtained CA-IDTIMS data suggests the position of the Permian-Triassic boundary slightly above the base of the Katberg Formation within the lower *Lystrosaurus* Assemblage Zone [AZ] (Gastaldo et al., 2020). At the same time, the faunistic and floristic

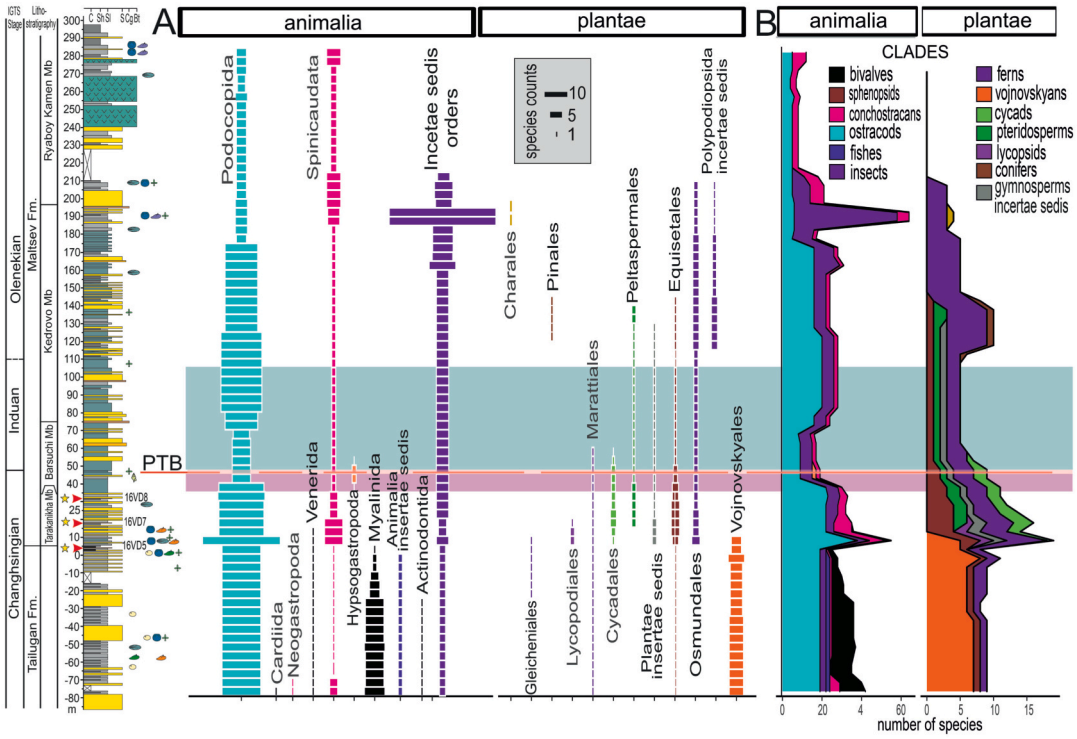

Fig. 11. The orders-level biodiversity of fauna and flora in Babyi Kamen Section. A, all orders distributed throughout late Permian and early Triassic, except cordaites (sensu *lato* =*Vojnovskyales*) in plants. B, species biodiversity in Babyi Kamen Section. The biodiversity among animals generally did not change at the evolutionary turnover, slightly decreased around the Permian-Triassic boundary and become abundant again in the early Triassic. The floral biodiversity in Babyi Kamen Section was relatively low before the turnover, peaked within Tarakanikha, and remains low (7–10 species) within the early Triassic, except in the middle Kedrovo Member. No local extinctions observed in neither faunal nor floral diversity in the entire Maltsev Fm. For the rest of explanations see Figs. 5, 7.

turnover within the Permian-Triassic transition is proposed in the middle of the Palingkloof Mbr of Balfour Fm. between the *Daptocephalus* AZ and *Lystrosaurus* AZ tetrapod faunas and *Glossopteris*-dominated flora to *Dicroidium*-dominated flora (Botha-Brink et al., 2020) or even earlier (Roopnarine and Angielczyk, 2015). This turnover at ~252.3 Ma was essentially synchronous to the turnover in many other regions analyzed here, including the Kuznetsk Basin (Fig. 6).

In the eastern Gondwana (Australia) the beginning of the Permian-Triassic transition (252.31 Ma) coincides with the changes in flora where the previously dominant *Glossopteris* taxa completely disappeared and new and more diverse plants, including lycophytes, voltzialeans, *Lepidopteris* and *Dicroidium* along with numerous new palynotaxa occurred (Fielding et al., 2019; Mays et al., 2019). Unfortunately, no fossils other than plants are documented within the P-T transition in Australia. The authors of the aforementioned publications considered this transition as the terrestrial biotic collapse and extinction, although this is a definite evolutionary turnover in the plants, like the one we documented in Kuznetsk Basin. A relatively sharp and synchronous biotic turnover at the global scale in middle-high latitudes in northern Pangea (Canadian Arctic, Greenland, Kuznetsk Basin), North and South China and Gondwana (Australia, South Africa, Pakistan) suggests a progressive global warming event similar to what is documented in the marine record (Algeo et al., 2012; Joachimski et al., 2012; Penn et al., 2018; Joachimski et al., 2020). The onset of the climate warming, in the marine records in South China and Transcaucasia, occurs around 252.1 Ma (bed 22 at Meishan in *S. China* and *Clarkina bachmani* conodont zone in Ali-Bashi, Iran) (Joachimski et al., 2012; Joachimski et al., 2020). This record has been documented in the tropics (25–30 ° S) where the climatic warming is not as significant as in middle-high latitudes (Burrows et al., 2011).

Several important groups of fauna and flora immigrated to the middle-high latitudes at this transitional time. The return of ammonoids (*Otoceras*) and the conodonts (*Hindeodus* and *Clarkina*) in the late Changhsingian (Zakharov et al., 2020) indicate climate warming and appropriate environmental temperatures for these climatically sensitive faunas after a long cool to cold climate time (middle Roadian – Changhsingian) (Joachimski et al., 2012; Davydov and Biakov, 2015; Davydov et al., 2016; Davydov et al., 2018; Joachimski et al., 2020). A similar reappearance of ammonoids and conodonts within the Permian-Triassic transition is documented in the Canadian Arctic and Greenland (Bjerager et al., 2006; Algeo et al., 2012; Davydov et al., 2020). The only Permian tetrapods in Siberia are found in the latest Changhsingian-earliest Triassic transition of the Tunguska Basin (Korvunchana biota) (Efremov and V'yushkov, 1955; Skundin, 1974), which is again consistent with climate warming close to the base of the Maltsev Formation of the Kuznetsk Basin. Several important Mesozoic groups of flora (gymnosperms *incertae sedis*, pteridosperms, pleuromeiales, lycopsids [including pleuromeiales] and conifers) also first appear in this transition in Siberia (Fig. 12).

6.5. *Reconciling global patterns of terrestrial turnover and marine extinction in the tropics across the Permian-Triassic transition, and modern analogs*

The pattern of biological diversity in the Phanerozoic was recognized at first from the data mostly collected in the paleo-tropics-subtropics (Fig. 15D) (Newell, 1967; Raup and Sepkoski, 1982; Sepkoski, 2002). The number of fossil collections for middle-high latitudes was and still is insufficiently smaller (about 10–15% of entire P-T collections in PaleoDB project) (Fig. 15D) (Close et al., 2020), and the latter have never been adequately assessed. Many fossil groups in the tropics-subtropics that were dominant in the Paleozoic completely disappeared close to the P-T boundary. These groups include tabulate and rugose corals, fenestrate bryozoans, goniatite cephalopods, blastoid echinoderms,

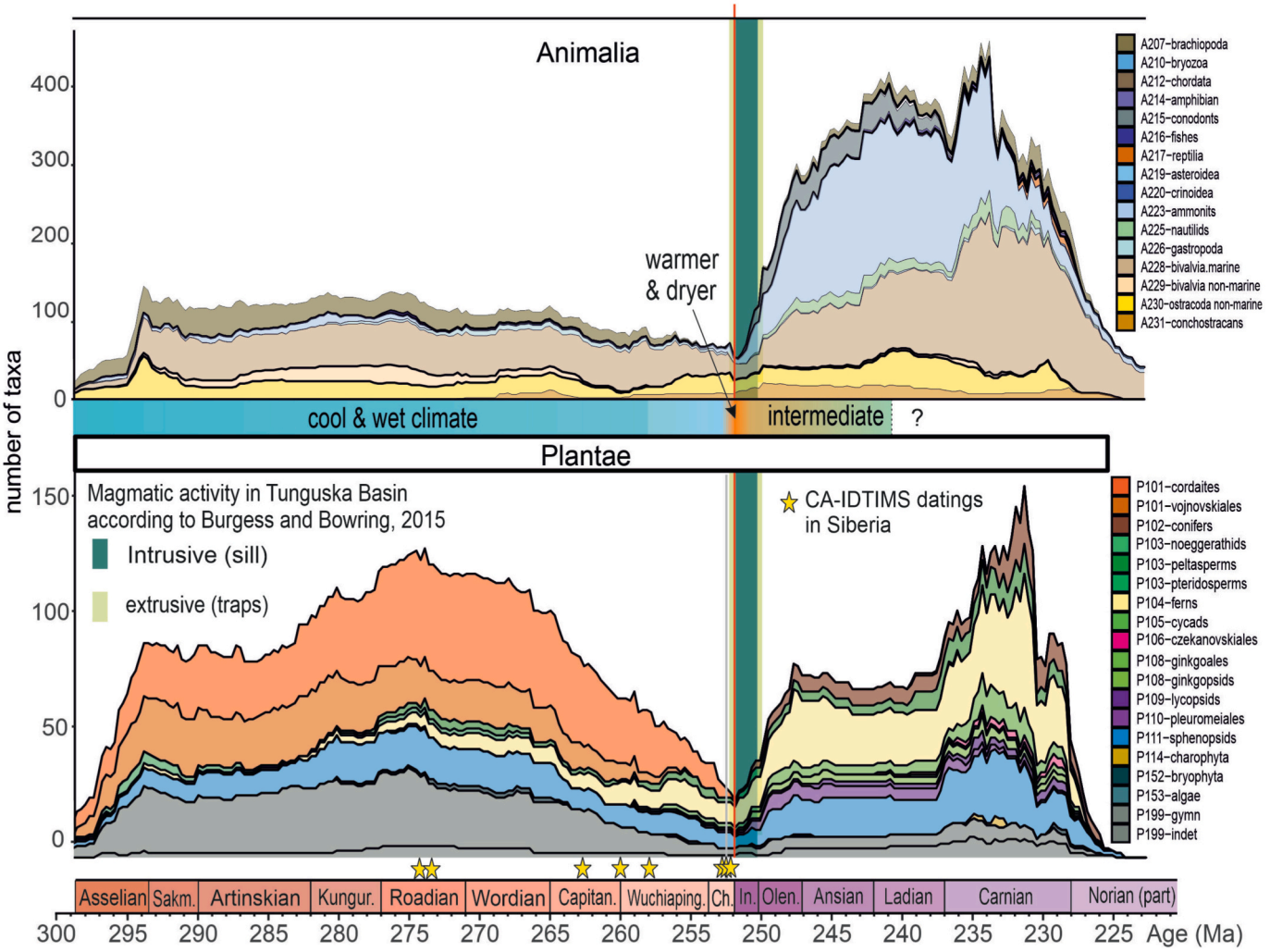

Fig. 12. The species biodiversity of the animals and plants in the marine and continental subsections of Siberia (Kuznetsk Basin, Tunguska Basin, Verkhoyanie, Taymyr, periphery of Okhotsk Massif, Omolon Massif). Yellow stars indicate CA-IDTIMS ages obtained in Siberia (Davydov et al., 2016; Davydov et al., 2018). Red line – the Permian-Triassic boundary, the straight vertical green line – intrusive sills activity in Tunguska Basin according to Burgess and Bowring (2015). The intrusive activity does not affect on the evolution of the biota in Siberia. (For interpretation of the references to colour in this figure legend, the reader is referred to the web version of this article.)

trilobites, rostroconch mollusks, multiplacophoran stem-group chitons, hyoliths, all strophomenate brachiopods, including the productids, the orthids and spiriferids from the Rhynchonellata and many others (Payne and Clapham, 2012). A physiological control on extinction has been proposed, namely a selection against genera with poorly buffered respiratory and calcareous shells (Clapham and Payne, 2011). Most of these fossils are generally distributed within the tropics-subtropics, where increases in marine temperatures and reduced oxygen availability were responsible for most of the extinctions (Penn et al., 2018; Joachimski et al., 2020).

The factor causing the extinction could be an extremely high temperature itself in the tropics-subtropics, which has some support in modeling of global warming and recent modern ecological dynamic. The average global near surface temperature from the year 1880 to recent has changed by 0.8–1.2 ˚ C (Fig. 15A, B) (Lenssen et al., 2019), whereas the warming in the middle-high latitudes is nearly twice of that, i.e., up to 2–4 ˚ C (Fig. 15B, red line) (Susskind et al., 2019). Generally, the same model of higher climate sensitivity in the middle-high latitudes has been proposed for the Permian-Triassic transition time (Fig. 1, insert) (Penn et al., 2018), where the temperature change in the tropics was about half that in the middle-high latitudes (Fig. 1, insert). The conodont phosphate paleothermometer possesses an uncertainty up to 2 ˚ C (Chen et al., 2013 and Prof. Michael Joachimski personal communication). This means that the onset of the warming of the global climate by 1.5–2 ˚ C in the tropics might not be detected by this method, but the temperature at the middle-high latitudes might be increased up to 4 ˚ C and cause deforestation and turnover in high-middle latitudes earlier than in tropics, with a unimodal Latitudinal Diversity Gradient (LDG) (Figs. 1, insert and 15B, blue line). This type of LDG in the recent planktonic foraminifera was characteristic for the last ice age and developed into a bimodal gradient through species distribution shifts driven by post-glacial recent ocean warming (Yasuhara et al., 2020). Model projections suggest that future warming will further diminish tropical pelagic diversity to a level not seen in past millions of years (Yasuhara et al., 2020). A global study of extinction risk in vascular plants finds that species in the tropics appear to have a greater natural susceptibility to extinction and disproportionately higher extinction risk in this climatic belt, even when indicators of human pressure (gross domestic agricultural product, population density, forest cover change) are considered (Vamosi and Vamosi, 2008). The recent local extinctions in both marine and terrestrial biotas are significantly higher in tropical species than in temperate species (55% versus 39%), in animals than in plants (50% versus 39%), and in freshwater habitats relative to terrestrial and marine habitats (74% versus 46% versus 51%) (Wiens, 2016). Besides, the

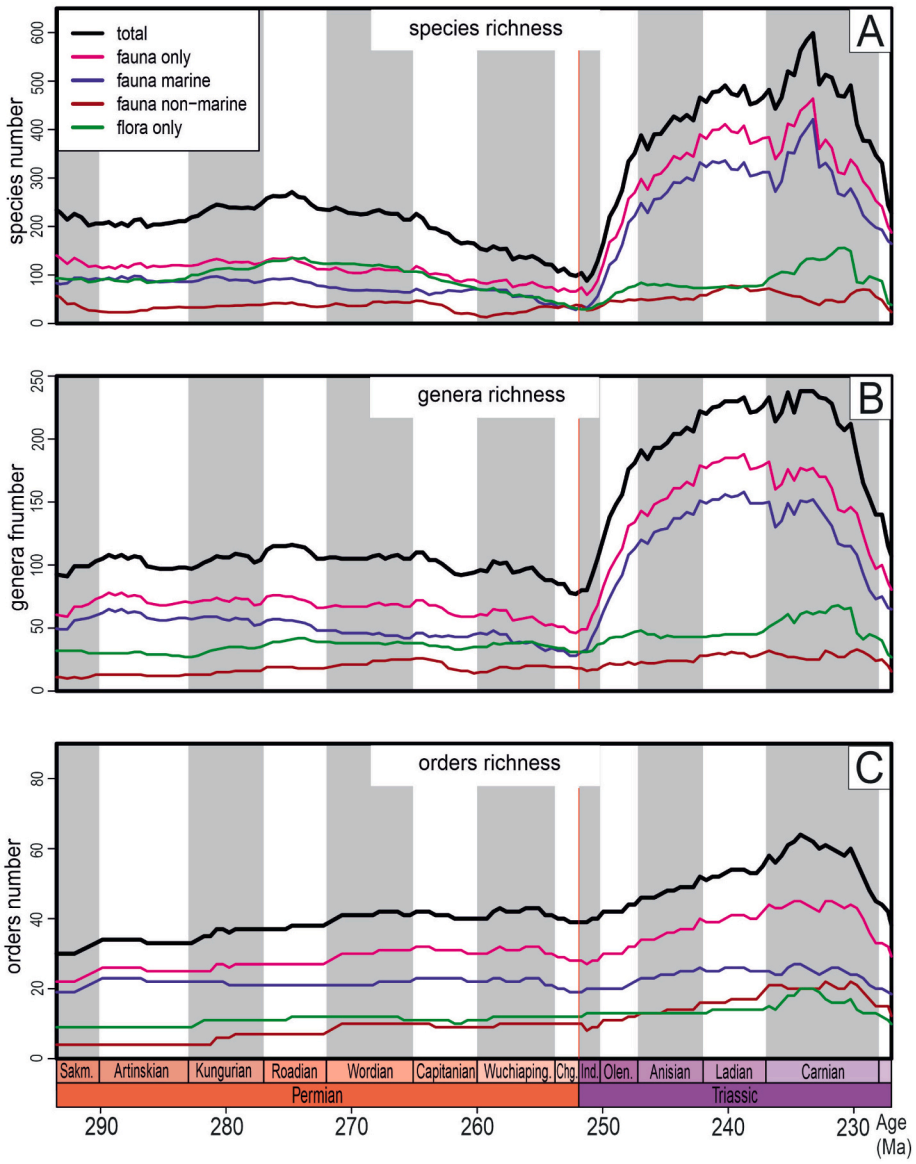

Fig. 13. The diversity of the faunas and flora at the different taxonomic levels (species, genera and orders) in Siberia. There is no sharp and sudden extinction in this middle latitudinal temperate climate zone within the Permian-Triassic transition, but rather the progressive decline from middle Roadian (P3 global glacial event) though the Permian-Triassic evolutionary turnover in Kuzbass (252.76 Ma). From latest Permian chronostratigraphic level throughout the Triassic the diversity in both fauna and flora and in terrestrial and marine faunas rapidly increased. The diversity increase is recognized at any taxonomic level, although it is more prominent at the species and generic level and less significant at the order level. Stage's abbreviations: Sakm. – Sakmarian; Chg. – Changhsingian; Wuchiaping. – Wuchiapingian; Ind. – Induan; Olen. - Olenekian.

extinction of the biotas is shifting along temperature isotherms north and south poleward (Fig. 15B, C). However, terrestrial species are lagging behind shifting isotherms more than marine species, which is probably related to the interplay between the wider thermal safety margin of terrestrial versus marine species and the more constrained physical environment for dispersal in terrestrial versus marine habitats (Wiens, 2016; Lenoir et al., 2020). In terrestrial habitats the prime driver of diversity dynamics is an environmentally driven extinction (analogous to the late Permian cordaites collapse), with high origination being an opportunistic response to diminishing ecospace occupancy (Lehtonen et al., 2017).

The migration of the biota along with climate velocity shifts is also confirmed in a marine taxa study (Molinos et al., 2016) that suggests that in the recent warming climatic trend, the range of expansions prevail over contractions in representative concentration pathways up to year 2100 (Fig. 15B, C). This is producing a net local increase in richness globally, and temporal changes in composition driven by the latitudinal redistribution, rather than the loss of diversity. At the same time, widespread invasions homogenize present-day communities across multiple regions. High extinction rates are expected regionally within the tropics-subtropics, leading to strong decreases in richness there (Fig. 15C) (Molinos et al., 2016). Mid-latitude regions with semi-arid and strongly seasonal climates (especially Mediterranean-climate areas) had much higher endemic species richness than predicted by the model (Cowling and Samways, 1994).

All these data suggest that the global climatic warming effects the tropical biotas much stronger than those in middle-high latitudes and the latter are more resistant to warm temperatures (Molinos et al., 2016; Wiens, 2016; Pinsky et al., 2019). This resistance of the biotas in marine habitats during the climate warming events in the middle-high latitudes is supported by the much higher oxygen level in the latest Permian, whereas in tropical and subtropical the oxygen was deadly low and caused the extinction alone with the other stress factors (Penn et al., 2018).

Thus, the Permian-Triassic extinction mostly occurs in the tropics and subtropics due to the strong climatic warming, most probably relatively slow and moderate in the late Changhsingian and gradually but quickly extended in the latest Changhsingian to the abnormally high temperature and extremely low oxygenated water that was deadly for most marine animals, except the planktonic one which were less effected (Radiolaria) (de Wever et al., 2006). The warm climate shift poleward during the Permian-Triassic transition in the middle-high latitudes,

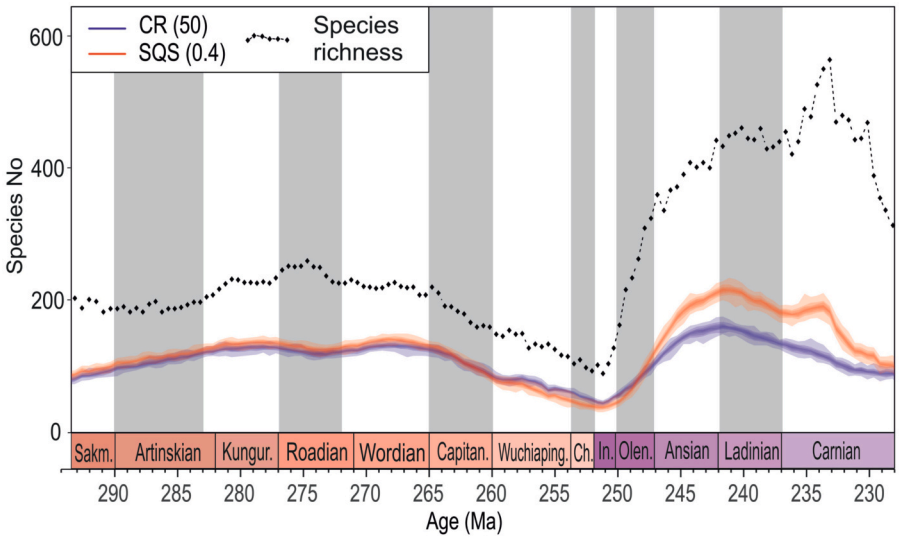

Sakm. -- Sakmarian; Capitan. – Capitanian; Wuchiaping. – Wuchiapingian; Ch. – Changhsingian; In. – Induan; Olen. – Olenekian

Fig. 14. Raw richness and subsampling standardization of the Permian-Triassic composite of Siberia. The dashed line shows a raw species richness (black line with points); colored lines - species richness standardized with Shareholder Quorum Subsampling (SQS, red line) and Classical Rarefaction (CR, blue line). The parameters of the subsampling: length of bin intervals near 0.5 MA, trials - 100, the quorum for SQS - 0.4, number of occurrences parameter for the CR - 50. The plot is created using functions from the "DivDyn" R package (Kocsis, Reddin et al., 2019). (For interpretation of the references to colour in this figure legend, the reader is referred to the web version of this article.)

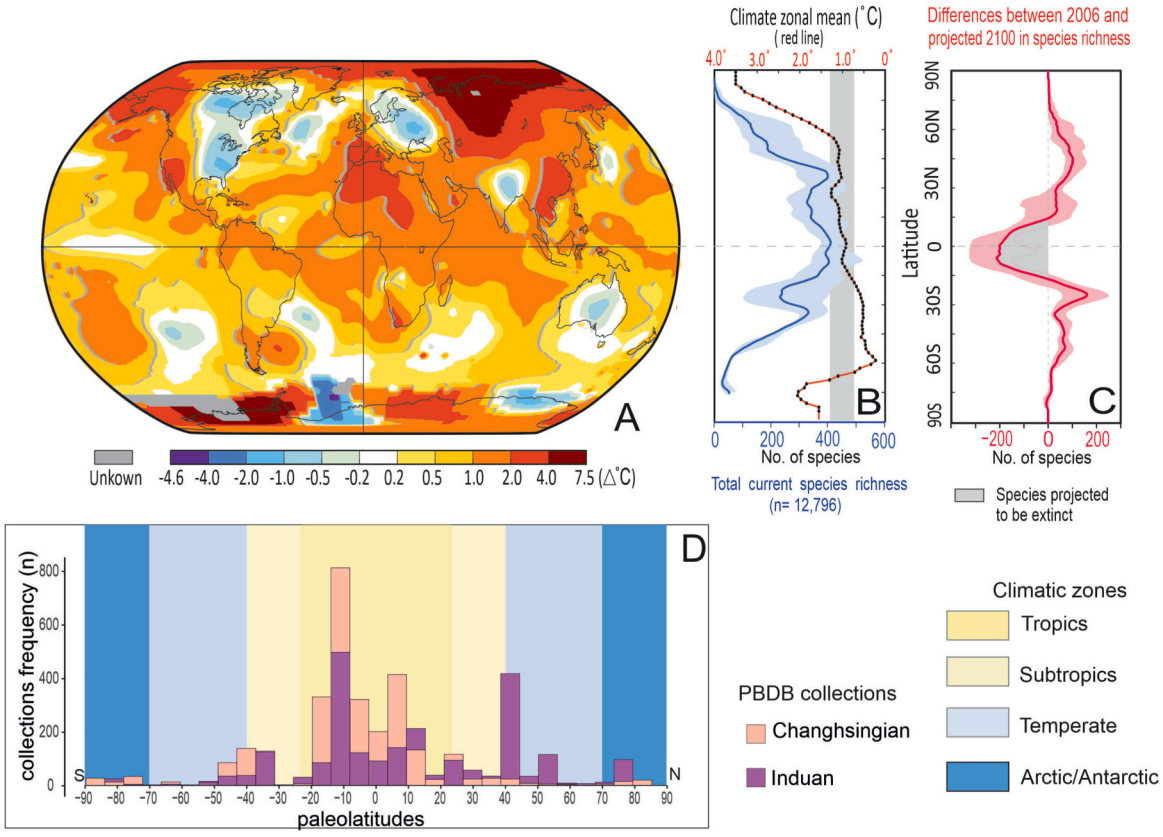

Fig. 15. Distribution of global surface temperature and biodiversity patterns under recent and future climate change. (A) Recent Land-Ocean surface Temperature index anomaly (C) versus 1951–1980 temperature distribution https://data.giss.nasa.gov/gistemp/maps/index_v4.html; (B) the initial bimodal temperature redistribution (red line with black dots) has just begun. Grey vertical thick line shows the global average mean temperature change from 1880 to recent (Lenssen et al., 2019). The current global marine species richness (n = 12,796, blue line and numbers) also demonstrates the occurrence of the initial bimodal distribution in biotic richness as well (Molinos et al., 2016); (C) the difference between recent (2006) and projected by 2100 latitudinal species richness (Molinos et al., 2016). The highest amount of biota extinctions (up to 60–70%) projected to occur within the tropics (approximately 0–15 N and S). The species richness in the subtropics and mid-latitudes (15–65 N and S) demonstrate a significant increase. The diversity in high-latitudes (70–90 N and S) remains unchanged; (D) Changhsingian and Induan fossil's collections in PaleoBiology Database (PBDB) as of July 2020 (collected from the site https://paleobiodb.org/navigator/). Most of the data from Permian-Triassic successions are from the tropics-subtropics. (For interpretation of the references to colour in this figure legend, the reader is referred to the web version of this article.)

caused the replacement (turnover) in terrestrial settings of the humid-related biotas by the dry climate-related and more diverse communities that diversified throughout the Triassic in both marine and terrestrial habitats. One recent model of the extinction pattern during the Permian-Triassic transition (Penn et al., 2018), however, suggests the opposite picture, where the main extinction event occurs in middle-high latitudes and medium extinction in tropics-subtropics. This model contradicts our data reported in this paper, and with the patterns of the recent biota global response to the dynamic climate warming during the last century, and predicted response in 21st century in marine and terrestrial habitats along the latitudinal gradient (Vamosi and Vamosi, 2008; Burrows et al., 2011; Molinos et al., 2016; Wiens, 2016; Pinsky et al., 2019; Lenoir et al., 2020; Yasuhara et al., 2020). The pattern of the Permian-Triassic event was more intricate in terms of extinction, turnover, and diversity of biota within the different climatic zones and environmental habitats than has been generally thought.

7. Conclusions

1. The Permian-Triassic boundary has been for the first time precisely established in the sedimentary successions of Siberia, in the Babyi Kamen section of the Kuznetsk Basin, through CA-IDTIMS U-Pb zircon ages, organic carbon isotope, geochemical, and paleomagnetic proxies.
2. The local extinction of the humid-dominated forest flora (cordaites) and the dry climate biota evolutionary turnover in the Kuznetsk Basin occur 820 kyr earlier than the end-Permian extinction event recorded in South China at 251.94 Ma.
3. There is a minor extinction at 252.76–252.75 Ma at the species and genera level, but not at the order taxonomic level in the Kuznetsk Basin and in the entire Siberia. The biota in Kuznets Basin subsequently diversified (with some exceptions) across the Permian-Triassic transition.
4. The marine and terrestrial biota diversity in Siberia progressively increased from the beginning of the Permian up to the middle Roadian (early Guadalupian global glacial event). Since that time, the diversity at species and generic level progressively and slowly declined towards the latest Changhsingian (252.76 Ma). Starting from this time, the biota rapidly diversifies in the latest Changhsingian and Early-Middle Triassic.
5. The Permian-Triassic extinction mostly occurs in the tropics and subtropics due to the strong climatic warming, that was relatively low in late Changhsingian and gradually but quickly extends in the latest Changhsingian to the abnormally high temperature and extremely low oxygenated water that was deadly for most marine animals.
6. The warm climate shift poleward during Permian-Triassic transition in the middle-high latitudes caused the replacement (turnover) of the humid-related biotas by the dry climate-related and more diverse communities expanded throughout the Triassic in both marine and terrestrial habitats.
7. The pattern of the Permian-Triassic event was more intricate in terms of extinction, turnover, and diversity of biota within the different climatic zones and environmental habitats than has been generally considered.

Declaration of Competing Interest

The authors declare that they have no known competing financial interests or personal relationships that could have appeared to influence the work reported in this paper.

Supplementary data to this article can be found online at https://doi.org/10.1016/j.palaeo.2021.110432.

Acknowledgments

This work was supported by the Russian Scientific Foundation, project no. 19-17-00178 and by RSF project No. 21-14-00284 (for VDV). We thank Prof. Joachimski, GeoZentrum Nordbayern, Universität Erlangen-Nürnberg, Germany, for the consultation regarding conodont phosphate paleothermometer uncertainty. The great advice from Prof. Peter Sadler, Riverside University, CA, USA with CONOP technique was very helpful. Mr. Alexander Bakaev, a PhD student from Paleontological Institute in Moscow of Russian Academy of Sciences thanks for the fish remains identifications. The help of Dr. Anna M. Fetisova from Moscow State University (MGU) with the paleomagnetic data interpretations is highly appreciated. The libraries at Boise State University and Florida International University provided access to literature sources. The input from two anonymous reviewers and Chief-Editor of the PPP, greatly improved the manuscript.

References

Abatzoglou, J.T., Dobrowski, S.Z., Parks, S.A., 2020. Multivariate climate departures have outpaced univariate changes across global lands. Sci. Rep. 10 (1), 3891.

Algeo, T.J., Ellwood, B., Nguyen, T.K.T., Rowe, H., Maynard, J.B., 2007. The Permian–Triassic boundary at Nhi Tao, Vietnam: evidence for recurrent influx of sulfidic watermasses to a shallow-marine carbonate platform. Palaeogeogr. Palaeocimatol. Palaeogeogr. 252 (1–2), 304–327.

Algeo, T.J., Kuwahara, K., Sano, H., Bates, S., Lyons, T., Elswick, E., Hinnov, L., Ellwood, B., Moser, J., Maynard, J.B., 2011. Spatial variation in sediment fluxes, redox conditions, and productivity in the Permian–Triassic Panthalassic Ocean. Palaeogeogr. Palaeocimatol. Palaeogeogr. 308 (1), 65–83.

Algeo, T., Henderson, C.M., Ellwood, B., Rowe, H., Elswick, E., Bates, S., Lyons, T., Hower, J.C., Smith, C., Maynard, B., Hays, L.E., Summons, R.E., Fulton, J., Freeman, K.H., 2012. Evidence for a diachronous Late Permian marine crisis from the Canadian Arctic region. Bull. Geol. Soc. Am. 124 (9–10), 1424–1448.

Allen, C.M., Campbell, I.H., 2012. Identification and elimination of a matrix-induced systematic error in LA–ICP–MS 206Pb/238U dating of zircon. Chemical Geology 332-333, 157–165.

Alroy, J., 2014. Accurate and precise estimates of origination and extinction rates. Paleobiology 40 (3), 374–397.

Alroy, J., Aberhan, M., Bottjer, D.J., Foote, M., Fürsich, F.T., Harries, P.J., Hendy, A.J.W., Holland, S.M., Ivany, L.C., Kiessling, W., Kosnik, M.A., Marshall, C.R., McGowan, A. J., Miller, A.I., Olszewski, T.D., Patzkowsky, M.E., Peters, S.E., Villier, L., Wagner, P. J., Bonuso, N., Borkow, P.S., Brenneis, B., Clapham, M.E., Fall, L.M., Ferguson, C.A., Hanson, V.L., Krug, A.Z., Layou, K.M., Leckey, E.H., Nürnberg, S., Powers, C.M., Sessa, J.A., Simpson, C., Tomasovych, A., Visaggi, C.C., 2008. Phanerozoic trends in the global diversity of marine invertebrates. Science (New York, N.Y.) 321 (5885), 97–100.

Andreeva, E.M., Mandelshtam, M.O., Radchenko, G.P., Rotay, A.P., Khalfin, L.L., Yavorsky, V.I., 1956. Atlas of the Key-Fossils of Fauna and Flora from Permian of Kuznets Basin. Gosnauchtekhizdat, Leningrad (In Russian).

Aristov, D.S., 2020. New Gryllones Insects (Insecta: Gryllones) from the Babii Kamen' Locality (Upper Permian of Russia). 2. Order Reculida and Gryllones Ordinis Incertis. Paleontol. J. 54 (2), 132–142.

Aristov, D.S., Bashkuev, A.S., Golubev, V.K., Gorochov, A.V., Karasev, E.V., Kopylov, D. S., Ponomarenko, A.G., Rasnitsyn, A.P., Rasnitsyn, D.A., Sinitshenkova, N.D., Sukatsheva, I.D., Vassilenko, D.V., 2013. Fossil insects of the middle and upper Permian of European Russia. Paleontol. J. 47 (7), 641–832.

Babin, G. A. (ed.), 2007. State geologic map of Russian Federation. Scale 1:1 M (third generation). Altai-Sayany Series, Sheet N-45-Novokuznetsk. Explanatory notes. Cartographic factory of VSEGEI, 665 p. (In Russian), St. Petersburg.

Bagherpour, B., Bucher, H., Vennemann, T., Schneebeli-Hermann, E., Yuan, D.-X., Leu, M., Zhang, C., Shen, S., 2020. Are Late Permian carbon isotope excursions of local or of global significance? Bull. Geol. Soc. Am. 132 (3–4), 521–544.

Baresel, B., Bucher, H., Bagherpour, B., Brosse, M., Guodun, K., Schaltegger, U., 2017. Timing of global regression and microbial bloom linked with the Permian-Triassic boundary mass extinction: implications for driving mechanisms. Sci. Rep. 7, 43630.

Baumgardner, R.W., Hamlin, H.S., Rowe, H.D., 2014. High-resolution core studies of Wolfcamp/Leonard basinal facies, Southern Midland Basin, Texas. In: Southwest Section AAPG, 2014 Annual Convention: West Texas Geological Society Publication, 1, pp. 38–39 (14–127).

Belica, M.E., 2017. Improving Early Prmian—Triassic Chronostratigraphic Correlation and the Apparent Polar Wander Path of Gondwana: A Magnetostratigraphic Investigation of the Kiaman Reverse Superchron. PhD, Perth, Australia.

Benton, M.J., Newell, A.J., 2014. Impacts of global warming on Permo-Triassic terrestrial ecosystems. Gondwana Res. 25 (4), 1308–1337.

Betekhtina, O.A., 1974. Non-Marine bivalve's Biostratigraphy and Correlation of Late Paleozoic Coal Measure. Nauka, Novosibirsk (In Russian).

Betekhtina, O.A., 1990. Freshwater mollusks of Tailugan Formation of Kuznets Basin (upper Permian). In: Elkin, E.A. (Ed.), Updates in Paleontology and Stratigraphy of the Paleozoic in the Asian Part of USSR. Nauka, Novosibirsk, pp. 132–140 (In Russian).

Betekhtina, O.A., Gorelova, S.L., 1965. Paleoecological zoning of Kuznetsk Basin territory in late Paleozoic. Int. Geol. Rev. 7 (12), 2091–2101.
Betekhtina, O.A., Mogucheva, N.K., Batyaeva, S.K., Kushnarev, M.P., 1986. Permian-Triassic boundary in the type section of Mal'tsev Formation of Kuzbass. In: Yanshin, A.L; Dagis, A.S; Biostratigraphy of the Mezoic of Siberia and Far East of Russia. Trans. Inst. Geol. Geophys. Novosibirsk 648, 31–38 (In Russian).
Betekhtina, O.A., Gorelova, S.G., Dryagina, L.L., Danilov, V.I., Batyayeva, S.P., Tokareva, P.A., 1988. Upper Paleozoic of Angarida. Flora and Fauna. Nauka, Novosibirsk (In Russian).
Biakov, A.S., Vedernikov, I.L., Brynko, I.V., 2020. The improvement of the regional startigraphic scale of the Permian of North-East Russia: results and achievements of the recent years. Vestnik North-East Scientific Center (1), 47-56 (IN Russian).
Bjerager, M., Seidler, L., Stemmerik, L., Surlyk, F., 2006. Ammonoid stratigraphy and sedimentary evolution across the Permian–Triassic boundary in East Greenland. Geol. Mag. 143 (5), 635–656.
Błędzki, L.A., Rybak, J., 2016. Freshwater crustacean zooplankton of Europe: Cladocera & copepoda (calanoida, cyclopoida) key to species identification, with notes on ecology, distribution, methods and introduction to data analysis / Leszek A. In: Bledzki, Joanna Rybak. Springer, Cham.
Blomenkemper, P., Kerp, H., Abu Hamad, A., DiMichele, W.A., Bomfleur, B., 2018. A hidden cradle of plant evolution in Permian tropical lowlands. Science (New York, N.Y.) 362 (6421), 1414–1416.
Bogomazov, V.M., Verbitskaya, N.G., Zolotov, A.P., Faddeeva, I.Z., 1996. Stratigraphy and environments of Kol'chugin Series in Kuznets basin. In: Budnikov, I.V. (Ed.), Kuzbass - a key region for the Upper Paleozoic stratigraphy in Angarida. Intergeo, 122 p., Novosibirsk, 104-114 (In Russian).
Bond, D.P., Grasby, S.E., 2017. On the causes of mass extinctions. Palaeogeogr. Palaeocimatol. Palaeogeogr. 478, 3–29.
Bond, D.P., Wignall, P.B., 2014. Large igneous provinces and mass extinctions: An update. In: Keller, G., Kerr, A.C. (Eds.), Volcanism, Impacts, and Mass Extinctions: Causes and Effects, vol. 505. Geological Society of America, pp. 29–55.
Botha-Brink, J., Huttenlocker, A.K., Smith, R.M., Prevec, R., Viglietti, P., Modesto, S.P., 2020. New geochemical and palaeontological data from the Permian-Triassic boundary in the South African Karoo Basin test the synchronicity of terrestrial and marine extinctions. Palaeogeogr. Palaeocimatol. Palaeogeogr. 540, 109467.
Bowring, S.A., Erwin, D.H., Jin, Y.G., Martin, M.W., Davidek, K., Wang, W., 1998. U/Pb Zircon Geochronology and Tempo of the End-Permian Mass Extinction. Science (Washington) 280 (5366), 1039–1045.
Bowring, S.A., Erwin, D.H., Isozaki, Y., 1999. The tempo of mass extinction and recovery: the end-Permian example. Proc. Natl. Acad. Sci. 96 (16), 8827.
Brayard, A., Escarguel, G., Bucher, H., Monnet, C., Brühwiler, T., Goudemand, N., Galfetti, T., Guex, J., 2009. Good genes and good luck: ammonoid diversity and the end-Permian mass extinction. Science (New York, N.Y.) 325 (5944), 1118–1121.
Brennecka, G.A., Herrmann, A.D., Algeo, T.J., Anbar, A.D., 2011. Rapid expansion of oceanic anoxia immediately before the end-Permian mass extinction. Proc. Natl. Acad. Sci. 108 (43), 17631.
Brookfield, M.E., Williams, J., Stebbins, A.G., 2020. Geochemistry of the new Permian-Triassic boundary section at Sitarička Glavica, Jadar block, Serbia. Chem. Geol. 550, 119696.
Brosse, M., Bucher, H., Goudemand, N., 2016. Quantitative biochronology of the Permian–Triassic boundary in South China based on conodont unitary associations. Earth Sci. Rev. 155, 153–171.
Kuzbass - a key region for the Upper Paleozoic stratigraphy in Angarida. In: Budnikov, I. V. (Ed.), 1996. Intergeo, 122 p., Novosibirsk, (In Russian).
Burger, B.J., Vargas Estrada, M., Gustin, M.S., 2019. What caused Earth's largest mass extinction event? New evidence from the Permian-Triassic boundary in northeastern Utah. Glob. Planet. Chang. 177, 81–100.
Burgess, S.D., Bowring, S.A., 2015. High-precision geochronology confirms voluminous magmatism before, during, and after Earth's most severe extinction. Sci. Adv. 1 (7), e1500470.
Burgess, S.D., Bowring, S., Shen, S., 2014. High-precision timeline for Earth's most severe extinction. Proc. Natl. Acad. Sci. 111 (9), 3316.
Burgess, S.D., Muirhead, J.D., Bowring, S.A., 2017. Initial pulse of Siberian Traps sills as the trigger of the end-Permian mass extinction. Nat. Commun. 8 (1), 164.
Burrows, M.T., Schoeman, D.S., Buckley, L.B., Moore, P., Poloczanska, E.S., Brander, K. M., Brown, C., Bruno, J.F., Duarte, C.M., Halpern, B.S., Holding, J., Kappel, C.V., Kiessling, W., O'Connor, M.I., Pandolfi, J.M., Parmesan, C., Schwing, F.B., Sydeman, W.J., Richardson, A.J., 2011. The pace of shifting climate in marine and terrestrial ecosystems. Science 334 (6056), 652–655.
Buslov, M.M., Safonova, I., Fedoseev, G.S., Reichow, M.K., Davies, K., Babin, G.A., 2010. Permo-Triassic plume magmatism of the Kuznetsk Basin, Central Asia: geology, geochronology, and geochemistry. Russ. Geol. Geophys. 51 (9), 1021–1036.
Cao, C., Wang, W., Liu, L., Shen, S., Summons, R.E., 2008. Two episodes of 13C-depletion in organic carbon in the latest Permian: evidence from the terrestrial sequences in northern Xinjiang, China. Earth Planet. Sci. Lett. 270 (3–4), 251–257.
Cao, W., Zahirovic, S., Flament, N., Williams, S., Golonka, J., Müller, R.D., 2017. Improving global paleogeography since the late Paleozoic using paleobiology. Biogeosci. Discuss. 14 (23), 5425–5439.
Chen, Z., Benton, M.J., 2012. The timing and pattern of biotic recovery following the end-Permian mass extinction. Nat. Geosci. 5 (6), 375–383.
Chen, B., Joachimski, M.M., Shen, S., Lambert, L.L., LAI, X., Wang, X., Chen, J., Yuan, D., 2013. Permian ice volume and palaeoclimate history; oxygen isotope proxies revisited. Gondwana Res. 24 (1), 77–89.
Cherepovskiy, V.F. (Ed.), 2003. Coal Reservoirs of Russia, vol. 2. Coal Basins of West Siberia. Geoinformmark, Moscow, 604 p. (In Russian).
Chu, D., Yu, J., Tong, J., Benton, M.J., Song, H., Huang, Y., Song, T., Tian, L., 2016. Biostratigraphic correlation and mass extinction during the Permian-Triassic transition in terrestrial-marine siliciclastic settings of South China. Glob. Planet. Chang. 146, 67–88.
Chu, D., Grasby, S.E., Song, H., Dal Corso, J., Wang, Y., Mather, T.A., Wu, Y., Song, H., Shu, W., Tong, J., Wignall, P.B., 2020. Ecological disturbance in tropical peatlands prior to marine Permian-Triassic mass extinction. Geology 48 (3), 288–292.
Clapham, M.E., 2013. The End-Permian mass extinction. In: Earth Systems and Environmental Sciences. Elsevier [Place of publication not identified].
Clapham, M.E., Payne, J.L., 2011. Acidification, anoxia, and extinction: a multiple logistic regression analysis of extinction selectivity during the Middle and Late Permian. Geology 39 (11), 1059–1062.
Clapham, M.E., Renne, P.R., 2019. Flood basalts and mass extinctions. Annu. Rev. Earth Planet. Sci. 47 (1), 275–303.
Close, R.A., Benson, R.B.J., Saupe, E.E., Clapham, M.E., Butler, R.J., 2020. The spatial structure of Phanerozoic marine animal diversity. Science (New York, N.Y.) 368 (6489), 420–424.
Condon, D.J., Schoene, B., McLean, N.M., Bowring, S.A., Parrish, R.R., 2015. Metrology and traceability of U–Pb isotope dilution geochronology (EARTHTIME Tracer Calibration Part I). Geochimica et Cosmochimica Acta 164, 464–480.
Cowling, R.M., Samways, M.J., 1994. Predicting global patterns of endemic plant species richness. Biodivers. Lett. 2 (5), 127.
Crasquin, S., Forel, M.-B., 2014. Ostracods (Crustacea) through Permian–Triassic events. Earth Sci. Rev. 137, 52–64.
Dagis, A.S., Ustritsky, V.I., 1971. Patterns of marine faunal distribution and evolution in the uppermost Permian and lowermost Triassic. Bull. Can. Petrol. Geol. 19 (2), 324.
Davies, C.E., Allen, M.B., Buslov, M.M., Safonova, I.Y., 2010. Deposition in the Kuznetsk Basin, Siberia: insights into the Permian–Triassic transition and the Mesozoic evolution of Central Asia. Palaeogeogr. Palaeocimatol. Palaeogeogr. 295, 307–322.
Davydov, V.I., 2021. Tunguska coals, Siberian sills and the Permian-Triassic extinction. Earth Sci. Rev. 212, 103438 (in press).
Davydov, V.I., Biakov, A.S., 2015. Discovery of shallow-marine biofacies conodonts in a bioherm within the Carboniferous–Permian transition in the Omolon Massif, NE Russia near the North paleo-pole: correlation with a warming spike in the southern hemisphere. Gondwana Res. 28 (2), 888–897.
Davydov, V.I., Crowley, J.L., Schmitz, M.D., Poletaev, V.I., 2010. High-precision U-Pb zircon age calibration of the global Carboniferous time scale and Milankovitch band cyclicity in the Donets Basin, eastern Ukraine. Geochem. Geophys. Geosyst. 11 (2), 1–22.
Davydov, V.I., Biakov, A.S., Isbell, J.L., Crowley, J.L., Schmitz, M.D., Vedernikov, I.L., 2016. Middle Permian U–Pb zircon ages of the "glacial" deposits of the Atkan Formation, Ayan-Yuryakh anticlinorium, Magadan province, NE Russia: their significance for global climatic interpretations. Gondwana Res. 38, 74–85.
Davydov, V.I., Biakov, A.S., Schmitz, M.D., Silantiev, V.V., 2018. Radioisotopic calibration of the Guadalupian (middle Permian) series: review and updates. Earth Sci. Rev. 176, 222–240.
Davydov, V.I., Karasev, E.V., Schmitz, M.D., Nurgalieva, N.G., Silantiev, V.V., Kuzina, D., Biakov, A.S., Gareev, B.I., Vasilenko, D.V., Zorina, S.O., Zharinova, V.V., Brunko, I. V., Lavrukhina, M.A., 2019a. Were the Siberian Traps a trigger for the global Permo-Triassic extinction? In: Nurgaliev, D.K. (Ed.), Late Paleozoic Sedimentary Earth Systems: Stratigraphy, Geochronology, Petroleum Resources: Abstract Volume of Kazan Golovkinsky Stratigraphic Meeting 2019 (September 24–28, 2019, Kazan, Russia). Kazan Federal University Press, pp. 87–88, 329 p., Kazan.
Davydov, V.I., Karasev, E.V., Zharinova, V.V., 2021. **Field evidence for coal combustion links the 252 Ma Siberian Traps with global carbon disruption**. Comment:. Geology 49, 517.
Davydov, V.I., Zharinova, V.V., Silantiev, V.V., 2019b. Late Permian and Early Triassic conchostracans from the Babyi Kamen section (Kuznetsk coal basin), Russia. Scientific notes of Kazan University. Nat. Sci. Ser. 161 (2), 339–347.
Davydov, V.I., Arefiev, M.P., Golubev, V.K., Karasev, E.V., Naumcheva, M.A., Schmitz, M.D., Silantiev, V.V., Zharinova, V.V., 2020. Radioisotopic and biostratigraphic constraints on the classical Middle–Upper Permian succession and tetrapod fauna of the Moscow syneclise, Russia. Geology 48 (7), 742–747.
de Wever, P., O'Dogherty, L., Goričan, Š., 2006. The plankton turnover at the Permo-Triassic boundary, emphasis on radiolarians. Eclogae Geol. Helv. 99 (S1), S49–S62.
DiMichele, W.A., 2014. Wetland-dryland vegetational dynamics in the Pennsylvanian ice age tropics. International Journal of Plant Sciences, 175(2), 123-164. Int. J. Plant Sci. 175 (2), 123–164.
Dmitriev, V.Y., Aristov, D.S., Bashkuev, A.S., Vasilenko, D.V., Vřsanský, P., Gorochov, A. V., Lukashevitch, E.D., Mostovski, M.B., Ponomarenko, A.G., Popov, Y.A., Rasnitsyn, A.P., Sinitshenkova, N.D., Sukatsheva, I.D., Tarasenkova, M.M., Khramov, A.V., Shmakov, A.S., 2018. Insect Diversity from the Carboniferous to Recent. Paleontol. J. 52 (6), 610–619.
Dobruskina, I.A., 1994. Triassic Floras of Eurasia. Springer, Wien, 422 pp.
Dobruskina, I.A., Durante, M.V., 2004. Restructuring of flora at the paleophyte and mesophyte boundary linked to global climate change. In: Durante, M.V., Ignatiev, I. A. (Eds.), Plant World in Space and Time. GEOS, Moscow, 2004. - 197 p. GEOS, Moscow, (In Russian).
Efremov, I.A., V'yushkov, B.P., 1955. Catalogue of Localities of Permian and Triassic Terrestrial Vertebrates in the Territories of the U.S.S.R. Moscow, 1-185 pp., (In Russian).
Ernst, R.E., Youbi, N., 2017. How large Igneous Provinces affect global climate, sometimes cause mass extinctions, and represent natural markers in the geological record. Palaeogeogr. Palaeocimatol. Palaeogeogr. 478, 30–52.

Felker, A.S., 2021. The first damselflies of the family Kennedyidae (Odonata: Protozygoptera) from the Permian-Triassic boundary deposits of the Kuznetsk basin, Russia. Paleontol. J. 2, 52–59 (In Russian).
Feng, Q., He, W., Gu, S., Meng, Y., Jin, Y., Zhang, F., 2007. Radiolarian evolution during the latest Permian in South China. Glob. Planet. Chang. 55 (1–3), 177–192.
Feng, Z., Wei, H.-B., Guo, Y., He, X.-Y., Sui, Q., Zhou, Y., Liu, H.-Y., Gou, X.-D., Lv, Y., 2020. From rainforest to herbland: new insights into land plant responses to the end-Permian mass extinction. Earth Sci. Rev. 204, 103153.
Fielding, C.R., Frank, T.D., Birgenheier, L.P., Rygel, M.C., Jones, A.T., Roberts, J., 2008. Stratigraphic imprint of the Late Palaeozoic Ice Age in eastern Australia: a record of alternating glacial and nonglacial climate regime. J. Geol. Soc. 165 (1), 129–140.
Fielding, C.R., Frank, T.D., McLoughlin, S., Vajda, V., Mays, C., Tevyaw, A.P., Winguth, A., Winguth, C., Nicoll, R.S., Bocking, M., Crowley, J.L., 2019. Age and pattern of the southern high-latitude continental end-Permian extinction constrained by multiproxy analysis. Nat. Commun. 10 (1), 385.
Flessa, K.W., Erben, H.K., Hallam, A., Hsii, K.J., Hiissner, H.M., Jablonski, D., Raup, D. M., Sepkoski, J.J., Soule, M.E., Sousa, W., Stinnesbeck, W., Vermeij, G.J., 1986. Mass extinctions, extinction events, and background extinctions. In: Raup, D.M., Jablonski, D. (Eds.), Patterns and Processes in the History of Life. Report of the Dahlem Workshop on Patterns and Processes in the History of Life Berlin 1985, June 16–21. Springer Berlin Heidelberg, Berlin, Heidelberg, pp. 257–275.
Foote, M., 2000. Origination and extinction components of taxonomic diversity: general problems. Paleobiology 26 (sp4), 74–102.
Forel, M.-B., 2012. Biodiversity Evolution through the Permian-Triassic Boundary Event: Ostracods from the Bükk Mountains. APP, Hungary.
Garzanti, E., Padoan, M., Setti, M., Najman, Y., Peruta, L., Villa, I.M., 2013. Weathering geochemistry and Sr-Nd fingerprints of equatorial upper Nile and Congo muds. Geochem. Geophys. Geosyst. 14 (2), 292–316.
Gastaldo, R.A., Kamo, S.L., Neveling, J., Geissman, J.W., Bamford, M., Looy, C.V., 2015. Is the vertebrate-defined Permian-Triassic boundary in the Karoo Basin, South Africa, the terrestrial expression of the end-Permian marine event? Geology 43 (10), 939–942.
Gastaldo, R.A., Kamo, S.L., Neveling, J., Geissman, J.W., Looy, C.V., Martini, A.M., 2020. The base of the *Lystrosaurus* Assemblage Zone, Karoo Basin, predates the end-Permian marine extinction. Nat. Commun. 11 (1), 1428.
Gastaldo, R.A., Neveling, J., Geissman, J.W., Kamo, S.L., 2018. A lithostratigraphic and magnetostratigraphic framework in a geochronologic context for a purported Permian–Triassic boundary section at Old (West) Lootsberg Pass, Karoo Basin, South Africa. In. Bulletin of the Geological Society of America 130 (9–10), 1411–1438. https://doi.org/10.1130/B31881.1.
Grasby, S.E., Beauchamp, B., Embry, A., Sanei, H., 2013. Recurrent Early Triassic ocean anoxia. Geology 41 (2), 175–178.
Guo, G., Tong, J., Zhang, S., Zhang, J., Bai, L., 2008. Cyclostratigraphy of the Induan (early Triassic) in West Pingdingshan Section, Chaohu, Anhui Province. Sci. China Ser. D-Earth Sci. 51 (1), 22–29.
Hallam, A., Wignall, P.B., 1997. Mass Extinctions and their Aftermath. Oxford University Press, Oxford.
Hansen, H.J., Lojen, S., Toft, P., Dolenec, T., Tong, J., Michaelsen, P., Sarkar, A., 2000. Magnetic susceptibility and organic carbon isotopes of sediments across some marine and terrestrial Permo-Triassic boundaries. In: Yin, H.-F., Dickins, J.M., Shi, G.R., Tong, J. (Eds.), Permian-Triassic Evolution of Tethys and Western Circum-Pacific. Elsevier, Amsterdam, Oxford, pp. 271–289.
Haslett, J., Parnell, A., 2008. A simple monotone process with application to radiocarbon-dated depth chronologies. Journal of the Royal Statistical Society: Series C (Applied Statistics) 57 (4), 399–418.
Hayashi, K.-I., Fujisawa, H., Holland, H.D., Ohmoto, H., 1997. Geochemistry of ~1.9 Ga sedimentary rocks from northeastern Labrador, Canada. Geochim. Cosmochim. Acta 61 (19), 4115–4137.
Henderson, C.M., Davydov, V.I., Wardlaw, B.R., Gradstein, F.M., Hammer, O., 2012. Chapter 24 - the Permian Period. In: Gradstein, F.M., Ogg, J.G., Schmitz, M.D., Ogg, G.M. (Eds.), The Geologic Time Scale. Elsevier, Boston, pp. 653–679.
Hermann, E., Hochuli, P.A., Bucher, H., Vigran, J.O., Weissert, H., Bernasconi, S.M., 2010. A close-up view of the Permian–Triassic boundary based on expanded organic carbon isotope records from Norway (Trøndelag and Finnmark Platform). Glob. Planet. Chang. 74 (3–4), 156–167.
Hounslow, M.W., Balabanov, Y.P., 2018. A geomagnetic polarity timescale for the Permian, calibrated to stage boundaries. In: Lucas, S.G., Shen, S. (Eds.), The Permian Times. Special Publications, pp. 61–103.
Hunt, J.W., 1988. Sedimentation rates and coal formation in the Permian basins of eastern Australia. Aust. J. Earth Sci. 35 (2), 259–274.
Hurd, C.L., Lenton, A., Tilbrook, B., Boyd, P.W., 2018. Current understanding and challenges for oceans in a higher-CO_2 world. Nat. Clim. Chang. 8 (8), 686–694.
Jaffey, A.H., Flynn, K.F., Glendenin, L.E., Bentley, W.T., Essling, A.M., 1971. Precision measurement of half-lives and specific activities of U 235 and U 238. Physical Review C 4, 1889–1906.
Jerram, D.A., Svensen, H.H., Planke, S., Polozov, A.G., Torsvik, T.H., 2016. The onset of flood volcanism in the north-western part of the Siberian Traps: Explosive volcanism versus effusive lava flows. Palaeogeogr. Palaeocimatol. Palaeogeogr. 441, 38–50.
Joachimski, M.M., Lai, X., Shen, S., Jiang, H., Luo, G., Chen, B., Chen, J., Sun, Y., 2012. Climate warming in the latest Permian and the Permian–Triassic mass extinction. Geology 40 (3), 195–198.
Jin, Y., Wang, Y., Henderson, Ch.s, M., Wardlaw, B.R., Shen, Sh., Cao, Ch., 2006. The Global Boundary Stratotype Section and Point (GSSP) for the base of Changhsingian Stage (Upper Permian). In. Episodes 29 (3), 175–182.
Joachimski, M.M., Alekseev, A.S., Grigoryan, A., Gatovsky, Y., 2020. Siberian Trap volcanism, global warming and the Permian-Triassic mass extinction: New insights from Armenian Permian-Triassic sections. Bull. Geol. Soc. Am. 132 (1–2), 427–443.
Johansson, L., Zahirovic, S., Müller, R.D., 2018. The interplay between the eruption and weathering of Large Igneous Provinces and the deep-time carbon cycle. Geophys. Res. Lett. 45 (11), 5380–5389.
JunHenderson, Ch.C. M., Shen, Sh., 2005. Discussion on Late Permian-Early Triassic conodonts. Morphological variation and evolutionary succession. Permophiles 45, 22–26.
Kamo, S.L., Czamanske, G.K., Amelin, Y., Fedorenko, V.A., Davis, D.W., Trofimov, V.R., 2003. Rapid eruption of Siberian flood-volcanic rocks and evidence for coincidence with the Permian-Triassic boundary and mass extinction at 251 Ma. Earth Planet. Sci. Lett. 214 (1–2), 75–91.
Karanovic, I., 2012. Recent Freshwater Ostracods of the World: Crustacea, Ostracoda, Podocopida, 608. Springer, Berlin, New York xiii.
Karasev, E., 2015. On small pinnate leaves of Peltasperm Pteridosperms from the Early Triassic of the Kuznetsk Basin (Mal'tsevo Formation, Babii Kamen Locality). Bot Pac. 4 (2), 131–136.
Kazakov, A.M., 2002. Stratigraphy of oil-gas bearing basins of Siberia. In: Triassic System. GEO, 327 p., Novosibirsk, (In Russian).
Kerp, H., 1996. Post-Variscan late Palaeozoic Northern Hemisphere gymnosperms: the onset to the Mesozoic. Rev. Palaeobot. Palynol. 90 (3–4), 263–285.
Kerp, H., 2000. The modernization of landscapes during the Late Paleozoic-Early Mesozoic. Paleontol. Soc. pap. 6, 79–114.
Kershaw, S., Crasquin, S., Li, Y., Collin, P.-Y., Forel, M.-B., 2012. Ocean Acidification and the End-Permian Mass Extinction: to what extent does evidence support hypothesis? Geosciences 2 (4), 221–234.
Kiessling, W., Schobben, M., Ghaderi, A., Hairapetian, V., Leda, L., Korn, D., 2018. Pre–mass extinction decline of latest Permian ammonoids. Geology 46 (3), 283–286.
Kirillov, V.N., 1971. Paleomagnetic and Stratigraphic Studies of Coal-Bearing Sequences of Kuznets Basin. Extended abstract of PhD dissertation., Krasnoyarsk, 26 p. (In Russian).
Knoll, A.H., Bambach, R.K., Payne, J.L., Pruss, S., Fischer, W.W., 2007. Paleophysiology and end-Permian mass extinction. Earth Planet. Sci. Lett. 256 (3), 295–313.
Korn, D., Chaderi, A., Kiessling, W., 2019. Ammonoid evolution and early warning signs for global warming during the end-Permian mass extinction. In: Program and Abstracts 2nd International REKLIM Conference, p. 78.
Korte, C., Kozur, H., 2005. Carbon isotope stratigraphy across the Permian/Triassic boundary Jolfa (NW Iran), Peitlerkofel (Sass de Putia), Pufels (Bula, bulla), Tesero (all three southern Alps, Italy) and Gerennavar (Bükk Mtns., Hungary). In Journal of Alpine Geology 47, 119–135.
Korte, Ch., Pande, P., Kalia, P., Kozur, H.W., JoachimskyI, M.M., Oberhänsli, H., 2010. Massive volcanism at the Permian–Triassic boundary and its impact on the isotopic composition of the ocean and atmosphere. Journal of Asian Earth Sciences 37 (4), 293–311. https://doi.org/10.1016/j.jseaes.2009.08.012.
Korte, Ch., Kozur, H.W., 2010. Carbon-isotope stratigraphy across the Permian–Triassic boundary: A review. In. Journal of Asian Earth Sciences 39 (4), 215–235. https://doi.org/10.1016/j.jseaes.2010.01.005.
Kozur, H., 2005. Pelagic uppermost Permian and the Permian-Triassic boundary conodonts of Iran. Part 2. Investigated sections and evaluation of the conodont faunas. In *Hallesches Jahrb*. Geowiss., B Beiheft 19, 49–86.
Kozur, H.W., 2007. Biostratigraphy and event stratigraphy in Iran around the Permian–Triassic Boundary (PTB): Implications for the causes of the PTB biotic crisis. Global and Planetary Change 55 (1), 155–176.
Kozur, H.W., Wardlaw, B.R., 2010. The Guadalupian conodont fauna of Rustaq and Wadi Wasit, Oman and a West Texas connection. Micropaleontology 56 (1/2), 213–231.
Krassilov, V.A., Karasev, E.V., 2009. Paleofloristic evidence of climate change near and beyond the Permian–Triassic boundary. Palaeogeography, Palaeocimatology and Palaeogeography 284 (3–4), 326–336.
Krull, E.S., Retallack, G.J., 2000. Delta super(13)C depth profiles from paleosols across the Permian-Triassic boundary: evidence for methane release. Bull. Geol. Soc. Am. 112 (9), 1459–1472.
Kukhtinov, D.A., Mishina, E.M., Neustrueva, I., 1986. Ostracods. In: Oleinikov, A.N., Zhamoida, A.I. (Eds.), Parastratigraphic Groups of flora and Fauna. Transactions of VSEGEI, New Series, Leningrad, Nedra, 334, pp. 216–282 (In Russian).
Kump, L.R., Pavlov, A., Arthur, M.A., 2005. Massive release of hydrogen sulfide to the surface ocean and atmosphere during intervals of oceanic anoxia. Geology 33 (5), 397–400.
Kurushin, N.I., 1992. Triassic Paleogeterodontian and Geterodontian Bivalves of Siberia. Nauka, Novosibirsk (In Russian).
Kusky, T.M., 2008. Volcanoes: Eruptions and other volcanic hazards / Timothy Kusky. In: Facts on File; London: Eurospan [distributor], New York.
Kustatscher, E., Bernardi, M., Petti, F.M., Franz, M., van Konijnenburg-van Cittert, J.H., Kerp, H., 2017. Sea-level changes in the Lopingian (late Permian) of the northwestern Tethys and their effects on the terrestrial palaeoenvironments, biota and fossil preservation. Global and Planetary Change 148, 166–180.
Kuzina, D., Fetisova, A., Gilmetdinov, I., Radmir, Ayupov, Davydov, V., Silantiev, V., 2019a. Paleomagnetic data on samples from Babii Kamen (Kuznetsk Basin). In: Nurgaliev, D.K. (Ed.), Sedimentary Earth Systems: Stratigraphy, Geochronology. Petroleum Resources. Filodiritto Editore, Bologna, Italy, pp. 146–150.
Kuzina, D., Kosareva, L., Gilmetdinov, I., Aupov, R., Silantiev, V., Davydov, V., Dogadina, I., Kuzmina, N., 2019b. Preliminary magnetic investigation of samples from reference Permian-Triassic sequence, Kemerovo Region, Russia. In: Nurgaliev, D., Shcherbakov, V., Kosterov, A., Spassov, S. (Eds.), Nurgaliev, D., Shcherbakov, V., Kosterov, A., Spassov, S. (Eds.), Recent Advances in Rock Magnetism, Environmental Magnetism and Paleomagnetism. International

Conference on Geomagnetism, Paleomagnetism and Rock Magnetism (Kazan, Russia). Springer, Cham, Switzerland, pp. 225–234.
Latter, J.H., 2013. Volcanic Hazards: Assessment and Monitoring. Springer, Berlin, Berlin, 625 pp.
Lehrmann, D.J., Stepchinski, L., Altiner, D., Orchard, M.J., Montgomery, P., Enos, P., Ellwood, B.B., Bowring, S.A., Ramezani, J., Wang, H., Wei, J., Yu, M., Griffiths, J.D., Minzoni, M., Schaal, E.K., Li, X., Meyer, K.M., Payne, J.L., 2015. An integrated biostratigraphy (conodonts and foraminifers) and chronostratigraphy (paleomagnetic reversals, magnetic susceptibility, elemental chemistry, carbon isotopes and geochronology) for the Permian–Upper Triassic strata of Guandao section, Nanpanjiang Basin, South China. J. Asian Earth Sci. 108, 117–135.
Lehtonen, S., Silvestro, D., Karger, D.N., Scotese, C., Tuomisto, H., Kessler, M., Peña, C., Wahlberg, N., Antonelli, A., 2017. Environmentally driven extinction and opportunistic origination explain fern diversification patterns. Sci. Rep. 7 (1), 4831.
Lenoir, J., Bertrand, R., Comte, L., Bourgeaud, L., Hattab, T., Murienne, J., Grenouillet, G., 2020. Species better track climate warming in the oceans than on land. Nat. Ecol. Evol. 4, 1044–1059.
Lenssen, N.J.L., Schmidt, G.A., Hansen, J.E., Menne, M.J., Persin, A., Ruedy, R., Zyss, D., 2019. Improvements in the GISTEMP uncertainty Model. J. Geophys. Res. Atmos. 124 (12), 6307–6326.
Logan, A., Hills, L.V. (Eds.), 1973. Permian and Triassic Systems and their Mutual Boundary. Memoir Canadian Society of Petroleum Geologists, Issue, vol. 2. Canadian Society of Petroleum Geologists, Calgary, Canada.
Macdonald, F.A., Schmitz, M.D., Strauss, J.V., Halverson, G.P., Gibson, T.M., Eyster, A., Cox, G., Mamrol, P., Crowley, J.L., 2018. Cryogenian of Yukon. Precambrian Research 319, 114–143.
Mattinson, J.M., 2005. Zircon U–Pb chemical abrasion ("CA-TIMS") method: Combined annealing and multi-step partial dissolution analysis for improved precision and accuracy of zircon ages. Chemical Geology 220 (1–2), 47–66.
Mays, C., Vajda, V., Frank, T.D., Fielding, C.R., Nicoll, R.S., Tevyaw, A.P., McLoughlin, S., 2019. Refined Permian–Triassic floristic timeline reveals early collapse and delayed recovery of south polar terrestrial ecosystems. GSA Bull. 132, 1489–1513.
McLean, N.M., Condon, D.J., Schoene, B., Bowring, S.A., 2015. Evaluating uncertainties in the calibration of isotopic reference materials and multi-element isotopic tracers (EARTHTIME Tracer Calibration Part II). Geochimica et Cosmochimica Acta 164, 481–501.
McLennan, S.M., Hemming, S., McDaniel, D.K., Hanson, G.N., 1993. Geochemical approaches to sedimentation, provenance, and tectonics. In: Johnsson, M.J., Basu, A. (Eds.), Processes Controlling the Composition of Clastic Sediments, 284. Geological Society of America Special Paper, Boulder, CO, USA, pp. 21–40.
Mei, S., Zhang, K., Wardlaw, B.R., 1998. A refined succession of Changhsingian and Griesbachian neogondolellid conodonts from the Meishan section, candidate of the global stratotype section and point of the Permian–Triassic boundary. Palaeogeogr. Palaeocimatol. Palaeogeogr. 143 (4), 213–226.
Metcalfe, I., Crowley, J.L., Nicoll, R.S., Schmitz, M., 2015. High-precision U-Pb CA-TIMS calibration of Middle Permian to Lower Triassic sequences, mass extinction and extreme climate-change in eastern Australian Gondwana. Gondwana Res. 28 (1), 61–81.
Meyen, S.V., 2002. On the Subangara Palaeofloristic Area of the Permian. GEOS, Moscow (In Russian).
Meyer, K.M., Kump, L.R., Ridgwell, A., 2008. Biogeochemical controls on photic-zone euxinia during the end-Permian mass extinction. Geology 36 (9), 747–750.
Mogucheva, N.K., 1973. Early Triassic Flora of Tunguska Basin. Nedra, Moscow (In Russian).
Mogucheva, N.K., 2016. Flora from the Induan stage (Lower Triassic) of Middle Siberia. Stratigr. Geol. Correl. 24 (3), 252–266.
Mogucheva, N.K., Krugovykh, V.V., 2009. New data on the stratigraphic chart for Triassic deposits in the Tunguska syneclise and Kuznetsk basin. Stratigr. Geol. Correl. 17 (5), 510–518.
Mogucheva, N.K., Naugolnykh, S.V., 2010. *Gagariostrobus cylindricus* (Prynada) Mogutcheva and the Permian—Triassic Ecosystem Flora Reorganization in the Tunguska Basin. Stratigr. Geol. Correl. 18 (1), 31–41.
Moisan, P., Voigt, S., Pott, C., Buchwitz, M., Schneider, J.W., Kerp, H., 2011. Cycadalean and bennettitalean foliage from the Triassic Madygen Lagerstätte (SW Kyrgyzstan, Central Asia). Review of Palaeobotany and Palynology 164 (1–2), 93–108.
Molinos, G.J., Halpern, B.S., Schoeman, D.S., Brown, C.J., Kiessling, W., Moore, P.J., Pandolfi, J.M., Poloczanska, E.S., Richardson, A.J., Burrows, M.T., 2016. Climate velocity and the future global redistribution of marine biodiversity. Nat. Clim. Chang. 6 (1), 83–88.
Müller, R.D., Cannon, J., Qin, X., Watson, R.J., Gurnis, M., Williams, S., Pfaffelmoser, T., Seton, M., Russell, S.H.J., Zahirovic, S., 2018. GPlates: building a virtual Earth through deep time. Geochem. Geophys. Geosyst. 19 (7), 2243–2261.
Mundil, R., Metcalfe, I., Ludwig, K.R., Renne, P.R., Oberli, F., Nicoll, R.S., 2001. Timing of the Permian–Triassic biotic crisis: implications from new zircon U/Pb age data (and their limitations). Earth Planet. Sci. Lett. 187 (1–2), 131–145.
Mundil, R., Ludwig, K.R., Metcalfe, I., Renne, P.R., 2004. Age and timing of the end Permian mass extinctions: U/Pb geochronology on closed-system zircons. Science 305, 1760–1763.
Nasdala, L., Lengauer, C.L., Hanchar, J.M., Kronz, A., Wirth, R., Blanc, P., Kennedy, A.K., Seydoux-Guillaume, A.-M., 2002. Annealing radiation damage and the recovery of cathodoluminescence. Chemical Geology 191 (1–3), 121–140.
Neiburg, M.F., 1936. On the stratigraphy of the coal-bearing deposits of the Kuznetsk Basin. Bulletin de l'Academie Des Sciences de l'URSS. Classe des Sciences Mathematiques et Naturelles 4, 471–515 (In Russian and English).
Nesbitt, H.W., Young, G.M., 1982. Early Proterozoic climates and plate motions inferred from major element chemistry of lutites. Nature 299 (5885), 715–717.
Neukom, R., Steiger, N., Gómez-Navarro, J.J., Wang, J., Werner, J.P., 2019. No evidence for globally coherent warm and cold periods over the preindustrial Common Era. Nature 571 (7766), 550–554.
Neustrueva, I.Y., 1966. Upper Permian ostracods of Kuznetsk Basin. In: Nalivkin, D.V. (Ed.), Terrestrial Upper Paleozoic and Mesozoic of Siberia and Central Kazakhstan. Nauka, Moscow, pp. 54–95, 184 p. (In Russian).
Newell, N.D., 1962. Paleontological gaps and geochronology. J. Paleontol. 36 (3), 592–610.
Newell, N.D., 1967. Revolutions in the history of life. In: Uniformity and Simplicity: A Symposium on the Principle of the Uniformity of Nature, vol. 89. Geological Society of America, pp. 63–92.
Nowak, H., Schneebeli-Hermann, E., Kustatscher, E., 2019. No mass extinction for land plants at the Permian-Triassic transition. Nat. Commun. 10 (1), 384.
Ogg, J.G., 2012. Chapter 25 - Triassic. In: Gradstein, F.M., Ogg, J.G., Schmitz, M.D., Ogg, G.M. (Eds.), The Geologic Time Scale. Elsevier, Boston, pp. 681–730.
Oppel, A., 1853. Der mittlere Lias Schwabens. Ebner & Seubert, Stuttgart, pp. 1–127.
Papin, Y.S., Chunikhin, S.A., 2007. Permian-Triassic boundary in Kuznetsk Basin as a regional stratotype for West Siberia. Lithosphere 4, 128–133 (In Russian).
Papin, Y.S., Lezhnin, A.I., 1998. Lithologic and paleontologic boundary between Permian and Triassic in the Kuznetsk basin. Zentralblatt fur Geologie und Palaeontologie, Teil I: Allgemeine, Angewandte, Regionale und Historische Geologie 1 (11−12), 1325–1336.
Payne, J.L., Clapham, M.E., 2012. End-Permian mass extinction in the oceans: an ancient analog for the twenty-first century? Annu. Rev. Earth Planet. Sci. 40 (1), 89–111.
Payne, J.L., Kump, L.R., 2007. Evidence for recurrent Early Triassic massive volcanism from quantitative interpretation of carbon isotope fluctuations. Earth Planet. Sci. Lett. 256 (1–2), 264–277.
Peate, I.U., Elkins-Tanton, L.T., 2015. Large igneous provinces and explosive basaltic volcanism. In: Schmidt, A., Fristad, K., Elkins-Tanton, L.T. (Eds.), Volcanism and Global Environmental Change. Cambridge University Press, Cambridge, pp. 3–15.
Peng, Y., Tong, J., Shi, G.R., Hansen, H.J., 2001. The Permian-Triassic Boundary Stratigraphic Set: characteristics and correlation. Newsl. Stratigr. 39 (1), 55–71.
Penn, J.L., Deutsch, C., Payne, J.L., Sperling, E.A., 2018. Temperature-dependent hypoxia explains biogeography and severity of end-Permian marine mass extinction. Science (New York, N.Y.) 362 (6419).
Pinsky, M.L., Eikeset, A.M., McCauley, D.J., Payne, J.L., Sunday, J.M., 2019. Greater vulnerability to warming of marine versus terrestrial ectotherms. Nature 569 (7754), 108–111.
Racki, G., 2020. Volcanism as a prime cause of mass extinctions: Retrospectives and perspectives. In: Adatte, T., Bond, D.P., Keller, G. (Eds.), Mass Extinctions, Volcanism, and Impacts: New Developments, vol. 544. Geological Society of America, pp. 1–34.
Radchenko, G.P., 1938. Description of sections along Tom' River from the mouth of Sueriekova River to Babyi Kamen' in Kuznets Basin. Mater. Geol. Western Siberia 47 (5), 147–149 (In Russian).
Radchenko, G.P., 1973. Altai-Sayany folded area. In: Gorsky, I.I., Kiparisova, L.D., Nalivkin, D.V., Radchenko, G.P. (Eds.), Stratigraphy of the USSR, Triassic System. Nedra Publishing House, Moscow, pp. 223–231 (In Russian).
Rasmussen, C., Brantley, S., Richter, D.d., Blum, A., Dixon, J., White, A.F., 2011. Strong climate and tectonic control on plagioclase weathering in granitic terrain. Earth Planet. Sci. Lett. 301 (3–4), 521–530.
Raup, D.M., Sepkoski, J.J., 1982. Mass Extinctions in the Marine Fossil Record. Sci. New Ser. 125 (4539), 1501–1503.
Reddin, C.J., Kocsis, Á.T., Kiessling, W., 2019. Climate change and the latitudinal selectivity of ancient marine extinctions. Paleobiology 45 (1), 70–84.
Reichow, M.K., Pringle, M.S., Al'Mukhamedov, A.I., Allen, M.B., Andreichev, V.L., Buslov, M.M., Davies, C.E., Fedoseev, G.S., Fitton, J.G., Inger, S., Medvedev, A., Mitchell, C., Puchkov, V.N., Safonova, I., Scott, R.A., Saunders, A.D., 2009. The timing and extent of the eruption of the Siberian Traps large igneous province: implications for the end-Permian environmental crisis. Earth Planet. Sci. Lett. 277 (1), 9–20.
Retallack, G.J., 2013. Permian and Triassic greenhouse crises. Gondwana Res. 24 (1), 90–103.
Retallack, G.J., Krull, E.S., 1999. Landscape ecological shift at the Permian-Triassic boundary in Antarctica. Aust. J. Earth Sci. 46 (5), 785–812.
Roopnarine, P.D., Angielczyk, K.D., 2015. Community stability and selective extinction during the Permian-Triassic mass extinction. Science (New York, N.Y.) 350 (6256), 90–93.
RStudio Team, 2015. RStudio: Integrated Development for R. RStudio, Inc., Boston, MA. http://www.rstudio.com. Accessed 15 July 2016.
Rudnick, R.L., Gao, S., 2014. Composition of the Continental Crust. In: Holland, H.D. (Ed.), Treatise on Geochemistry. Elsevier, Amsterdam, pp. 1–51.
Sadler, P.M., 2006. Composite time lines: A means to leverage resolving power from radioisotopic dates and biostratigraphy. In: The Paleontological Society Papers, 12, pp. 145–170.
Sadovnikov, G.N., 2008. On the global stratotype section and point of the Triassic base. Stratigr. Geol. Correl. 16 (1), 31–46.
Sadovnikov, G.N., 2016. Trap's volcanism of Siberia and "Permian-Triassic extinction". Geology of higher education. Geol. Explor. 2, 8–14 (In Russian).
Sanson-Barrera, A., Hochuli, P.A., Bucher, H., Schneebeli-Hermann, E., Weissert, H., Adatte, T., Bernasconi, S.M., 2015. Late Permian–earliest Triassic high-resolution organic carbon isotope and palynofacies records from Kap Stosch (East Greenland). Glob. Planet. Chang. 133, 149–166.

Schmitz, M.D., Davydov, V.I., 2012. Quantitative radiometric and biostratigraphic calibration of the Pennsylvanian-Early Permian (Cisuralian) time scale and pan-Euramerican chronostratigraphic correlation. Bull. Geol. Soc. Am. 124 (3–4), 549–577.
Schmitz, M.D., Schoene, B., 2007. Derivation of isotope ratios, errors, and error correlations for U-Pb geochronology using (super 205) Pb- (super 235) U-((super 233) U)-spiked isotope dilution thermal ionization mass spectrometric data. Geochemistry, Geophysics, Geosystems - G (super 3) 8, 8.
Schneebeli-Hermann, E., Kürschner, W.M., Kerp, H., Bomfleur, B., Hochuli, P.A., Bucher, H., Ware, D., Roohi, G., 2015. Vegetation history across the Permian–Triassic boundary in Pakistan (Amb section, Salt Range). Gondwana Res. 27 (3), 911–924.
Sepkoski, J.J., 1986. Phanerozoic overview of mass extinction. In: Raup, D.M., Jablonski, D. (Eds.), Patterns and Processes in the History of Life. Report of the Dahlem Workshop on Patterns and Processes in the History of Life Berlin 1985, June 16–21. Springer Berlin Heidelberg, Berlin, Heidelberg, pp. 277–295.
Sepkoski, J.J., 2002. A compendium of fossil marine animal genera. Bull. Am. Paleontol. 363, 1–560.
Sepkoski, J.J., 2012. Patterns of Phanerozoic extinction: A perspective from global data bases. In: Walliser, O.H. (Ed.), Global Events and Event Stratigraphy in the Phanerozoic. Results of International Interdisciplinary Cooperation in the IGCP PRoject 216 "Global Biological in Earth History". Springer, Göttingen, pp. 35–51.
Shcherbakov, D.E., 2008. On Permian and Triassic insect faunas in relation to biogeography and the Permian-Triassic crisis. Paleontol. J. 42 (1), 15–31.
Shen, S., Crowley, J.L., Wang, Y., Bowring, S.A., Erwin, D.H., Sadler, P.M., Cao, C., Rothman, D.H., Henderson, C.M., Ramezani, J., Zhang, H., Shen, Y., Wang, X., Wang, W., Mu, L., Li, W., Tang, Y., Liu, X., Liu, L., Zeng, Y., Jiang, Y., Jin, Y., 2011. Calibrating the end-Permian mass extinction. Science 334 (6061), 1367–1372.
Shen, S., Ramezani, R., Chen, J., Cao, C.-Q., Erwin, D.H., Zhang, H., Xiang, L., Schoepfer, S.D., Henderson, C., Zheng, Q.-F., Bowring, S.A., Wang, Y., Li, X.-H., Wang, X.-D., Yuan, D.-X., Zhang, Y.-C., Mu, L., Wang, J., Wu, Y.-S., 2019. A sudden end-Permian mass extinction in South China: /10.1130 /B31909.1. GSA Bull. 131 (1–2), 205–223.
Silantiev, V.V., 2018. Permian nonmarine Bivalve Mollusks: review of geographical and stratigraphic distribution. Paleontol. J. 52 (7), 707–729.
Silantiev, V.V., Urazaeva, M.N., 2021. Non-marine bivalves from volcano-silisiclastic succession of the Siberian trapp's province. In: Paleostrat-2021. Program and Abstracts, pp. 69–70 (In Russian).
Silantiev, V.V., Urazaeva, M.N., Nurgalieva, N.G., 2020. Non-marine bivalves from the terminal part of the Permian and the Early Triassic of Kuznetsk Basin. In: Paleostrat-2020. Program and Abstracts, pp. 53–54 (In Russian).
Skundin, V.S., 1974. Geological map of the USSR. In: Scale 1:200.000, Tunguska Series. Sheet Q-46-XXXV-XXXVI. Explanatory Notes. Moscow (In Russian).
Smith, R.M., Botha-Brink, J., 2014. Anatomy of a mass extinction: sedimentological and taphonomic evidence for drought-induced die-offs at the Permo-Triassic boundary in the main Karoo Basin, South Africa. Palaeogeogr. Palaeocimatol. Palaeogeogr. 396, 99–118.
Sobolev, S.V., Sobolev, A.V., Kuzmin, D.V., Krivolutskaya, N.A., Petrunin, A.G., Arndt, N. T., Radko, V.A., Vasiliev, Y.R., 2011. Linking mantle plumes, large igneous provinces and environmental catastrophes. Nature 477 (7364), 312–316.
Sobolev, A.V., Arndt, N.T., Krivolutskaya, N.A., Kuzmin, D.V., Sobolev, S.V., 2015. The origin of gases that caused the Permian–Triassic extinction. In: Schmidt, A., Fristad, K., Elkins-Tanton, L.T. (Eds.), Volcanism and Global Environmental Change. Cambridge University Press, Cambridge, pp. 147–163.
Song, H., Tong, J., Chen, Z.Q., 2009. Two episodes of foraminiferal extinction near the Permian–Triassic boundary at the Meishan section, South China. Aust. J. Earth Sci. 56 (6), 765–773.
Song, H., Wignall, P.B., Tong, J., Yin, H., 2013. Two pulses of extinction during the Permian–Triassic crisis. Nat. Geosci. 6 (1), 52–56.
Song, H., Wignall, P.B., Dunhill, A.M., 2018. Decoupled taxonomic and ecological recoveries from the Permo-Triassic extinction. Sci. Adv. 4 (10) eaat5091.
Stanley, S.M., 2016. Estimates of the magnitudes of major marine mass extinctions in earth history. Proc. Natl. Acad. Sci. 113 (42), E6325.
Susskind, J., Schmidt, G.A., Lee, J.N., Iredell, L., 2019. Recent global warming as confirmed by AIRS. Environ. Res. Lett. 14 (4), 44030.
Svensen, H., Planke, S., Polozov, A.G., Schmidbauer, N., Corfu, F., Podladchikov, Y.Y., Jamtveit, B., 2009. Siberian gas venting and the end-Permian environmental crisis. Earth Planet. Sci. Lett. 277 (3), 490–500.
Svensen, H.H., Frolov, S., Akhmanov, G.G., Polozov, A.G., Jerram, D.A., Shiganova, O.V., Melnikov, N.V., Iyer, K., Planke, S., 2018. Sills and gas generation in the Siberian Traps. Philos. Trans. Ser. A Math. Phys. Eng. Sci. 376 (2130).
Thorp, J.H., Rogers, D.C., Damborenea, C., 2019. Thorp and Covich's freshwater invertebrates. In: Volume 4, Keys to Palaearctic Fauna. Academic Press, Amsterdam.
Trayler, R.B., Schmitz, M.D., Cuitiño, J.I., Kohn, M.J., Bargo, M.S., Kay, R.F., Strömberg, C.A., Vizcaíno, S.F., 2020. An improved approach to age-modeling in deep time: Implications for the Santa Cruz Formation, Argentina. Bulletin of the Geological Society of America 132 (1–2), 233–244.
Vajda, V., McLoughlin, S., Mays, C., Frank, T.D., Fielding, C.R., Tevyaw, A., Lehsten, V., Bocking, M., Nicoll, R.S., 2020. End-Permian (252 Mya) deforestation, wildfires and flooding—an ancient biotic crisis with lessons for the present. Earth Planet. Sci. Lett. 529, 115875.
Vamosi, J.C., Vamosi, S.M., 2008. Extinction risk escalates in the tropics. PLoS One 3 (12), e3886.
van Hinsbergen, D.J.J., Abels, H.A., Bosch, W., Boekhout, F., Kitchka, A., Hamers, M., van der Meer, D.G., Geluk, M., Stephenson, R.A., 2015. Sedimentary geology of the middle Carboniferous of the Donbas region (Dniepr-Donets Basin, Ukraine). Sci. Rep. 5, 9099.
Vladimirovich, V.P., Lebedev, V.M., Popov, Y.N., Radchenko, G.P., Shvedov, N.A., 1967. Stratigraphy of Triassic of the Middle Siberia. In: Greiner, R.N. (Ed.), Mesozoic and Cenozoic Stratigraphy of Middle Siberia. Nauka, Novosibirsk, pp. 7–30 (In Russian).
Walliser, O.H., 1990. How to define "global bio-events". In: Kauffman, E.G., Walliser, O. H. (Eds.), Extinction Events in Earth History. Springer-Verlag, Berlin, pp. 1–4.
Wang, Y., Sadler, P., Shen, S., Crowley, J., Cao, C., Henderson, C., Wang, W., Shang, Q., Bowring, S.A., 2014. Quantifying the process and abruptness of the end-Permian mass extinction. Paleobiology 40 (1), 113–129.
Wardlaw, B.R., Davydov, V.I., 2005. Progress report of the Permian-Triassic Time Slice Project. Permophiles 45, 36–39.
Whitelock, L.M., 2002. The Cycads. Timber Press, Portland, Oregon, p. 374.
Whittaker, J.M., Afonso, J.C., Masterton, S., Müller, R.D., Wessel, P., Williams, S.E., Seton, M., 2015. Long-term interaction between mid-ocean ridges and mantle plumes. Nat. Geosci. 8 (6), 479–483.
Wiens, J.J., 2016. Climate-related local extinctions are already widespread among plant and animal species. PLoS Biol. 14 (12), e2001104.
Wignall, P.B., Chu, D., Hilton, J.M., Corso, J.D., Wu, Y., Wang, Y., Atkinson, J., Tong, J., 2020. Death in the shallows: the record of Permo-Triassic mass extinction in paralic settings, Southwest China. Glob. Planet. Chang. 189, 103176.
Wu, Y., Tong, J., Algeo, T.J., Chu, D., Cui, Y., Song, H., Shu, W., Du, Y., 2020. Organic carbon isotopes in terrestrial Permian-Triassic boundary sections of North China: Implications for global carbon cycle perturbations. Bull. Geol. Soc. Am. 132 (5–6), 1106–1118.
Xiong, C., Wang, Q., 2011. Permian–Triassic land-plant diversity in South China: was there a mass extinction at the Permian/Triassic boundary? Paleobiology 37 (1), 157–167.
Xu, G., Deconinck, J.-F., FENG, Q., Baudin, F., Pellenard, P., Shen, J., Bruneau, L., 2017. Clay mineralogical characteristics at the Permian–Triassic Shangsi section and their paleoenvironmental and/or paleoclimatic significance. Palaeogeogr. Palaeocimatol. Palaeogeogr. 474, 152–163.
Yan, E.V., Beutel, R.G., Lawrence, J.F., Yavorskaya, M.I., Hörnschemeyer, T., Pohl, H., Vassilenko, D.V., Bashkuev, A.S., Ponomarenko, A.G., 2019. Archaeomalthus-(Coleoptera, Archostemata) a 'ghost adult' of Micromalthidae from Upper Permian deposits of Siberia? Historical Biology 1–9.
Yasuhara, M., Wei, C.-L., Kucera, M., Costello, M.J., Tittensor, D.P., Kiessling, W., Bonebrake, T.C., Tabor, C.R., Feng, R., Baselga, A., Kretschmer, K., Kusumoto, B., Kubota, Y., 2020. Past and future decline of tropical pelagic biodiversity. Proc. Natl. Acad. Sci. U. S. A. 117 (23), 12891–12896.
Yin, H., Jiang, H., Xia, W., Feng, Q., Zhang, N., Shen, J., 2014. The end-Permian regression in South China and its implication on mass extinction. Earth - Science Reviews 137, 19–33.
Yin, H., Xie, S., Luo, G., Algeo, T.J., Zhang, K., 2012. Two episodes of environmental change at the Permian–Triassic boundary of the GSSP section Meishan. Earth - Science Reviews 115 (3), 163–172.
Yin, H., Zhang, K., Tong, J., Yang, Z., Wu, Shunbao, 2001. The Global Stratotype Section and Point (GSSP) of the Permian-Triassic Boundary. Episodes 24 (2), 102–114.
Yin, H., Feng, Q., Lai, X., Baud, A., Tong, J., Hongfu, Yin, Warrington, G., Xie, Shucheng, 2007. The protracted Permo-Triassic crisis and multi-episode extinction around the Permian-Triassic boundary. Glob. Planet. Chang. 55 (1–3), 1–20.
Yuan, A., Zhu, Z., Lin, W., Liu, Y., 2003. Susceptibility study on the terrestrial Permian-Triassic boundary in Ningwu, Shanxi Province, China. Di zhi ke ji qing bao = Geol. Sci. Technol. Inform. 22 (3), 37–40 (In Chinese).
Yuan, D.-X., Shen, S., Henderson, C.M., Chen, J., Zhang, H., Zheng, Q., Wu, H., 2019. Integrative timescale for the Lopingian (Late Permian): A review and update from Shangsi, South China. Earth Sci. Rev. 188, 190–209.
Zakharov, Y.D., Biakov, A.S., Horacek, M., Kutygin, R.V., Sobolev, E.S., Bond, D.P.G., 2020. Environmental control on biotic development in Siberia (Verkhoyansk Region) and neighbouring areas during Permian–Triassic large igneous province activity. In: Guex, J., Torday, J., Miller Jr., W.B. (Eds.), Morphogenesis, Environmental Stress and Reverse Evolution. Springer, Cham, pp. 197–231.
Zhang, H., Cao, C., Liu, X., Mu, L., Zheng, Q., Liu, F., Xiang, L., Liu, L., Shen, S., 2016. The terrestrial end-Permian mass extinction in South China. Palaeogeogr. Palaeocimatol. Palaeogeogr. 448, 108–124.
Zhang, F., Romaniello, S.J., Algeo, T.J., Lau, K.V., Clapham, M.E., Richoz, S., Herrmann, A.D., Smith, H., Horacek, M., Anbar, A.D., 2018. Multiple episodes of extensive marine anoxia linked to global warming and continental weathering following the latest Permian mass extinction. Sci. Adv. 4 (4), e1602921.
Zharinova, V.V., 2019. New discoveries of the conchostracans of late Permian and Early Triassic from Babyi Kamen section (Kuzbass). In: Paleostrat-2019. Program and Abstracts, pp. 28–29 (In Russian).
Zheng, X., Dai, S., Nechaev, V., Sun, R., 2020. Environmental perturbations during the latest Permian: evidence from organic carbon and mercury isotopes of a coal-bearing section in Yunnan Province, southwestern China. Chem. Geol. 549, 119680.
Zuchuat, V., Sleveland, A., Twitchett, R.J., Svensen, H.H., Turner, H., Augland, L.E., Jones, M.T., Hammer, Ø., Hauksson, B.T., Haflidason, H., Midtkandal, I., Planke, S., 2020. A new high-resolution stratigraphic and palaeoenvironmental record spanning the End-Permian Mass Extinction and its aftermath in Central Spitsbergen, Svalbard. Palaeogeogr. Palaeocimatol. Palaeogeogr. 109732 https://doi.org/10.1016/j.palaeo.2020.109732 in press.